

Master Thesis

# Experimental and numerical investigation of the mixing of laminar and turbulent streams

carried out for the purpose of obtaining the academic degree

**Diplom-Ingenieur (Dipl.-Ing.)**

submitted at TU Wien

Faculty of Mechanical and Industrial Engineering

by

**Paul Ecker**

Matr.Nr.: 01126617

under the supervision of

Ass.Prof. Dipl.-Ing. Dr.techn. Michael Harasek

and

Dipl.-Ing. Christian Jordan

and

Bahram Haddadi Sisakht, MSc

Institute of Chemical, Environmental and Bioscience Engineering

E166

## Abstract

The mixing of turbulent and laminar flow inside a rectangular channel T-junction is investigated using experimental and numerical methods. A non-intrusive, optical measurement technique (Laser Doppler Velocimetry) is applied to gather point-wise velocity information of the flow. This information is used to calculate the turbulent kinetic energy  $k$ , a measure of velocity fluctuations. Computational Fluid Dynamics (CFD), allows the detailed investigation of mixing flows based on finite volume method. However, because of the complexity of turbulent flow, economical simulations are restricted to the use of turbulence models to account for the velocity fluctuations. Comparison of measurements and simulation indicates that while velocities are predicted correctly, the simulation severely underpredicts the turbulent kinetic energy. Aim of this work is to use the obtained measurement data to calibrate the turbulence model, reducing the error in the prediction of  $k$ , and therefore enable a better simulation of the mixing fluid flow. This is achieved by modifying the default values of eight model constants present in the equations of the turbulence model. In order to reduce the computational effort a statistical method, Design of Experiments (DoE), is applied to identify the best possible value combinations. Using this method, a stationary point is predicted, reducing the error between measured and simulated turbulent kinetic energy in the turbulent flow from initially 90 % to 45 %.

**LDV**  
**CFD**  
**DoE**

## **Kurzfassung**

Das Mischverhalten von turbulenten und laminaren Strömungen in einem rechteckigen Kanal wird mittels experimenteller und numerischer Methoden untersucht. Eine kontaktlose, optische Messtechnik (Laser Doppler Velocimetry) wird angewandt um punktweise Geschwindigkeitsinformation der Strömung zu erfassen. Diese Information wird genutzt um die turbulente kinetische Energie  $k$ , ein Maß für die Geschwindigkeitsschwankungen, zu berechnen. Numerische Strömungssimulation (CFD) ermöglicht eine genaue Untersuchung der Strömung, basierend auf dem Finite-Volumen-Verfahren. Aufgrund der Komplexität von turbulenten Strömungen sind diese Simulationen auf Modelle angewiesen, die Geschwindigkeitsschwankungen erfassen. Der Vergleich von Messergebnissen und Simulation zeigt, dass Geschwindigkeiten korrekt vorhergesagt werden, die turbulente kinetische Energie allerdings stark unterschätzt wird. Ziel dieser Arbeit ist es, das Turbulenzmodell mithilfe der Messdaten zu kalibrieren und so den Fehler in der Vorhersage von  $k$  zu minimieren. Die Kalibration erfolgt durch Anpassung der Standardwerte der acht Modellkonstanten des Turbulenzmodells. Um den Rechenaufwand so gering wie möglich zu halten, wird eine statistische Methode, Design of Experiments (DoE), angewandt. Die so erhaltenen neuen Modellkonstanten reduzieren den Fehler zwischen experimenteller und numerischer turbulenter kinetischer Energie von initial 90 % auf 45 %.

## **Acknowledgment**

The computational results presented have been achieved in part using the Vienna Scientific Cluster (VSC). Financial support was provided by the Austrian research funding association (FFG) under the scope of the COMET program within the research project Industrial Methods for Process Analytical Chemistry From Measurement Technologies to Information Systems (imPACts, [www.k-pac.at](http://www.k-pac.at)) (contract # 843546). Special thanks to Bahram and Christian for supporting this thesis.

## **Affidavit**

I confirm, that going to pres of this thesis needs the conformation of the examination committee. I declare in lieu of oath, that I wrote this thesis and performed the associated research myself, using only literature cited in this volume. If text passages from sources are used literally, they are marked as such. I confirm that this work is original and has not been submitted elsewhere for any examination, nor is it currently under consideration for a thesis elsewhere.

Vienna, February 1, 2018

# Contents

<b>1</b>	<b>Introduction</b>	<b>14</b>
1.1	Aim of this work . . . . .	14
1.2	Structure . . . . .	15
1.3	Applied Software . . . . .	16
<b>2</b>	<b>Theoretical Background</b>	<b>18</b>
2.1	Turbulent Flow . . . . .	18
2.2	Governing Equations . . . . .	19
2.2.1	Direct Numerical Simulation (DNS) . . . . .	20
2.3	Reynolds Averaged Navier Stokes Equations . . . . .	21
2.3.1	Closure Problem . . . . .	22
2.3.2	Linear Eddy Viscosity Models . . . . .	22
2.3.3	Closure Coefficients . . . . .	22
2.4	The $k - \omega - SST$ Model . . . . .	23
2.4.1	Model formulation . . . . .	24
2.4.2	Closure Coefficients . . . . .	25
2.5	The $\gamma - Re_\theta$ Model . . . . .	26
2.5.1	Transition modeling concept . . . . .	27
2.5.2	Transition Model Formulation . . . . .	28
2.5.3	Closure Coefficients . . . . .	30
2.5.4	Coupling with the $k - \omega - SST$ Model . . . . .	31
2.6	Laser Doppler Velocimetry (LDV) . . . . .	31
2.6.1	Measurement principle . . . . .	31
2.6.2	Seeding . . . . .	32
2.6.3	LDV Components . . . . .	33
2.6.4	Evaluation of measurement data . . . . .	34
2.7	Design of Experiments (DoE) . . . . .	35

2.7.1	Introduction to DoE . . . . .	35
2.7.2	Fractional Factorial Design . . . . .	38
2.7.3	Objectives of DoE . . . . .	40
2.7.4	Evaluation of Raw Data . . . . .	41
2.7.5	Model Quality . . . . .	41
<b>3</b>	<b>Experimental Investigation</b>	<b>46</b>
3.1	Investigated Flow . . . . .	46
3.2	LDV- Measurement Positions . . . . .	47
3.3	Experimental Setup . . . . .	48
3.3.1	Estimation of Pump Error . . . . .	49
3.3.2	Selection of Seeding Particles . . . . .	51
3.4	Measurement Results . . . . .	52
<b>4</b>	<b>Numerical investigation</b>	<b>54</b>
4.1	Mesh selection . . . . .	54
4.2	Base case - Setup . . . . .	56
4.2.1	Boundary Conditions . . . . .	56
4.2.2	Solver settings . . . . .	57
4.3	Base Case - Results . . . . .	58
<b>5</b>	<b>Screening Simulations</b>	<b>63</b>
5.1	Simplified Mesh . . . . .	63
5.2	Boundary Conditions . . . . .	63
5.3	Design of Simulation Experiments . . . . .	64
5.3.1	Response . . . . .	65
5.4	Evaluation . . . . .	66
<b>6</b>	<b>Optimization Simulations</b>	<b>68</b>
6.1	Boundary Conditions . . . . .	68

6.2	Design . . . . .	68
6.3	Response . . . . .	69
6.4	1 <sup>st</sup> Optimization . . . . .	70
6.4.1	Setup . . . . .	70
6.4.2	Evaluation . . . . .	71
6.5	2 <sup>nd</sup> Optimization . . . . .	73
6.5.1	Evaluation . . . . .	74
<b>7</b>	<b>Optimization Results</b>	<b>77</b>
7.1	Qualitative Comparison . . . . .	77
7.2	Global Error Comparison . . . . .	79
7.2.1	Turbulent Kinetic Energy, all Profiles . . . . .	79
7.2.2	Turbulent Kinetic Energy, only turbulent sections . . . . .	80
7.2.3	Velocity . . . . .	81
7.3	Profile Error Comparison . . . . .	83
7.3.1	Turbulent kinetic energy . . . . .	83
7.3.2	Velocity . . . . .	85
<b>8</b>	<b>Summary and Outlook</b>	<b>87</b>
8.1	Summary . . . . .	87
8.2	Future Work . . . . .	88
	<b>Appendices</b>	<b>90</b>
	<b>Appendix A Empirical Correlations</b>	<b>90</b>
	<b>Appendix B Measurement Results - Cross section</b>	<b>91</b>
	<b>Appendix C Measurement Results - Box plot</b>	<b>92</b>
	<b>Appendix D OpenFOAM solver settings</b>	<b>93</b>
D.1	turbulenceProperties . . . . .	93

D.2	fvSolution . . . . .	94
D.3	fvSchemes . . . . .	96
<b>Appendix E Profile 1</b>		<b>98</b>
<b>Appendix F Profile 2</b>		<b>99</b>
<b>Appendix G Profile 3</b>		<b>101</b>
<b>Appendix H Profile 4</b>		<b>102</b>
<b>Appendix I Profile 5</b>		<b>104</b>

## List of Figures

1	Laminar and turbulent flow in a pipe (Oertel 2012) . . . . .	18
2	Axial component of velocity on the centerline of a turbulent jet. (C. Tong and Warhaft 1995) . . . . .	19
3	Principle of the $k - \omega - SST$ model . . . . .	23
4	Principle of the $\gamma - Re_\theta$ model . . . . .	26
5	Measurement principle of LDV (Haddadi et al. 2018) . . . . .	32
6	Components of the LDV system and experimental setup (Haddadi et al. 2018)	34
7	LDV velocity distribution. Result of one measurement point (Haddadi et al. 2018) . . . . .	35
8	Fitting a simple model to experimental data containing Factors $x_n$ , Responses $y_m$ , Coefficients $\beta_i$ and the model error $e_m$ . . . . .	36
9	Geometrical representation and design of a three factor full factorial design (without center points) . . . . .	37
10	Graphical interpretation of a $2^{3-1}$ ( $g = 3, b = 1$ ) fractional factorial design.	38
11	Different fractional factorial designs and their resolution (roman numerals). Leftmost column indicates the required number of runs. . . . .	39

12	Outline of the DoE workflow applied in this work . . . . .	40
13	Boxplot of normally distributed (A) and tailed data (B) . . . . .	41
14	Interpretation of the Half-normal plot . . . . .	45
15	Channel dimensions in mm . . . . .	46
16	Position of the five measurement profiles . . . . .	47
17	Experimental Setup: 1 = Laser source and Bragg cell, 2 = LDV probe, 3 = Traverse System, 4 = Flow channel, 5 = Pumps and water tank . . . . .	49
18	Velocity profiles for the pump error estimation . . . . .	50
19	Comparison of aluminium and hollow glass particles for seeding . . . . .	52
20	FLTR: Case 0.0, Case 0.1, Case 0.2 (Intermittency: blue = 0, red = 1) . .	55
21	Inlet section and stratifiers of the mesh used for the simulation . . . . .	56
22	Convergence of the Base Case (Slice 1 = Laminar section, Slice 2 = Turbu- lent section, Slice 3 = Mixing section) . . . . .	58
23	Simulation results of the mixing section . . . . .	59
24	Velocity measurement and base case simulation comparison (Profile 3) . . .	60
25	Velocity measurement and base case simulation comparison (Profile 2 and Profile 5) . . . . .	61
26	Turbulent kinetic energy measurement and base case simulation comparison (Profile 2 and Profile 3) . . . . .	61
27	Turbulent kinetic energy and velocity measurement. Base case simulation comparison (Profile 4 at $z/h = 0.6$ ) . . . . .	62
28	Segment of the simplified mesh for the Screening simulations . . . . .	63
29	Boxplot of the transformed Response . . . . .	66
30	Screening results - Main effects plot . . . . .	66
31	Screening results - Half normal plot . . . . .	67
32	RSM Design . . . . .	69
33	3D contour plot of the first optimization design, Error on the z-Axis denoted as SSE . . . . .	72
34	Movement of the center points . . . . .	73

35	Boxplot of the 2 <sup>nd</sup> optimization response . . . . .	75
36	Residual plot of the 2 <sup>nd</sup> quadratic model . . . . .	75
37	3D contour plot of the second optimization design . . . . .	76
38	Qualitative comparison of the simulation with standard and adjusted coefficients at the symmetry plane . . . . .	78
39	Intermittency values at $z/h = 0.5$ . . . . .	78
40	Error comparison of the turbulent kinetic energy error for all optimization simulations . . . . .	79
41	Error composition of the turbulent kinetic energy error with the standard (left) and adjusted (right) coefficients . . . . .	80
42	Error comparison of the turbulent kinetic energy error for all optimization simulations, without the laminar profile . . . . .	81
43	Error composition of the turbulent kinetic energy error with the standard (left) and adjusted (right) coefficients, without the laminar profile . . . . .	81
44	Error comparison of the velocity error for all optimization simulations. . . . .	82
45	Error composition of the velocity error with the standard (left) and adjusted (right) coefficients . . . . .	82
46	Effect of the parameter change on the turbulent kinetic energy, profiles 1 and 5 at $z/h = 0.6$ . . . . .	83
47	Simulation profile 5 with different scaling at $z/h = 0.6$ . . . . .	84
48	Effect of the parameter change on the turbulent kinetic energy, profile 2 at $z/h = 0.5$ . . . . .	84
49	Effect of the parameter change on the turbulent kinetic energy, profile 3 at $z/h = 0.6$ . . . . .	85
50	Effect of the parameter change on the velocity components, profiles 2 at $z/h = 0.5$ . . . . .	86
51	Valid counts for all measurement points . . . . .	91
52	Valid counts for all measurement points . . . . .	92
53	Turbulent kinetic energy comparison (Profile 1) . . . . .	98

54	Standard coefficients velocity components comparison (Profile 1) . . . . .	98
55	Adjusted coefficients velocity components comparison (Profile 1) . . . . .	99
56	Turbulent kinetic energy comparison (Profile 2) . . . . .	99
57	Standard coefficients velocity components comparison (Profile 2) . . . . .	100
58	Adjusted coefficients velocity components comparison (Profile 2) . . . . .	100
59	Turbulent kinetic energy comparison (Profile 3) . . . . .	101
60	Standard coefficients velocity components comparison (Profile 3) . . . . .	101
61	Adjusted coefficients velocity components comparison (Profile 3) . . . . .	102
62	Turbulent kinetic energy comparison (Profile 4) . . . . .	102
63	Standard coefficients velocity components comparison (Profile 4) . . . . .	103
64	Adjusted coefficients velocity components comparison (Profile 4) . . . . .	103
65	Turbulent kinetic energy comparison (Profile 5) . . . . .	104
66	Standard coefficients velocity components comparison (Profile 5) . . . . .	104
67	Adjusted coefficients velocity components comparison (Profile 5) . . . . .	105

## List of Tables

1	R Packages used in this work . . . . .	17
2	Stokes number based on particle size distribution for SPHERICEL <sup>®</sup> 110P8	33
3	Confounding of factors in a $2^{4-1}$ fractional factorial design . . . . .	39
4	Example output of R for an interaction model . . . . .	42
5	Example output of an interaction model fitted to a fractional factorial design	44
6	Calculated flowrates for the different channel sections . . . . .	47
7	Water properties for 20 °C . . . . .	47
8	Measurement profiles and resolution . . . . .	48
9	Summary of the pump error investigation . . . . .	51
10	Experimental conditions . . . . .	53
11	Properties of the meshes used in the mesh dependence study . . . . .	55
12	Boundary conditions for the Base Case . . . . .	57

---

13	CFD boundary conditions for Screening . . . . .	64
14	Investigated values of the Screening exercise . . . . .	64
15	Fractional factorial screening design . . . . .	65
16	Confounding pattern of two factor interactions . . . . .	67
17	Investigated values of the first Optimization Design . . . . .	70
18	First optimization design . . . . .	71
19	Investigated values of the first optimization design . . . . .	73
20	2 <sup>nd</sup> Optimization Design . . . . .	74
21	Optimization results . . . . .	76

---

# Nomenclature

## Greek letters

$\eta$	Kolmogorov length scale
$\lambda$	Laser wavelength
$\mu$	Dynamic viscosity
$\mu_t$	Eddy viscosity
$\nu$	Kinematic viscosity
$\Omega$	Vorticity magnitude
$\omega$	Specific turbulence dissipation rate
$\rho$	Fluid density
$\rho_p$	Seeding particle density
$\tau_\eta$	Kolmogorov time scale
$\theta$	Momentum thickness
$\varepsilon$	Dissipation rate
$\beta$	Regression coefficient
$\gamma$	Intermittency
$\hat{\sigma}^2$	Residual variance

## Latin letters

$\tilde{Re}_{\theta t}$	Local transition onset momentum thickness Reynolds number
$Co$	Courant number
$d$	Fringe distance
$D/Dt$	Material derivative
$d_h$	Hydraulic diameter
$e$	Regression model error
$f_d$	Doppler frequency
$g$	Number of factors

---

$k$	Turbulent kinetic energy
$L$	Characteristic length scale
$n$	Number of valid counts
$p$	Pressure
$R$	Seeding particle radius
$R^2$	Coefficient of determination
$Re_{\theta c}$	Critical momentum thickness Reynolds number
$Re_{\theta t}$	Transition onset momentum thickness Reynolds number
$Re_v$	Vorticity Reynolds number
$S_{ij}$	Rate of strain
$St$	Stokes number
$T$	Temperature
$Tu$	Turbulence intensity
$U$	Freestream velocity
$U(x, t)$	Velocity field
$u(x, t)$	Fluctuating velocity component
$U_0$	Local freestream velocity
$u_\eta$	Kolmogorov velocity scale
$u_\tau$	Friction velocity
$V$	Total volume
$v_i$	Volume of cell i
$x$	Regression model factor
$y$	Regression model response
$y^+$	Dimensional wall distance

# 1 Introduction

## 1.1 Aim of this work

Computational Fluid Dynamics (CFD) can provide a detailed investigation of industrial size mixing processes, that are either economically or physically not accessible for ordinary measurement devices. In principle, the governing fluid flow equations for mass, impulse and energy can be solved numerically which is referred to as Direct Numerical Simulation (DNS). However, due to the complexity of turbulence DNS requires high spatial and temporal resolution, resulting in unfeasible computational requirements for industrial size applications. In order to circumvent this challenge Osborne Reynolds proposed a simplification by splitting the flow field in a mean and fluctuating component. The resulting Reynolds Averaged Navier Stokes (RANS) Equations use turbulence models (e.g.  $k - \omega - SST$ ) to account for the turbulent kinetic energy  $k$ , a measure of velocity fluctuations.

A downside of RANS - based models is their inability to capture the effect of laminar-turbulent transition. Empirical correlation models e.g. Abu-Ghannam and Shaw (1980) successfully predict transition in special purpose cases, however due to their non-local formulation are not applicable for unstructured, general purpose CFD codes. In 2006 the  $\gamma - Re_\theta$  model, a correlation based transition model that adds two additional transport equations and three empirical correlations to the  $k - \omega - SST$  turbulence model, was introduced (Robin Blair Langtry 2006). Part of this work is to confirm the correct implementation of the  $\gamma - Re_\theta$  model in OpenFOAM<sup>®</sup> and verify its ability to represent laminar and turbulent internal flows.

In order to prove the models validity, mixing experiments in a T-junction rectangular glass channel are conducted. Velocities and turbulent kinetic energy predicted in the simulation are compared to experimental data. Laser Doppler Velocimetry (LDV) is used to gather point-wise velocity information of the flow.

The initial comparison of simulation and experiment reveals that while velocities are predicted accurately, turbulent kinetic energy values are under-predicted in every point of the flow field. This observation is consistent with Zöchbauer, Smith, and Lauer (2015) who investigated LDV- measurements, LES and RANS simulations in an exhaust gas pipe. A possible reason for this discrepancy are the models standard values for its *Closure Coefficients*.

Closure coefficients are constants present in the transport equations of the turbulence model. The determination of these values is achieved by a combination of experimental observations and experience (Wilcox 1988). It is known that small changes in these values can significantly improve or deteriorate the simulation results (Schaefer et al. 2017). Since most turbulence models are primarily calibrated for external flow, it is conceivable that changing the standard values of the closure coefficients can lead to a reduction of error.

The main ambition of this work is therefore to find a combination of closure coefficient values that reduces the error in turbulent kinetic energy prediction to a minimum, while maintaining the accurate prediction of velocity components. Since the selected turbulence model contains 8 closure coefficients influencing the prediction of  $k$ , an organized approach is preferable to reduce the necessary number of simulations for this task. Design of Experiments (DoE) offers such an approach by fitting a regression model to the outcome of a structured experimental plan.

### 1.2 Structure

The first part of this work is an introduction to Computational Fluid Dynamics (CFD), especially turbulence modelling and why it is necessary, as well as the advantages and disadvantages of RANS-based turbulence models. A summary of the  $\gamma - Re_\theta$  transition model used in this work is given. Subsequently, the measurement principle of Laser Doppler

Velocimetry (LDV) is described, including the selection of suitable seeding particles. An overview of Design of Experiments (DoE) is presented, clarifying the aim, advantages and execution of this method.

Section 3 introduces the investigated flow, measurement setup and experimental conditions. The numerical investigation of this work is split in three parts. First, the *Base Case* is established and initially compared with measurement results. Then, as part of the DoE, the *Screening* simulations are presented and evaluated. Based on the Screening results the final *Optimization* step leads to the desired minimum of error (= stationary point). Concluding, the results of LDV-measurements and stationary point simulation are compared and evaluated.

### 1.3 Applied Software

The results presented in this work are achieved using different free to use software:

The open source CFD-code *OpenFOAM*®4.1 is employed to obtain the numerical solution of the flow.

*ParaView 5.0.1*, a data analysis and visualization software, is used for the post-processing of the simulation results.

Evaluation of simulation and measurement data, as well as conducting Design of Experiments, is carried out with the statistical computing environment "R" 3.3.2. A major advantage of this software is its availability of user created content, so called "Packages". The Packages utilized in this work are listed in Table 1.

The computational results presented in this work have been achieved in part using the Vienna Scientific Cluster (VSC).

## 1. INTRODUCTION

---

Table 1: R Packages used in this work

<b>Package</b>	<b>Version</b>	<b>Source</b>	<b>Description</b>
FrF2	1.7-2	Groemping 2014	Fractional Factorial Design
rsm	2.8	Lenth 2009	Response-surface Analysis
daewr	1.1-7	Lawson 2016	Design and Analysis of Experiments with R
ggplot2	2.2.1	Wickham 2009	Data visualization

## 2 Theoretical Background

### 2.1 Turbulent Flow

The following description of turbulent flows and turbulence modeling is based on the work of Pope (2000). A visual representation of the difference between laminar and turbulent flow is depicted in Figure 1. Dye is inserted in a pipe, if laminar flow is present the dye stream is undistorted by the flow and continues on a parallel path along the pipes axis. However if the flow is turbulent the dye is jiggled by turbulent motion resulting in a mixing of water and dye. This experiment was conducted by *Reynolds* in 1883 and lays the groundwork for our understanding of turbulent flow. Reynolds later established a dimensionless parameter, now known as the Reynolds number  $Re$ , to distinguish between the two flow regimes. It consists of the the characteristic velocity  $U$  ( $m/s$ ) and length  $L$  ( $m$ ) as well as the kinematic viscosity  $\nu$  ( $m^2/s$ ).

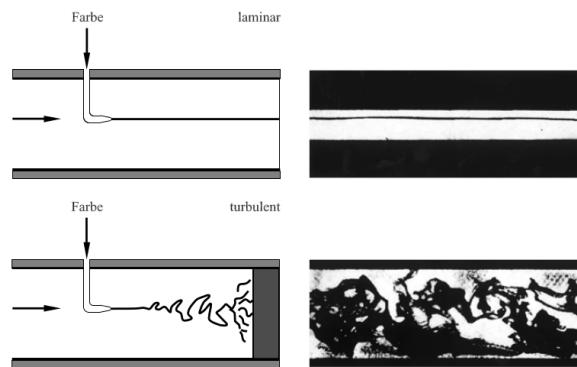


Figure 1: Laminar and turbulent flow in a pipe (Oertel 2012)

$$Re = \frac{UL}{\nu} \quad (2.1)$$

The defining property of a turbulent flow is its significant, irregular variation of the velocity field, denoted  $U(x, t)$ , in both time and space as displayed in Figure 2. These velocity fluctuations lead to a much better transport and mixing characteristic compared to laminar

## 2. THEORETICAL BACKGROUND

---

flows, as well as higher pressure drop, shear stress and heat transfer. In many engineering applications turbulent flow is prevalent, a correct prediction of the turbulence magnitude and the distinction between laminar and turbulent flow by numerical simulations is therefore highly desirable. However, as the following sections will discuss, the characteristic velocity fluctuations of a turbulent flow pose a challenge for efficient numerical simulation.

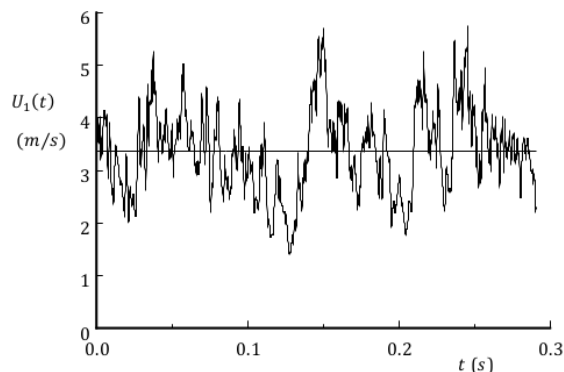


Figure 2: Axial component of velocity on the centerline of a turbulent jet. (C. Tong and Warhaft 1995)

### 2.2 Governing Equations

The basic equations governing the flow of an incompressible fluid are the continuity equation for conservation of mass (Equation 2.2), the Navier-Stokes equations (incompressible, newtonian fluids) for conservation of momentum (Equation 2.3) and the energy equation for conservation of energy (Equation 2.4). They make up a system of 5 equations and 5 unknowns: Three velocity components ( $u, v, w$ ), pressure  $p$  and enthalpy  $h$ .

$$\frac{\partial \rho}{\partial t} + \nabla(\rho U) = 0 \quad (2.2)$$

$$\frac{DU}{Dt} = -\frac{1}{\rho} \nabla p + \nu \nabla^2 U \quad (2.3)$$

$$\rho \frac{D}{Dt} \left[ h + \frac{1}{2} u_i u_i \right] = \frac{\partial p}{\partial t} + \frac{\partial}{\partial x_i} [u_i S_{ij}] - \frac{\partial q_i}{\partial x_i} + \rho g_i u_i \quad (2.4)$$

### 2.2.1 Direct Numerical Simulation (DNS)

For a given flow this complete set of equations can be solved numerically, given appropriate initial and boundary conditions, to obtain the fluid properties at every grid point. This is referred to as *Direct Numerical Simulation (DNS)*. In turbulent flows the grid size must therefore be in magnitude of the smallest turbulent motions, the so called *Kolmogorov Scales*.

#### Energy cascade & Kolmogorov Scales

*"Big whorls have little whorls,  
Which feed on their velocity  
And little whorls have lesser whorls,  
And so on to viscosity (in the molecular sense)."*

In 1922 *Richardson* summarized the concept of the *Energy Cascade* with the above poem (Pope 2000). The concept is based on the consideration that turbulence is composed of eddies of different sizes. Eddies of size  $\ell$  have a characteristic velocity  $u(\ell)$  and timescale  $\tau(\ell) \equiv \ell/u(\ell)$ . Richardsons assumption is that large eddies are unstable and break up into smaller eddies, transferring their energy. This process continues until the Reynolds number  $Re(\ell) = u(\ell)\ell/\mu$  is sufficiently small that the eddy motion is stable, and molecular viscosity dissipates the kinetic energy. In 1941 *Kolmogorov* enhanced the concept of the energy cascade by combining the rate of dissipation  $\varepsilon = u_0^3/\ell_0$  and kinematic viscosity  $\nu$  to define the "*Kolmogorov Scales*". They represent characteristic length (Equation 2.5), velocity (Equation 2.6) and time (Equation 2.7) scales of the smallest turbulent motion.

$$\eta \equiv \left( \frac{\nu^3}{\varepsilon} \right)^{1/4} \quad (2.5)$$

$$u_\eta \equiv (\varepsilon\nu)^{1/4} \quad (2.6)$$

$$\tau_\eta \equiv \left(\frac{\nu}{\varepsilon}\right)^{1/2} \quad (2.7)$$

Based on the Kolmogorov Scales an estimation for the necessary number of grid nodes  $N$  as a function of the Reynolds number, can be made.

$$N^4 \sim Re^3 \quad (2.8)$$

### 2.3 Reynolds Averaged Navier Stokes Equations

Because of the above requirement, DNS is not economically applicable for industrial size, turbulent flows. Simplifications are therefore made in order to simulate high Reynolds number flows. In 1894 *Reynolds* proposed a decomposition of the velocity  $U(x, t)$  in a mean component  $\langle U(x, t) \rangle$  and a fluctuating component  $u(x, t)$ .

$$U(x, t) = \langle U(x, t) \rangle + u(x, t) \quad (2.9)$$

also referred to as *Reynolds decomposition*. By applying the Reynolds decomposition on the Navier- Stokes equation (Equation 2.3) the Reynolds Averaged Navier Stokes (RANS) equation is obtained.

$$\frac{D\langle \bar{U}_j \rangle}{Dt} = \nu \nabla^2 \langle U_j \rangle - \frac{\partial \langle u_i u_j \rangle}{\partial x_i} - \frac{1}{\rho} \frac{\partial \langle p \rangle}{\partial x_j} \quad (2.10)$$

Comparing Equation 2.10 with Equation 2.3, an additional term  $\langle u_i u_j \rangle$  is present in the RANS equation, referred to as *Reynolds stresses*. Because of its symmetry ( $\langle u_i u_j \rangle = \langle u_j u_i \rangle$ ), it introduces six new variables to the system of equations. Based on the Reynolds stress tensor an important variable, the "*turbulent kinetic energy*", can be defined as half the trace of the tensor.

$$k = \frac{1}{2} \langle u_i u_i \rangle \quad (2.11)$$

### 2.3.1 Closure Problem

For a three-dimensional flow, there are four independent equations governing the flow. However, due to the Reynolds stresses, there are ten unknown variables (Three velocity components, pressure and six Reynolds stresses), which is referred to as the *closure problem*. Solving this problem, i.e. modeling the Reynolds stresses, ultimately leads to the variety of different turbulence models available today. One approach is based on an analogy between the Reynolds stresses and molecular viscosity, so called "*Linear Eddy Viscosity Models*".

### 2.3.2 Linear Eddy Viscosity Models

The idea of eddy viscosity, also known as turbulent viscosity was first introduced in 1877 by J. V. Boussinesq. He proposed modeling the Reynolds stresses analogous to the Newtonian friction law, replacing the molecular viscosity and non-linear terms with a single variable called the eddy viscosity  $\nu_t$ . The eddy viscosity is not a fluid property, but a property of the flow turbulence and can be interpreted as the magnitude of mixing due to turbulence and its effect on the mean flow.

$$\langle u_i u_j \rangle = 2\nu_t S_{ij} - \frac{2}{3}k\delta_{ij} \quad (2.12)$$

Popular turbulence models such as the " $k - \omega$ " model are based on this concept. They solve two additional transport equations for the turbulent kinetic energy ( $k$ ) and specific dissipation rate ( $\omega$ ), to calculate  $\nu_t = f(k, \omega)$ .

### 2.3.3 Closure Coefficients

An example transport equation for  $k$ , originating from the  $k - \omega$  model, is represented in Equation 2.13 (Wilcox 1988).

$$\frac{\partial}{\partial t}(\rho k) + \frac{\partial}{\partial x_j}(\rho U_j k) = \tilde{P}_k - \beta^* \rho \omega k + \frac{\partial}{\partial x_j} \left[ (\mu + \sigma^* \mu_t) \frac{\partial k}{\partial x_j} \right] \quad (2.13)$$

## 2. THEORETICAL BACKGROUND

---

It contains the variables  $\beta^*$  and  $\sigma^*$ , examples of so called "closure coefficients". Closure coefficients are present in all turbulent eddy viscosity models due to dimensional reasons. Their constant numerical value is determined by the models authors, based on a combination of dimensional analysis and experimental measurements (Schaefer et al. 2017). For example, the value of  $\beta^*$  was obtained by examination of the log layer region. Various simplifications lead to the relation  $\sqrt{\beta^*} = \tau/k$ . Based on experiments it was concluded that  $\tau/k = 0.3$  in the log layer region which resulted in a standard value for  $\beta^* = 0.09$ . The value for  $\sigma^* = 0.5$  on the other hand is solely chosen because it yields the best fit for a set of experimental results (Wilcox 1988). Because of this calibration to experimental data, it is unlikely that a turbulence model with a given set of closure coefficients is equally valid for any type of flow. Efforts are therefore made to calibrate (i.e. change the values of the closure coefficients) turbulence models for specific flow problems. (Stephanopoulos et al. 2016) performed an uncertainty quantification on a 2D flat-plate and backward-facing step, using different turbulence models. They found that the  $k - \omega - SST$  model is most sensitive to the  $\sigma_{\omega_1}$  coefficient. A similar investigation was performed by Schaefer et al. (2017) for transonic flows, who determined that  $\beta^*$  is the most influential parameter in the  $k - \omega - SST$  model.

### 2.4 The $k - \omega - SST$ Model

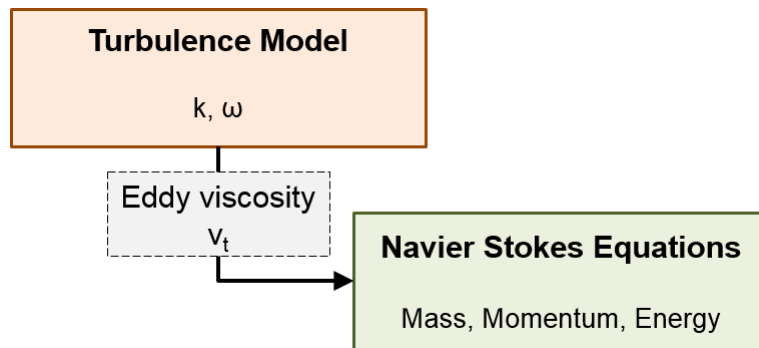


Figure 3: Principle of the  $k - \omega - SST$  model

## 2. THEORETICAL BACKGROUND

---

The  $k - \omega - SST$  turbulence model is a RANS based, two-equation eddy viscosity model (F. R. Menter 1994). By itself it is a combination of the  $k - \varepsilon$  (Launder and Sharma 1974), and the  $k - \omega$  turbulence model (Wilcox 1988). The motivation for this combination is the superior behavior of the  $k - \varepsilon$  model in the free-stream, and  $k - \omega$  model near wall regions. Using a blending function, the  $k - \omega - SST$  model switches between both in order to yield the best possible solution (F. R. Menter 1994), (Pope 2000). OpenFOAM<sup>®</sup> 4.0 implements the  $k - \omega - SST$  model as specified in F. Menter and Esch (2001) with two notable exceptions. The closure coefficient values are inherited from F. R. Menter, Kuntz, and R. Langtry (2003), and an additional blending function  $F_3$  is used as described in Hellsten (1998).

### 2.4.1 Model formulation

The core of the model are its two transport equations for the turbulent kinetic energy  $k$  (Equation 2.14),

$$\frac{\partial}{\partial t}(\rho k) + \frac{\partial}{\partial x_j}(\rho U_j k) = \tilde{P}_k - \beta^* \rho \omega k + \frac{\partial}{\partial x_j} \left[ \left( \mu + \frac{\mu_t}{\sigma_k} \right) \frac{\partial k}{\partial x_j} \right] \quad (2.14)$$

and the specific dissipation rate  $\omega$  (Equation 2.15).

$$\frac{\partial}{\partial t}(\rho \omega) + \frac{\partial}{\partial x_j}(\rho U_j \omega) = \frac{\gamma}{\nu_t} P_k - \beta \rho \omega^2 + \frac{\partial}{\partial x_j} \left[ \left( \mu + \frac{\mu_t}{\sigma_\omega} \right) \frac{\partial \omega}{\partial x_j} \right] + (1 - F_1) 2 \rho \sigma_{\omega 2} \frac{1}{\omega} \frac{\partial k}{\partial x_j} \frac{\partial}{\partial x_j} \quad (2.15)$$

Where  $F_1$  is the blending function responsible for the switch between the  $k - \omega$  ( $F_1 = 1$ ) and  $k - \varepsilon$  ( $F_1 = 0$ ) formulation.

$$F_1 = \tanh(\arg_1^4); \quad \arg_1 = \min \left( \max \left( \frac{\sqrt{k}}{\beta^* \omega y} \right); \frac{4 \rho \sigma_{\omega 2} k}{C D_{k\omega} y^2} \right) \quad (2.16)$$

The production of turbulent kinetic energy (Equation 2.14) is described by

$$\tilde{P}_k = \min(P_k; 10 * \beta^* \rho k \omega) \quad (2.17)$$

$$P_k = \tau_{ij} \frac{\partial U_i}{\partial x_j} \quad (2.18)$$

The calculation of the turbulent eddy viscosity  $\nu_t$  is defined as

$$\nu_t = \frac{a_1 k}{\max(a_1 \omega; S F_2)} \quad (2.19)$$

with  $S$  representing the invariant measure of the strain rate, and  $F_2$  being an additional blending function.

$$F_2 = \tanh(\arg_2^2); \quad \arg_2 = \max\left(2 \frac{\sqrt{k}}{\beta^* \omega y}; \frac{500\nu}{y^2 \omega}\right) \quad (2.20)$$

#### 2.4.2 Closure Coefficients

The coefficients  $\varphi$  of the SST model are computed as a blend of the corresponding  $k - \omega$  ( $\varphi_1$ ), and  $k - \epsilon$  closure coefficients ( $\varphi_2$ ). A short description is given based on Wilcox (1988) and Schaefer et al. (2017).

$$\varphi = \varphi_1 F_1 + (1 - F_1) \varphi_2 \quad (2.21)$$

- $\sigma_{k1} = 0.85$ ,  $\sigma_{k2} = 1.0$ : Values chosen to match empirical decay rate of  $k$  and  $\nu_t$  (Equation 2.14).
- $\sigma_{\omega1} = 0.5$ ,  $\sigma_{\omega2} = 0.856$ : Values chosen to match empirical decay rate of  $k$  and  $\nu_t$  (Equation 2.15, Equation 2.16)
- $\beta_1 = 0.075$ ,  $\beta_2 = 0.0828$ : Approximates the time decay of homogeneous isotropic turbulence experiments (Equation 2.15)
- $\beta^* = 0.09$ : Relates  $\tau/k = 0.3$  in the log layer; (Equation 2.14, Equation 2.16 and Equation 2.20)
- $\gamma_1 = \beta_1 / \beta^* - \sigma_{\omega1} * \kappa^2 / \sqrt{\beta^*} = 5/9$  (Equation 2.15)

## 2. THEORETICAL BACKGROUND

---

- $\gamma_2 = \beta_2/\beta * -\sigma_{\omega_2} * \kappa^2/\sqrt{\beta^*} = 0.44$  (Equation 2.15)
- $a_1 = 0.31$ : Present in the turbulent eddy viscosity definition. According to Schaefer et al. (2017) decreasing it would lead to non-physical results. (Equation 2.19)

### 2.5 The $\gamma - Re_\theta$ Model

The turbulence model investigated in this work is the  $\gamma - Re_\theta$  Model which was published in its entirety in 2009 (Robin B. Langtry and Florian R. Menter 2009). It extends the  $k-\omega-SST$  model (F. Menter and Esch 2001) by adding two additional transport equations for the intermittency  $\gamma$ , and the local transition onset momentum thickness Reynolds number  $\tilde{Re}_{\theta t}$ , as well as three empirical correlations, in order to model laminar-turbulent transition. The functional principle of the model is depicted in Figure 4, dividing the equations necessary to describe the fluid flow in three categories.

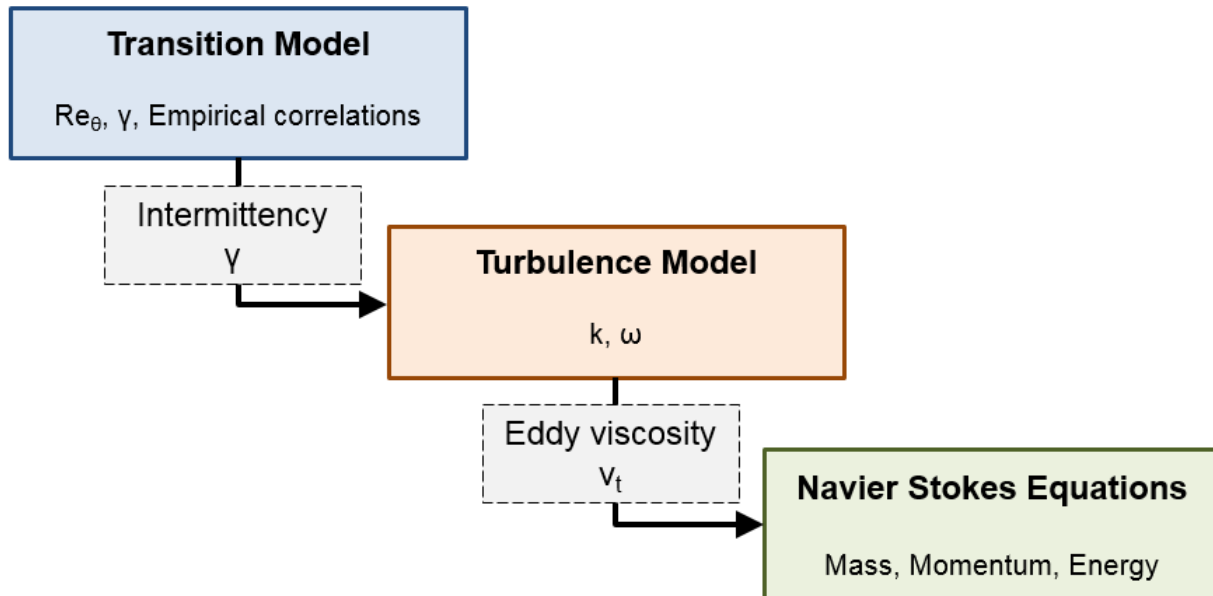


Figure 4: Principle of the  $\gamma - Re_\theta$  model

First, the empirical correlations and transport equations of the transition model are solved to determine the value of  $\gamma$ , a measure for transition onset. Second, the turbulence

model transport equations calculate the eddy viscosity  $\nu_t$ , which is subsequently used to acquire the solution of the flow fields governing equations.

### 2.5.1 Transition modeling concept

In order to better understand the working of the  $\gamma - Re_\theta$  model, it is advantageous to review former approaches of transition modeling.

Empirical correlation models e.g. Abu-Ghannam and Shaw (1980) connect the momentum thickness Reynolds number  $Re_\theta$

$$\theta = \int \frac{u}{U_0} * (1 - \frac{u}{U_0}) * dy \quad (2.22)$$

$$Re_\theta = \frac{\rho\theta U_0}{\mu} \quad (2.23)$$

with local free-stream conditions (e.g. Turbulent intensity, Pressure gradient). This is achieved by calculating the laminar solution and integrating the boundary layer quantities in order to calculate  $Re_\theta$ . If the calculated  $Re_\theta$  exceeds the one obtained from the empirical calculation, transition onset is assumed. The main shortcoming of these models is their non-local formulation, which makes them unfit for 3D, unstructured CFD codes (Robin B. Langtry and Florian R. Menter 2009). Menter proposed a link between the vorticity Reynolds number  $Re_v$  (Blumer and VanDriest 1963)

$$Re_v = \frac{\rho y^2}{\mu} S \quad (2.24)$$

and  $Re_\theta$  therefore eliminating the need for the integration of the boundary layer. This is possible because  $Re_v$  is a local quantity and can therefore be calculated at every grid point of unstructured code (F.R. Menter, Esch, and Kubacki 2002). Based on this observation the  $\gamma - Re_\theta$  model was introduced (Robin Blair Langtry 2006). It uses an empirical correlation to capture non-local free stream conditions and calculate the transition onset momentum thickness Reynolds number  $\tilde{Re}_{\theta t}$ . By treating  $\tilde{Re}_{\theta t}$  as a transported scalar quantity, it can

## 2. THEORETICAL BACKGROUND

---

be used in a transport equation. A second transport equation calculates the intermittency  $\gamma$  to locally trigger transition (Robin Blair Langtry 2006).

### 2.5.2 Transition Model Formulation

A full description of the model is given in (Robin B. Langtry and Florian R. Menter 2009).

The Intermittency  $\gamma$  can be interpreted as the probability that a given point in the flow field is turbulent. Its transport equation for the reads

$$\frac{\partial(\rho\gamma)}{\partial t} + \frac{\partial(\rho U_j \gamma)}{\partial x_j} = P_\gamma - E_\gamma + \frac{\partial}{\partial x_j} \left[ \left( \mu + \frac{\mu_t}{\sigma_f} \right) \frac{\partial \gamma}{\partial x_j} \right] \quad (2.25)$$

The source is defined as

$$P_\gamma = F_{length} c_{a1} \rho S [\gamma F_{onset}]^{0.5} (1 - c_{e1} \gamma) \quad (2.26)$$

where  $F_{length}$  controls the length, and  $F_{onset}$  the location of the transition region. Both  $F_{length}$  and  $F_{onset}$  are calculated using empirical correlations (see Appendix A), and take the solution of the  $\tilde{Re}_{\theta t}$  transport equations as input.

$$F_{length} = f(\tilde{Re}_{\theta t}) \quad (2.27)$$

$$F_{onset} = f(\tilde{Re}_{\theta c}) \quad (2.28)$$

$F_{onset}$  activates the production of intermittency  $\gamma$ . It is designed to assume values between 0 in laminar regions, and 1 for each point of the flow field where the transition onset criteria is met. The sink term is defined as

$$E_\gamma = c_{a2} \rho \Omega \gamma F_{turb} (c_{e2} \gamma - 1) \quad (2.29)$$

$F_{turb}$  is used to disable the destruction source outside of a laminar boundary layer or in

## 2. THEORETICAL BACKGROUND

---

the viscous sublayer.

$$F_{turb} = e^{-(\frac{R_T}{4})^4} \quad (2.30)$$

$R_T$  is the viscosity ratio specified as

$$R_T = \frac{\rho k}{\mu \omega} \quad (2.31)$$

In order to calculate  $\gamma$ , non-local free-stream conditions need to be captured. This is achieved by solving the transport equation for the transition momentum-thickness Reynolds number

$$\frac{\partial(\rho \tilde{R}e_{\theta t})}{\partial t} + \frac{\partial(\rho U_j \tilde{R}e_{\theta t})}{\partial x_j} = P_{\theta t} + \frac{\partial}{\partial x_j} \left[ \sigma_{\theta t} (\mu + \mu_t) \frac{\partial(\tilde{R}e_{\theta t})}{\partial x_j} \right] \quad (2.32)$$

Outside the boundary layer the source term is designed to force the transported scalar  $\tilde{R}e_{\theta t}$  to match the local value of  $Re_{\theta t}$ , which is obtained from empirical correlations (see Appendix A).

$$P_{\theta t} = c_{\theta t} \frac{\rho}{t} (Re_{\theta t} - \tilde{R}e_{\theta t})(1.0 - F_{\theta t}) \quad (2.33)$$

$Re_{\theta t}$  is calculated based on free stream information namely the turbulence intensity  $Tu$  and the pressure gradient  $\lambda_\theta$ .

$$Tu = 100 \frac{\sqrt{2k/3}}{U} \quad (2.34)$$

$$\lambda_\theta = \frac{\rho \theta^2}{\mu} \frac{dU}{ds} \quad (2.35)$$

where  $dU/ds$  is the stream-wise acceleration.  $F_{\theta t}$  is a blending function equal to zero in the free stream and one in the boundary layer.

$$F_{\theta t} = \min \left( \max \left( F_{wake} e^{-(y/\delta)^4}, 1.0 - \left( \frac{\gamma - 1/c_{e2}}{1.0 - 1/c_{e2}} \right)^2 \right), 1.0 \right) \quad (2.36)$$

The  $F_{wake}$  function ensures that the blending function is not active in the wake regions

downstream of an airfoil or blade.

$$F_{wake} = e^{-\left(\frac{Re_{\omega}}{1E+5}\right)^2} \quad (2.37)$$

### 2.5.3 Closure Coefficients

In order to calibrate the transition model for internal pipe flow Abraham, Sparrow, and J. Tong (2008) proposed to adjust two closure coefficients. In doing so, the range of transition for the friction factor was increased to  $Re \sim 4000$ .

- $c_{e1} = 1.0$  (Equation 2.26) limits the value of  $\gamma$  to a maximum of 1. Since a value below zero or above one is not physical this parameter should not be changed.
- $c_{a1} = 2.0$  (Equation 2.26)
- $c_{e2} = 50$  (Equation 2.29) controls the lower limit of the intermittency. The value of 50 results in a lower limit of 0.02. Abraham, Sparrow, and J. Tong (2008) changed this value to 70. Increasing this value will likely result in an extended transition region.
- $c_{a2} = 0.06$  (Equation 2.29) controls the strength of the destruction term and makes sure that it is smaller than the production term.
- $\sigma_f = 1.0$  (Equation 2.25).
- $c_{\theta t} = 0.03$  (Equation 2.33) controls the magnitude of the source term. Abraham, Sparrow, and J. Tong (2008) changed the value to 0.015. Decreasing will likely increase the transition region.
- $\sigma_{\theta t} = 2.0$  (Equation 2.32) Diffusion coefficient. Controls the lag between the local value of  $Re_{\theta t}$  in the boundary layer and that in the freestream. The larger the value the less sensitive the transition model is to history effects.

### 2.5.4 Coupling with the $k - \omega - SST$ Model

As illustrated in Figure 4, the information passed from the transition to the turbulence model is the intermittency  $\gamma$ . In order for them to interact some modifications are necessary to the formulation of the  $k-\omega-SST$  model (Robin B. Langtry and Florian R. Menter 2009). The most important is the adjustment of the production term in the turbulent kinetic energy transport equation Equation 2.17, which is labeled  $P_k$  in the following equation.

$$\tilde{P}_k = \gamma * P_k \quad (2.38)$$

Therefore, if a fully laminar flow is present ( $\gamma = 0$ ) the production of turbulent kinetic energy is disabled. On the other hand in a fully turbulent flow ( $\gamma = 1$ ) the transition model does not influence the underlying turbulence model.

## 2.6 Laser Doppler Velocimetry (LDV)

Laser Doppler Velocimetry (LDV) is an optical measurement technique used to determine fluid flow velocity. It is based on the Doppler Effect, relating the change in wavelength of a reflected signal to the targeted objects relative velocity (Yeh and Cummins 1964). Key benefits of this measurement technique are the possibility to measure fluid flow non-intrusive, calibration-free with a high sampling frequency (Beauvais 1994). Limitations include the need for suitable seeding particles and expensive equipment, as well as optical access to the fluid medium (Nabavi and Siddiqui 2010).

### 2.6.1 Measurement principle

In a dual beam system two coherent laser beams with wavelength  $\lambda$  form a measurement volume at their focal point (Figure 5). The crossing of the beams creates a fringe pattern with light and dark areas. The distance  $d$  between these areas can be calculated using Equation 2.39 (Boutier and Most 2012)

$$d = \frac{\lambda}{2 * \sin(\phi/2)} \quad (2.39)$$

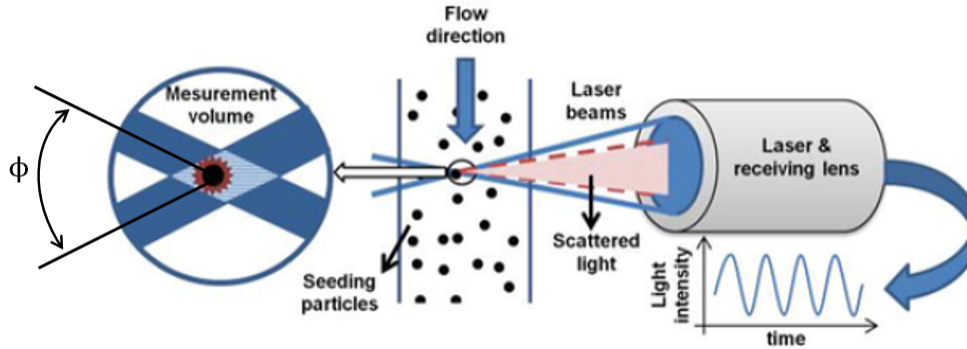


Figure 5: Measurement principle of LDV (Haddadi et al. 2018)

If a seeding particle passes through the fringe pattern it will scatter a signal with frequency  $f_d$ . The velocity  $v$  of the particle is therefore calculated as (Boutier and Most 2012)

$$v = \frac{f_d * \lambda}{2 * \sin(\phi/2)} \quad (2.40)$$

Two particles with the same velocity but opposite direction will have the same frequency value  $f_d$ . In order to measure the direction of the flow, one of the laser beams is therefore shifted by a frequency  $f_0$ , creating a moving fringe pattern. A particle with zero velocity will result in a detected frequency  $f_0$  while any movement of the particle will result in a frequency larger or smaller than  $f_0$ , depending on the direction relative to the fringe movement (McKeon et al. 2007).

$$v = \frac{(f_d - f_0) * \lambda}{2 * \sin(\phi/2)} \quad (2.41)$$

### 2.6.2 Seeding

Flow seeding is essential since LDV measures the velocity of particles passing through the measurement volume. In order to claim that particle velocity relates to fluid velocity the

## 2. THEORETICAL BACKGROUND

---

particles have to follow the flow field. The Stokes number  $St$  (Equation 2.42) compares the particle inertia to the viscous forces of the fluid (Gondret, Lance, and Petit 2002).

$$St = \frac{2 * \rho_p * U * R}{9 * \mu} \quad (2.42)$$

If  $St < 0.1$  the flow tracing accuracy error can be assumed below 1% (McKeon et al. 2007). Another desired property of seeding particles is the ability to scatter light. The scattering ability of a particle increases with its size, which is contrary to the demand of small particles for flow tracking (McKeon et al. 2007). Hollow glass particles (SPHERICEL<sup>®</sup> 110P8, Osthoff Omega Group) are selected for seeding due to their size, density  $\rho_p = 1.1 \text{ kg/m}^3$  and material. Assuming a water viscosity of  $\mu = 0.0010022 \text{ Pas}$  and velocity of  $U = 0.44 \text{ m/s}$ , which is the highest mean velocity calculated prior to experiments, the Stokes number is calculated based on the particle size distribution supplied by the manufacturer (Table 2).

Table 2: Stokes number based on particle size distribution for SPHERICEL<sup>®</sup> 110P8

Cumulative	Diameter	St
%	$\mu\text{m}$	-
10	5	0.000271
50	10	0.000542
90	21	0.001138
97	25	0.001355

### 2.6.3 LDV Components

Components of the LDV system are depicted in Figure 6. A 300 mW, air cooled Argon Ion Laser (CVI Melles-Griot) is split into a 488 nm blue and 514.8 nm green beam, followed by a frequency shift of 35 MHz using a Bragg cell. The signal is transported via fiber optic cables and focused at the point of interest. A TSI TR260 fiber-optic probe (350 mm

## 2. THEORETICAL BACKGROUND

focal length, 61 mm diameter) collects the scattered signal in backscatter mode (180°). Photo-multipliers (TSI PDM 1000 Photomultiplier System) detect the photons which are analyzed at the signal processor (TSI FSA 4000 3-channel digital burst processor, 800 MHz sampling frequency, 175 MHz max. Doppler frequency). Evaluation of the acquired data was performed using TSI FlowSizer (version 3.0.0.0, 2011) software.

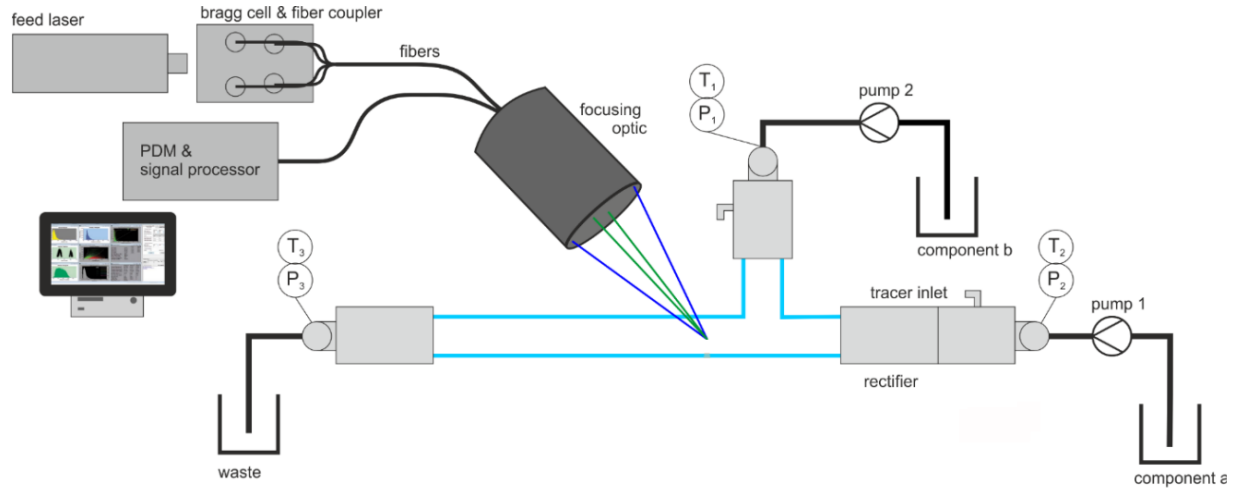


Figure 6: Components of the LDV system and experimental setup (Haddadi et al. 2018)

In the current setup the LDV probe is mounted on a traverse system (Figure 17) which enables movement in X,Y and Z direction as well as pre-programming a set of desired measurement points. The setup is accompanied by an optional simultaneous concentration measurement using Raman spectroscopy (Haddadi et al. 2018).

### 2.6.4 Evaluation of measurement data

Each time a seeding particle passing through the fringe pattern creates a detectable signal it is referred to as a "valid count", resulting in a velocity distribution for each measurement point (Figure 7). Based on this distribution, the average velocity for each component  $i$  at a measurement position is calculated as

$$\bar{U}_i = \frac{1}{n} \sum_{j=1}^n (U_{i,j}) \quad (2.43)$$

## 2. THEORETICAL BACKGROUND

---

with  $n$  being the number of valid counts.

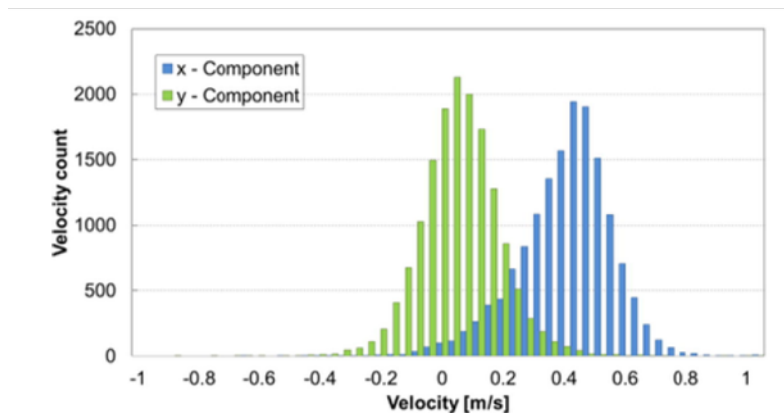


Figure 7: LDV velocity distribution. Result of one measurement point (Haddadi et al. 2018)

The turbulent kinetic energy  $k$  is a measure of velocity fluctuations (Equation 2.11). For two measured velocity components the calculation is performed as

$$k = \frac{3}{4} \frac{1}{n} \sum_{i=1}^n ((U_{1,i} - \bar{U}_1)^2 + (U_{2,i} - \bar{U}_1)^2) \quad (2.44)$$

assuming isotropic turbulence. The third velocity component ( $Z$ ) is considered as a mean value of the other two components. High number of valid counts are therefore desirable for a trustworthy calculation of the pointwise velocity and turbulent kinetic energy.

## 2.7 Design of Experiments (DoE)

### 2.7.1 Introduction to DoE

Aim of this work is to identify the optimum value combination of the closure coefficients present in the turbulence model. This task could be achieved by arbitrarily changing one model constant at a time, trying to find the best possible combination. However, this unorganized approach yields two major disadvantages. First, it would require enormous amounts of time and resources. Second, if there are interactions between two of the con-

## 2. THEORETICAL BACKGROUND

---

starts, the optimum combination would likely be missed.

Design of Experiments on the other hand provides an organized plan for collecting data in a way that it can be analyzed statistically, with a minimum of resources. This is achieved by fitting a *Regression model*, containing the *Factors* of interest and their according *Coefficients*, to an experimental *Response* using the least squares method (Figure 8).

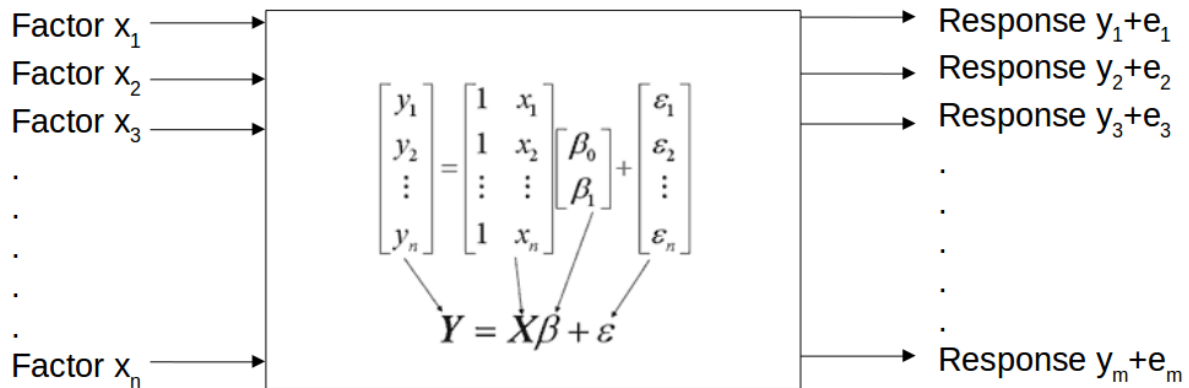


Figure 8: Fitting a simple model to experimental data containing Factors  $x_n$ , Responses  $y_m$ , Coefficients  $\beta_i$  and the model error  $e_m$ .

When discussing DoE it is practical to define some frequently used terms (Eriksson 2008):

**Factor** Factors are input variables whose influence on the outcome is investigated. In the present case the closure coefficients represent the factors. A classification can be made in controllable (e.g. inlet velocity) and uncontrollable (e.g. ambient pressure in experiments), as well as qualitative (e.g. ON or OFF) and quantitative (e.g. velocity, pressure) factors. When using DoE in connection with CFD, all factors are controllable.

**Level** The number of investigated values for each factor is referred to as level. An increasing number of levels increases accuracy at the cost of additional experiments. Most common are 2-level designs where each factor is investigated at a high (+) and low (-) value.

## 2. THEORETICAL BACKGROUND

---

**Design** The design is a set of experimental runs, determined prior to experiments, that allows fitting of a model and estimation of effects. A design that includes all possible combinations is referred to as "Full factorial"-design. The common notation for these designs is " $2^g$ " where 2 refers to the number of levels and  $g$  to the number of factors. One example of such design is given in Figure 9 where each blue point represents a factor combination.

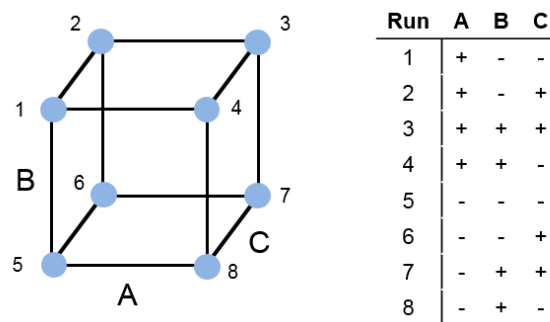


Figure 9: Geometrical representation and design of a three factor full factorial design (without center points)

**Response** The response is the output variable or depended variable of the process. Equally to factors, it can be classified as qualitative or quantitative. The present work defines the response as a measure of turbulent kinetic energy.

**Regression Model** A regression model represents the mathematical link between pre-defined factors and the computed responses. Generally, a simple model used on complex data will miss important interactions and a complex model used on simple data will lead to over-fitting. Since the model is selected beforehand it is therefore crucial to check the model fit before using it for predictions (Lawson 2015).

Linear model

$$y = \beta_0 + x_1\beta_1 + x_2\beta_2 + \dots + e \quad (2.45)$$

Interaction model

$$y = \beta_0 + x_1\beta_1 + x_2\beta_2 + x_1x_2\beta_{12} + \dots + e \tag{2.46}$$

Quadratic model

$$y = \beta_0 + x_1\beta_1 + x_2\beta_2 + x_1^2\beta_{11} + x_2^2\beta_{22} + x_1x_2\beta_{12} + \dots + e \tag{2.47}$$

### 2.7.2 Fractional Factorial Design

A disadvantage of full factorial designs is the exponentially increasing number of experiments. A  $2^8$  design for example would require 256 runs to complete. A method to decrease the number of experimental runs is the use of "Fractional factorial"- Designs ( $2^{g-b}$ ) which reduce the number of experiments at the expense of model accuracy (Eriksson 2008), (Lawson 2015). A graphical interpretation of the concept is given in Figure 10. The full  $2^g$  design is split  $b$  times, reducing the number of experiments. This reduction however comes at the cost of *confounding*, meaning that the main factor effects can no longer be computed completely free from one another.

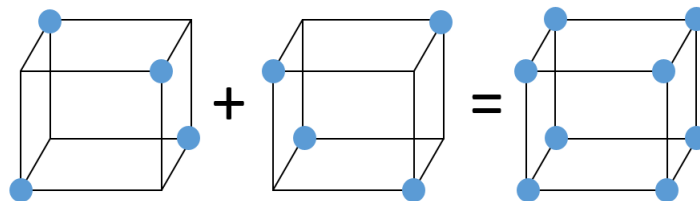


Figure 10: Graphical interpretation of a  $2^{3-1}$  ( $g = 3, b = 1$ ) fractional factorial design.

The confounding pattern of a  $2^{4-1}$  design is shown in Table 3. All the main effects,  $A, B, C, D$ , are confounded with three factor interaction terms  $A:B:C, A:C:D, A:B:D$  and  $A:B:C$  respectively. However these three factor interaction terms are usually small compared to the main effects and can therefore be assumed to be of negligible relevance (Eriksson 2008). The two factor interactions are confounded with each other and therefore

## 2. THEORETICAL BACKGROUND

---

the situation is more complex.

Table 3: Confounding of factors in a  $2^{4-1}$  fractional factorial design

$$\begin{aligned}
 A &= B:C:D \\
 B &= A:C:D \\
 C &= A:B:D \\
 D &= A:B:C \\
 A:B &= C:D \\
 A:C &= B:D \\
 A:D &= B:C
 \end{aligned}$$

A degree of confounding is the *resolution* of a fractional factorial design. The resolution of a design is the smallest order interaction that the main effect is confounded with, plus one (e.g. resolution III signifies that all main effects are aliased with 2 factor interactions). For Screening purposes, resolution III or IV designs are viable. Figure 11 summarizes the benefits and shortcomings of choosing a fractional factorial design.

<b>4</b>	$2^{3-1}$ , III				
<b>8</b>	$2^3$	$2^{4-1}$ , IV	$2^{5-2}$ , III	$2^{6-3}$ , III	$2^{7-4}$ , III
<b>16</b>	$2^3$	$2^4$	$2^{5-1}$ , V	$2^{6-2}$ , VI	$2^{7-3}$ , VI
<b>32</b>	$2^3$	$2^4$	$2^5$	$2^{6-1}$ , VI	$2^{7-2}$ , VI
<b>64</b>	$2^3$	$2^4$	$2^5$	$2^6$	$2^{7-1}$ , VII

Figure 11: Different fractional factorial designs and their resolution (roman numerals). Leftmost column indicates the required number of runs.

### 2.7.3 Objectives of DoE

Combining the strengths of full and fractional factorial designs, a workflow can be determined that yields detailed results with a minimum amount of simulations (Lawson 2015). This process is illustrated in Figure 12, including the main objectives of each step.

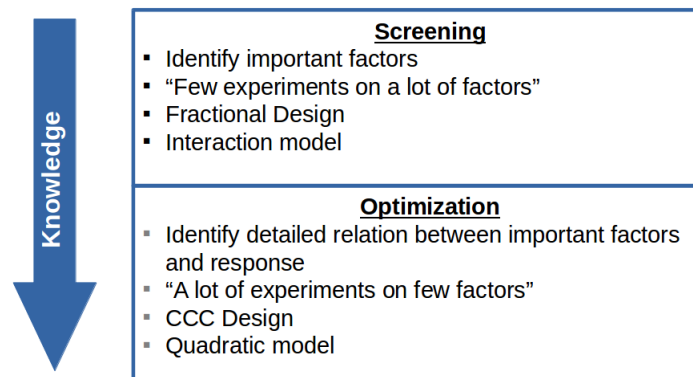


Figure 12: Outline of the DoE workflow applied in this work

**Screening** At the start of the investigation there is usually little information about the influence of factor on a desired response. Therefore it is advisable to reduce the number of factor in a first "*Screening*" step. This reduction of factor is achieved by utilizing fractional factorial designs, which allows for a broad investigation of factor with reasonable experimental effort. This way the most important factors can be identified and passed on to the second "*Optimization*" step.

**Optimization** Optimization designs identify a detailed relation between the selected factor and the response. They are also referred to as Response Surface Methodology (RSM) designs. This work uses the Central Composite Circumscribed (CCC) design, which is visualized in Figure 32 for three factor. The CCC design is based on a full factorial (blue) design, but augments it by introducing axial points (red). Therefore every factor is investigated at five levels (-1.68, -1, 0, +1, +1.68) (Lawson 2015). RSM designs usually fit quadratic models.

### 2.7.4 Evaluation of Raw Data

Selecting the correct design is one part of DoE. The second part involves evaluation of the obtained data.

In DoE, it is advantageous if the response data is normally distributed, as it enhances model quality. A quick way to check this requirement is the use of Boxplots. Figure 13 exemplifies the difference in normally distributed data (A) and tailed data (B). The thick black line represents the median value. If the raw data appears as shown in (B), it is advisable to perform a logarithmic transformation. If a transformation does not yield the desired result, the factor levels should be changed in order to obtain superior data.

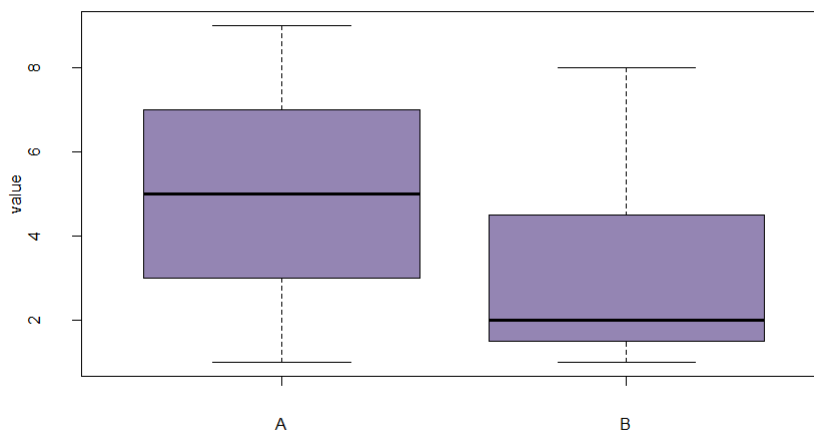


Figure 13: Boxplot of normally distributed (A) and tailed data (B)

### 2.7.5 Model Quality

Once satisfied with the quality of response data, the model can be fitted. It is important to keep in mind that a DoE constructed in  $R$  will always fit a model to the provided data. An output however does not equal a valid model. The model quality needs to be examined before predictions are made. An example output of an interaction model fitted to a  $2^3$  full factorial design is given in Table 4.

## 2. THEORETICAL BACKGROUND

---

Table 4: Example output of R for an interaction model

```

Coefficients:
              Estimate Std. Error t value Pr(>|t|)
(Intercept) 668.5625    4.5178 147.985 4.86e-15 ***
A1          -16.8125    4.5178  -3.721 0.00586 **
B1             0.9375    4.5178   0.208 0.84079
C1             5.4375    4.5178   1.204 0.26315
A1:B1        -6.6875    4.5178  -1.480 0.17707
A1:C1        12.5625    4.5178   2.781 0.02390 *
B1:C1         1.8125    4.5178   0.401 0.69878
A1:B1:C1     -5.8125    4.5178  -1.287 0.23422
---
Signif. codes:  0 '***' 0.001 '**' 0.01 '*' 0.05 '.' 0.1 ' ' 1

Residual standard error: 18.07 on 8 degrees of freedom
Multiple R-squared:  0.772,    Adjusted R-squared:  0.5724
F-statistic: 3.869 on 7 and 8 DF,  p-value: 0.0385

```

**Global Model Quality** The global model quality is verified at the bottom section of Table 4. Based on the residual standard error an F-test is performed. If the calculated p value (in this case  $p = 0.0385$ ) is smaller than a chosen  $\alpha$  (e.g.  $\alpha = 0.05$ ), the zero-hypothesis that all coefficients are equal to zero is rejected, meaning that at least one of the factor has a significant influence on the response. The coefficient of determination  $R^2$  is an indicator providing information about the goodness of fit of a Model. If  $R^2 = 1$ , the regression line perfectly fits the data.

$$\bar{y} = \frac{1}{n} \sum_{i=1}^n y_i \quad (2.48)$$

$$SumSquareError = SSE = \sum_{i=1}^n (y_i - \hat{y}_i)^2 \quad (2.49)$$

$$SumSquareTotal = SST = \sum_{i=1}^n (y_i - \bar{y})^2 \quad (2.50)$$

$$R^2 = 1 - \frac{SSE}{SST} \quad (2.51) \quad 0 \leq R^2 \leq 1 \quad (2.52)$$

$y_i$ ...Response variable of experiment i

$\hat{y}_i$ ...Predicted value of response variable of experiment i

## 2. THEORETICAL BACKGROUND

---

$\bar{y}...$  Mean value of response variable

**t-Test** Based on the residual variance  $\hat{\sigma}^2$  with  $n$  observations and  $p$  parameters

$$\hat{\sigma}^2 = \frac{SSE}{n - p} \quad (2.53)$$

and the variance of each coefficient, the standard error is computed. This standard error then is used to test each coefficient for its significance using a t-statistic. The zero hypothesis, that the tested coefficient is equal to zero is rejected if the  $Pr(> |t|)$ -value is smaller than a chosen  $\alpha$ -level. In this example the main effect  $A1$  and the interaction term  $A1 : C1$  are estimated with a certainty of 99% and 95% respectively.

**Evaluation of fractional factorial designs** The model output of a fractional factorial design (Table 5) is different in comparison to the output of a full factorial design (Table 4). In this example eight experiments ( $2^{4-1}$ ) are carried out and an interaction model was fitted. Thus eight experiments and eight coefficients are present, resulting in  $R^2 = 1$ , a perfect fit. Therefore no variance of the coefficient can be computed and no t-statistic can be performed, as indicated by "NA".

## 2. THEORETICAL BACKGROUND

---

Table 5: Example output of an interaction model fitted to a fractional factorial design

```

Residuals:
ALL 8 residuals are 0: no residual degrees of freedom!

Coefficients: (7 not defined because of singularities)
              Estimate Std. Error t value Pr(>|t|)
(Intercept)  0.68875      NA      NA      NA
A1           -0.09375      NA      NA      NA
B1           -0.10875      NA      NA      NA
C1           -0.03625      NA      NA      NA
D1            0.02875      NA      NA      NA
A1:B1        -0.03625      NA      NA      NA
A1:C1         0.05125      NA      NA      NA
A1:D1        -0.03375      NA      NA      NA
B1:C1         NA          NA      NA      NA
B1:D1         NA          NA      NA      NA
C1:D1         NA          NA      NA      NA
A1:B1:C1      NA          NA      NA      NA
A1:B1:D1      NA          NA      NA      NA
A1:C1:D1      NA          NA      NA      NA
B1:C1:D1      NA          NA      NA      NA

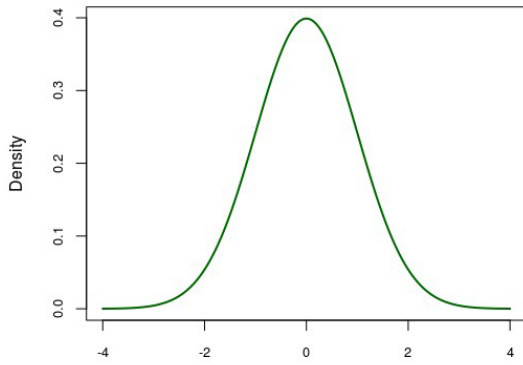
Residual standard error: NaN on 0 degrees of freedom
Multiple R-squared: 1, Adjusted R-squared: NaN
F-statistic: NaN on 7 and 0 DF, p-value: NA

```

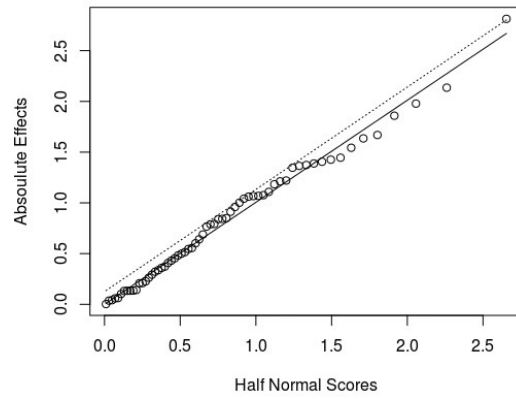
A different approach to determine the significance of a coefficient is needed, for example the *Half-normal plot*. The interpretation of the Half-normal plot is illustrated in Figure 14. Assuming that all coefficients are caused by white noise in the response variable, (i.e. no factor has an effect on the response), the resulting coefficients are normally distributed around a mean value, and therefore close to the near-zero line in the half normal plot (Figure 14b). All coefficients that are not only caused by white noise are typically displaced well off the line (Figure 14c).

## 2. THEORETICAL BACKGROUND

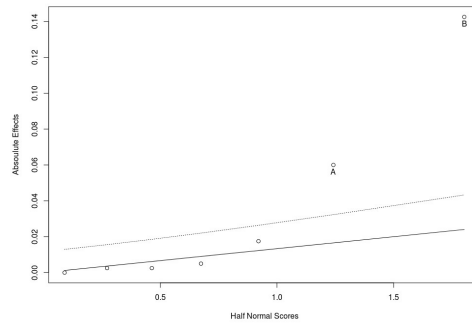
---



(a) PDF of standard distribution



(b) Half-normal plot of standard distribution



(c) Half-normal plot with outliers

Figure 14: Interpretation of the Half-normal plot

### 3 Experimental Investigation

#### 3.1 Investigated Flow

The mixing of turbulent and laminar flow in a T-junction, rectangular glass channel is investigated. The dimensions of the channel are illustrated in Figure 15. The turbulent flow enters the channel from inlet 1, the laminar flow from inlet 2. In order to remove flow history effects, stratifiers are included in the setup for both inlets. Each stratifier consists of 30 pipes with a diameter of 1 mm and a length of 50 mm. Water is selected as experimental fluid considering its availability, cost, non-toxicity and fluid properties. Using water for both inlets also enables recirculation of the outlet flow. Therefore longer experiment times and subsequently more measurements are possible, as opposed to multispecie experiments which are limited by material consumption.

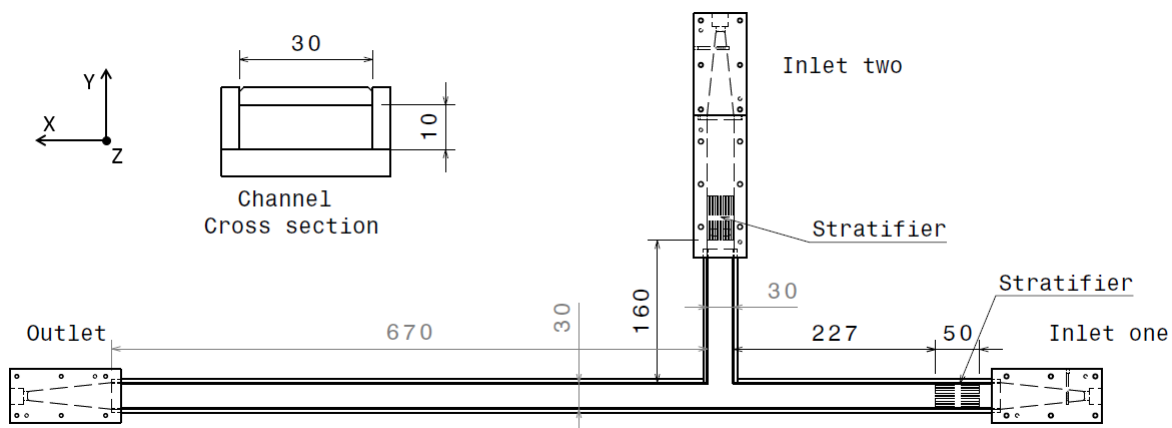


Figure 15: Channel dimensions in mm

The flowrates (Table 6) for the laminar and turbulent section of the channel are constant throughout the experiment.

The Reynolds number (Equation 2.1) is based on the hydraulic diameter  $d_h = 2ab/a+b$ , where  $a$  and  $b$  are the width and height of the glass channel. Water properties (Table 7) are assumed constant over the course of the experiment.

### 3. EXPERIMENTAL INVESTIGATION

Table 6: Calculated flowrates for the different channel sections

	Flowrate [kg/s]	Flowrate [l/min]	Re [-]
Inlet 1	0.0998	6	4980
Inlet 2	0.0199	1.2	996
Outlet	0.1197	7.2	5976

Table 7: Water properties for 20°C

Water Properties		
Density	998.21	$kg/m^3$
Kinematic viscosity	0.000001004	$m^2/s$
Hydraulic diameter	0.015	m

### 3.2 LDV- Measurement Positions

A total of five 2D profiles at the inlets, outlet and mixing sections are investigated. Figure 16.

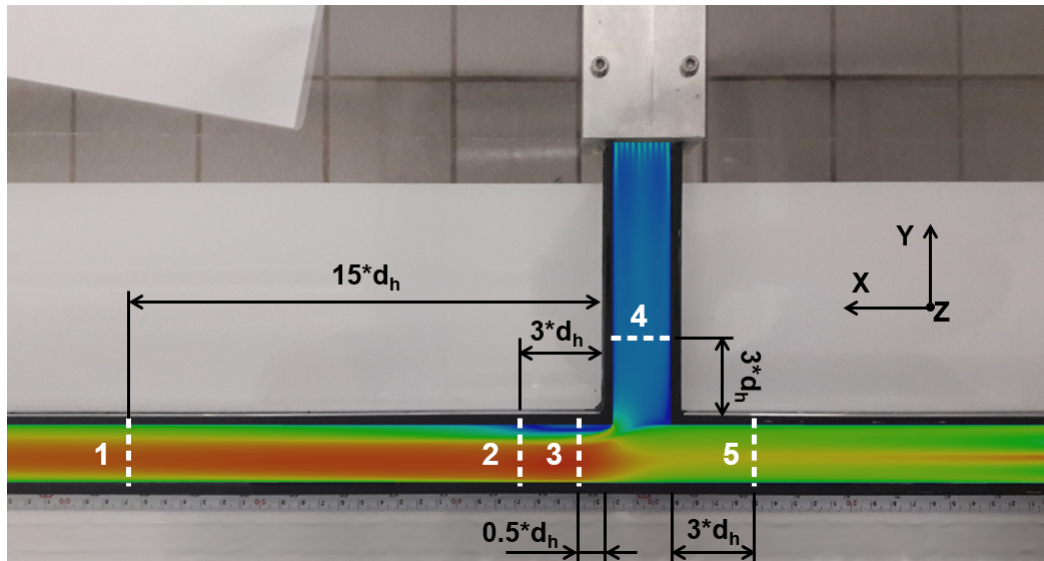


Figure 16: Position of the five measurement profiles

### 3. EXPERIMENTAL INVESTIGATION

---

Due to the more complex flow field, the profiles at the mixing section are expected to require a higher resolution in order to capture all flow conditions accurately. Therefore a resolution of 341 measurement points is applied for profile 2 and profile 3, equal to a spacing of 1 mm, and a lower resolution of 96 measurement points for profiles 1, profile 4 and profile 5, equal to a spacing of 2 mm (Table 8).

Table 8: Measurement profiles and resolution

	<b>Position</b>	<b>Points (X)</b>	<b>Points (Y)</b>	<b>Points (Z)</b>	<b>Total</b>
Profile 1	Outlet	1	11	6	96
Profile 2	Mixing Section	1	31	11	341
Profile 3	Mixing Section	1	31	11	341
Profile 4	Laminar Inlet	11	1	6	96
Profile 5	Turbulent Inlet	1	11	6	96

### 3.3 Experimental Setup

The complete setup is depicted in Figure 17. As described in Section 2.6, the LDV probe is mounted on a traverse system, allowing for quick adjustment of the measurement position. A file that includes all measurement points is created using a C++ code and forwarded to the traverse control.

### 3. EXPERIMENTAL INVESTIGATION

---

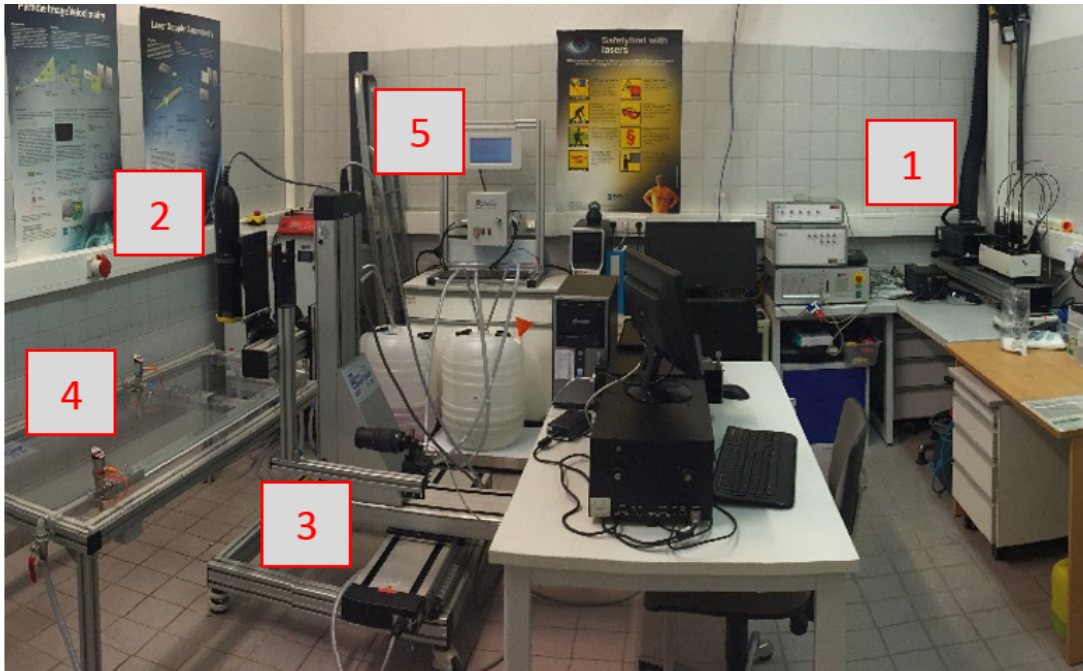


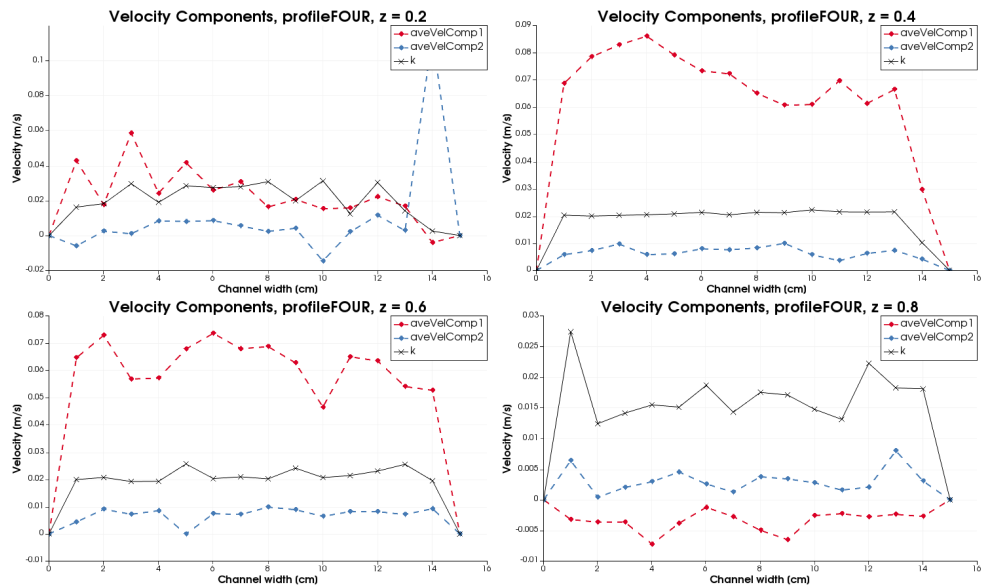
Figure 17: Experimental Setup: 1 = Laser source and Bragg cell, 2 = LDV probe, 3 = Traverse System, 4 = Flow channel, 5 = Pumps and water tank

#### 3.3.1 Estimation of Pump Error

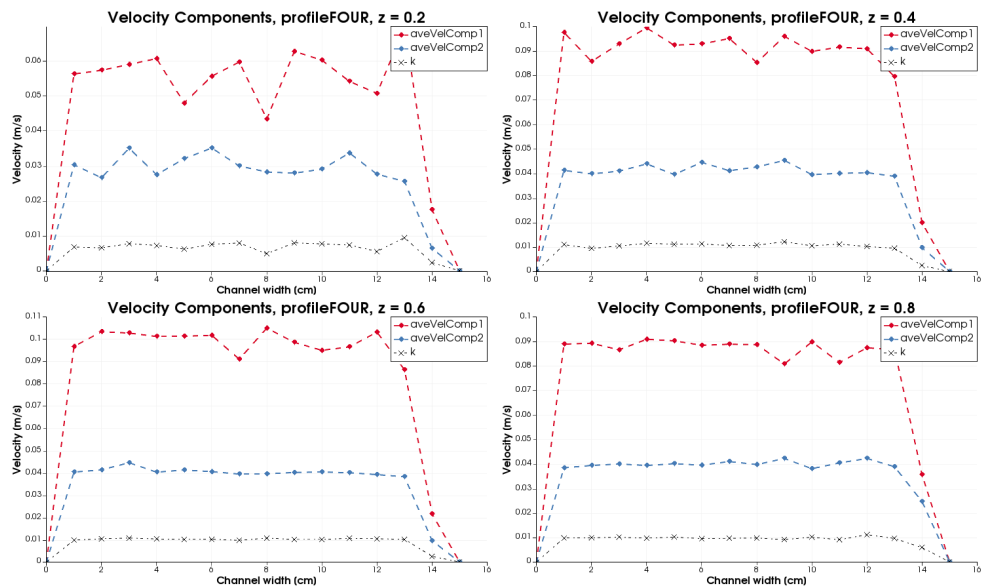
Succeeding the first LDV measurements, a mismatch of simulation results and experiments regarding the velocities, especially in the laminar flow, was observed. Evaluation of the measurement data revealed fluctuating velocity profiles (Figure 18a).

Test measurements were performed at high and low flowrates to estimate the mean flowrate error of the system. An error of 20% at laminar conditions was observed. Investigation of the erroneous pump revealed broken bearings as the cause for the high error. To ensure stable flow rates and therefore reliable measurements a new set of pumps (RoverPompe<sup>®</sup> BE-T 25) was installed in the experimental setup. Repeated measurements revealed that the error was successfully reduced to 4.2% (Table 9).

### 3. EXPERIMENTAL INVESTIGATION



(a) Previous system



(b) Current system

Figure 18: Velocity profiles for the pump error estimation

### 3. EXPERIMENTAL INVESTIGATION

---

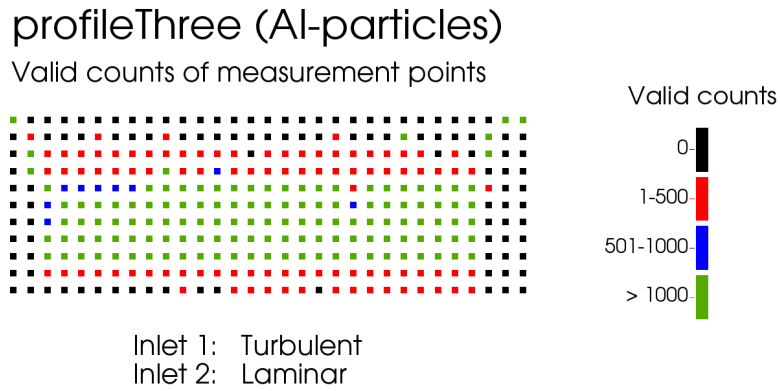
Table 9: Summary of the pump error investigation

<b>Previous system</b>			
	Massflow [kg/s]	Mean Error [%]	Variation Coefficient [-]
Low FR	0.04	20	0.12
High FR	0.08	3.1	0.038
<b>Current system</b>			
Low FR	0.02	4.2	0.05
High FR	0.1	1.6	0.02

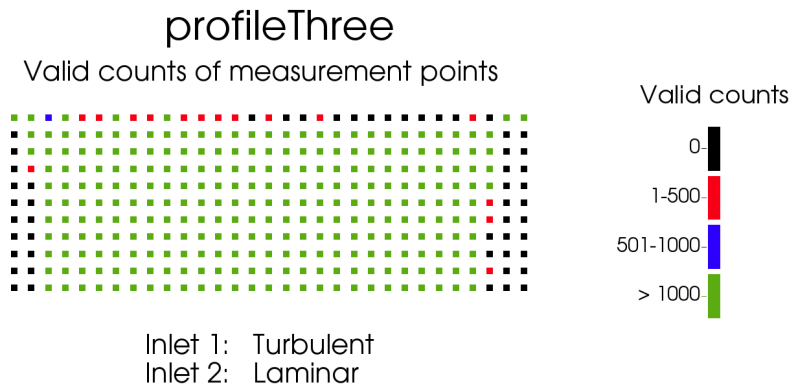
The current pumping system consists of two pumps, each equipped with a variable frequency drive to adjust the flow rate, and a water feed tank in which the seeding particles are dispersed. The glass channel (Figure 15) is fixed on a table and supplied with water by the pumping system. Pressures at the inlets and outlet, as well as water temperature are recorded. Rotameters are installed at both inlets to monitor the flowrates during the course of the experiment.

#### 3.3.2 Selection of Seeding Particles

Initially Aluminum particles (ECKA<sup>®</sup> DG 018, AN <0.045mm) are used for flow seeding. During measurements with recirculating water flow it is observed that the number of valid counts is decreasing over time. Figure 20a depicts the valid counts of each measurement point at the mixing section using Aluminum particles. It is apparent that only the core of the fluid flow is supplied with enough seeding particles during the measurement. An inspection of the channel revealed that, after hours of measurement, the particles tend to settle on the bottom wall, especially in low velocity regions. New seeding material was selected based on the Stokes number (Section 2.6.2). The newly selected hollow glass spheres exhibit satisfactory results Figure 20b.



(a) Aluminium particles



(b) Glass particles

Figure 19: Comparison of aluminium and hollow glass particles for seeding

### 3.4 Measurement Results

Additional experimental conditions are listed in Table 10. During the LDV data collection the flowrates as well as valid counts are monitored. After completion a C++ code is used to extract the obtained data, perform the calculation of the turbulent kinetic energy

### 3. EXPERIMENTAL INVESTIGATION

---

(Section 2.6.4) and convert it to a *ParaView* compatible file format (.vtk). The conversion eases the comparison of measurement with simulation data.

Table 10: Experimental conditions

<b>Pressure drop</b>	0.01 bar
<b>Temperature</b>	23°C
<b>Limit for LDV</b>	3000 valid counts or 9 seconds
<b>Seeding Particles</b>	10 g in 24.8 kg Water

Investigating the valid counts of the recorded profiles (see Appendix B), it is apparent that measurements near the channel walls are not as good as in the rest of the flow field. The reason for the low or zero counts near the side walls is the glue layer that was used in the building process of the channel (Figure 16, black glue layer is visible). The thickness of this layer is about 1 mm, and therefore it blocks the laser light from entering the channel at this position.

Low or zero counts near the top and bottom walls are most likely due to the shape of the LDV measurement volume (Figure 5). Its vertical length of 0.91 mm (Haddadi et al. 2018) exceeds its width, making it harder to position the LDV-probe correctly on the vertical axis. Furthermore, the reflections of the glass impede the data acquisition near the top and bottom walls.

An assumption could be made that the velocity at the first measurement points near the channel walls is close to zero. Interpolation with the first valid measurement point could approximate the missing values. However, including these points in the error estimation would likely distort the outcome of the DoE. Therefore, a reduction of the measurement profiles for the comparison with simulation results is applied. Measurements at height  $z/h = 0.4, 0.5, 0.6$  for Profiles 2 and 3, and  $z/h = 0.4, 0.6, 0.8$  for Profiles 1,4 and 5 are evaluated. Additionally, the zero valid count points near the side walls are discarded.

Measurement results for velocity components and turbulent kinetic energy are illustrated in Appendix E - I (black graphs). A detailed discussion is given in Section 4.3.

## 4 Numerical investigation

A numerical investigation of the flow is performed using OpenFOAM<sup>®</sup>, beginning with a simulation using the standard closure coefficients (= Base Case). The following section will introduce the Base Case setup, and compare its results to the measurements. OpenFOAM<sup>®</sup> determines all case settings in text files that are located in one of three directories:

**0** Boundary conditions for each variable, as well as initial values are established in the *0* directory.

**constant** The *constant* directory is used to set material and mesh properties. It also contains the *turbulenceProperties* file which establishes the values of the closure coefficients.

**system** The *system* directory contains information about the solver (fvSolution), discretization (fvSchemes) and data input/output control (controlDict) settings.

### 4.1 Mesh selection

The first step in obtaining the numerical solution is the discretization of the computational domain, also referred to as *meshing*. An indicator if the discretization near the walls is fine enough is the dimensionless wall-distance  $y^+$  which is calculated using the friction velocity  $u_\tau$  (Pope 2000).

$$u_\tau = \sqrt{\frac{\tau_w}{\rho}} \quad (4.1)$$

$$y^+ = \frac{u_\tau * y}{\nu} \quad (4.2)$$

For the use of the  $\gamma - Re_\theta$  model, a  $y^+$  value of approximately 1 is suggested in order to correctly resolve the boundary layers (Robin B. Langtry and Florian R. Menter 2009). A mesh dependence study using different wall-refinements and cell sizes (Table 11) is

#### 4. NUMERICAL INVESTIGATION

---

performed to investigate the influence on the solution.

Table 11: Properties of the meshes used in the mesh dependence study

		Case 0.0	Case 0.1	Case 0.2
Wall refinement	-	yes	yes	no
Cells	-	2021160	1758108	1064136
$y^+$ (avg)	-	0.6	1.7	10
k (avg)	$m^2s^{-2}$	0.0023	0.0021	0.0457

Results of this study are displayed in Figure 20. Cases with wall-refinement are able to resolve the laminar boundary layer (blue), whereas Case 0.2 predicts an intermittency value of 1 for each cell in the flow field. The course discretization also influences the average k-value extracted from the simulations (Table 11), where Case 0.2 predicts a much higher value compared to the other cases.

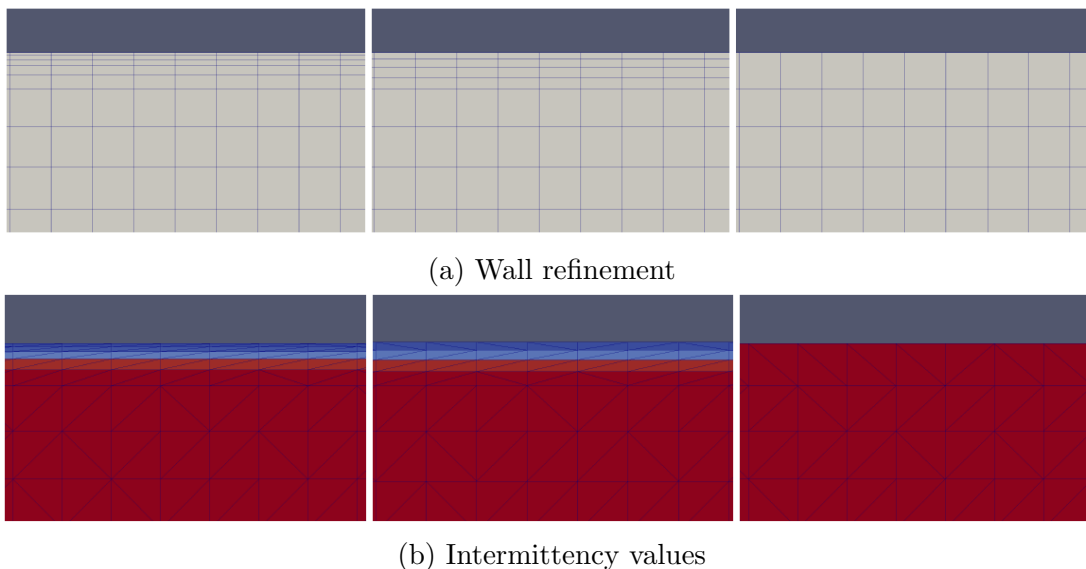


Figure 20: FLTR: Case 0.0, Case 0.1, Case 0.2 (Intermittency: blue = 0, red = 1)

Based on the dependence study, a mesh consisting of 5 296 730 cells with an average  $y^+$  of 1.5 is created using the OpenFOAM<sup>®</sup> mesh generation utility *snappyHexMesh*

(Figure 21).

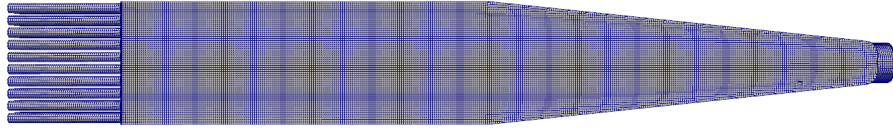


Figure 21: Inlet section and stratifiers of the mesh used for the simulation

## 4.2 Base case - Setup

### 4.2.1 Boundary Conditions

Velocity, pressure and temperature boundary conditions are based on experimental data. Inlet conditions for  $k$  and  $\omega$  are estimated using the turbulence intensity  $Tu$  and length scale  $L$  for fully developed pipe flow. At the wall,  $\omega$  is set to a non-zero number ( $\sim 10^{-30}$ ) therefore avoiding floating point exceptions.

$$k = \frac{3}{2}(U * Tu)^2 \quad (4.3a)$$

$$Tu = 0.16 * Re_{dh}^{-1/8} \quad (4.3b)$$

$$\omega = \sqrt{k/L} \quad (4.4a)$$

$$L = 0.038 * d_h \quad (4.4b)$$

Boundary conditions for  $\gamma$  and  $Re_\theta$  are suggested in Robin B. Langtry and Florian R.

Menter (2009). An intermittency value of 1 for the turbulent inlet, and 0 for laminar inlet is chosen. For the estimation of  $Re_\theta$ , Equation A.3 is solved assuming zero velocity gradient and free stream turbulent velocity. To ensure numerical robustness a value of  $Re_\theta \geq 20$  is suggested. A complete list of boundary conditions is given in Table 12

Table 12: Boundary conditions for the Base Case

		Inlet 1	Inlet 2	Outlet	Wall
Velocity	$m/s$	1.273	0.255	zeroGradient	0
Pressure	$m^2s^{-2}$	zeroGradient	zeroGradient	1e5	zeroGradient
k	$m^2s^{-2}$	0.005	0.000005	zeroGradient	0
$\omega$	$s^{-1}$	200	50	zeroGradient	1e-30
$\gamma$	-	1	0	zeroGradient	zeroGradient
$Re_\theta$	-	20	500	zeroGradient	zeroGradient
T	293	$K$	293	zeroGradient	zeroGradient

#### 4.2.2 Solver settings

A PISO (= Pressure Implicit with Splitting of Operator) algorithm is applied to solve the system of equations. The Courant number  $Co$  (Equation 4.5)

$$Co = \frac{\Delta t * u}{\Delta x} \quad (4.5)$$

is used as a limit for dynamic time stepping. For a given cell size  $\Delta x$  and fluid velocity  $u$  the time step  $\Delta t$  is selected in a way that  $Co \leq 1$ . Due to its size, the case is run in parallel, splitting the computational domain in 48 segments. Computation was performed on the Vienna Scientific Cluster (VSC3). For detailed solver settings see Appendix D.

### 4.3 Base Case - Results

Results are evaluated after 3.9 seconds simulated time, which corresponds to  $\sim 144$  hours of computational runtime. A possible reason for this lengthy runtime are high fluid velocities in the stratifiers, which result in timesteps of  $\sim 10^{-5} s$  due to the  $Co$  limit. In order to check convergence, the  $k$  values are monitored at three different positions in the channel (Figure 22). Since no notable trend is apparent at either position, the simulation results are deemed stable.

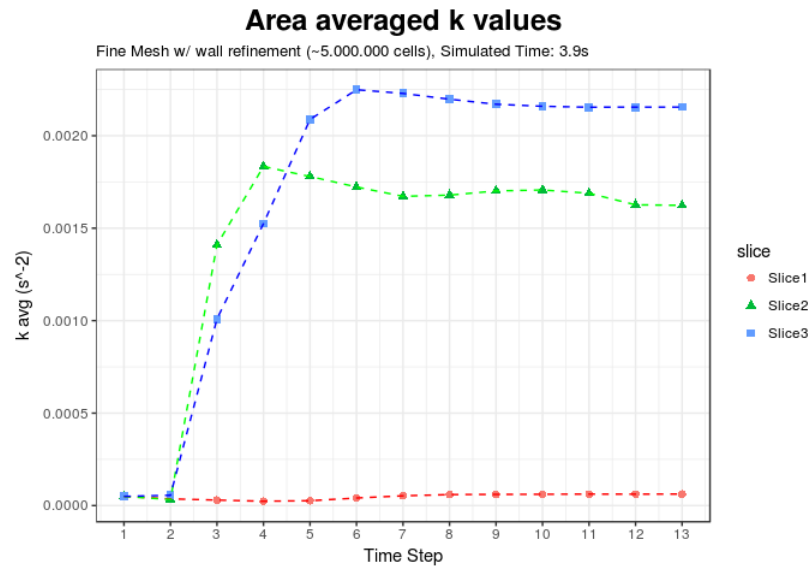


Figure 22: Convergence of the Base Case (Slice 1 = Laminar section, Slice 2 = Turbulent section, Slice 3 = Mixing section)

Qualitative simulation results of the turbulent kinetic energy and velocity field are depicted in Figure 23 for the mixing section.

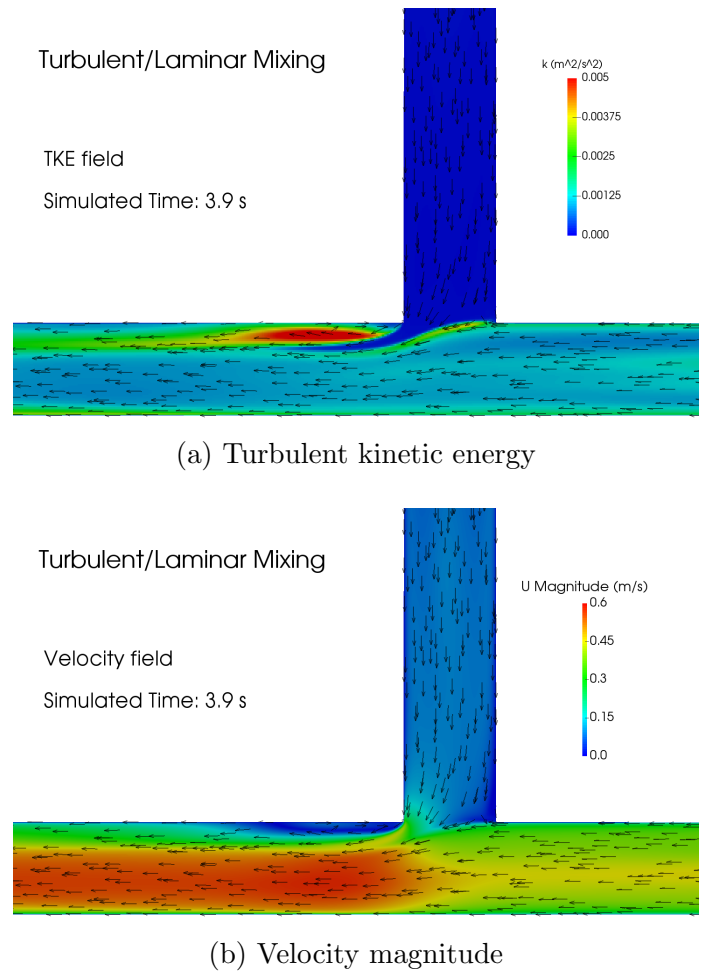


Figure 23: Simulation results of the mixing section

According to the measurement positions (Section 3.2), velocity and turbulent kinetic energy information is extracted and compared to the experimental data. Complete results are presented in Appendix E - I. Black graphs represent measurement results, blue and red graphs the simulation values.

Analyzing the velocities of profile 3, it is evident that LDV-data and simulation results are in very good agreement. Magnitudes of both components, as well as the profile shapes are correctly predicted (Figure 24).

#### 4. NUMERICAL INVESTIGATION

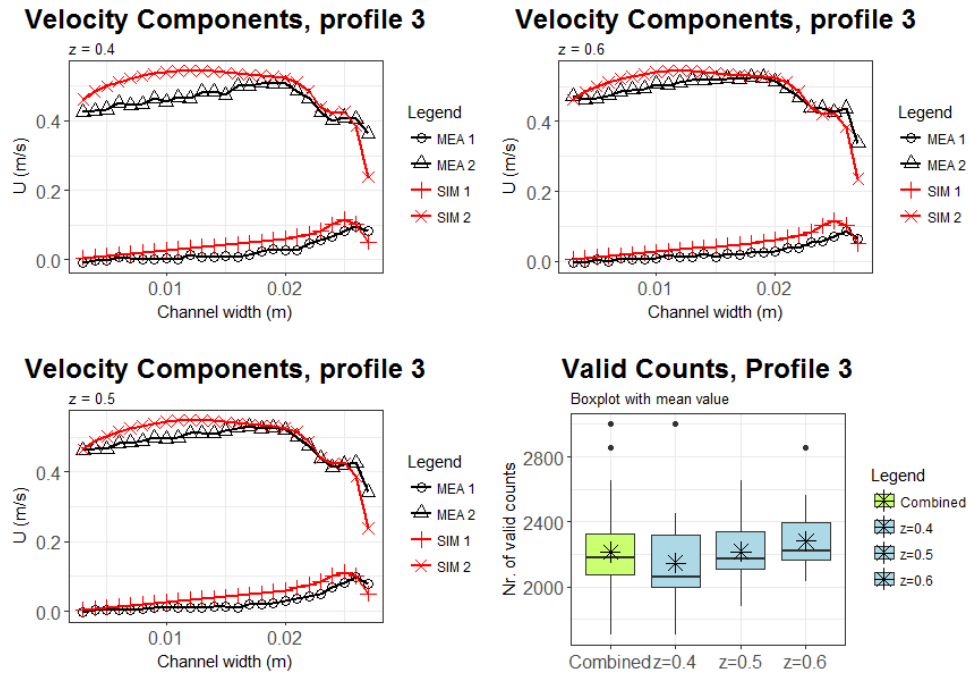


Figure 24: Velocity measurement and base case simulation comparison (Profile 3)

This trend extends to the other profiles as well, the exception being profile 2 (Figure 25a) where the velocity of the main component is overpredicted by  $\sim 30\%$ . Examining the profiles of fully turbulent flow (Figure 25b) it is noticeable that measurements at height  $z/h = 0.8$  differ in their main velocity magnitude, compared to the other profiles where it is equal along all heights.

#### 4. NUMERICAL INVESTIGATION

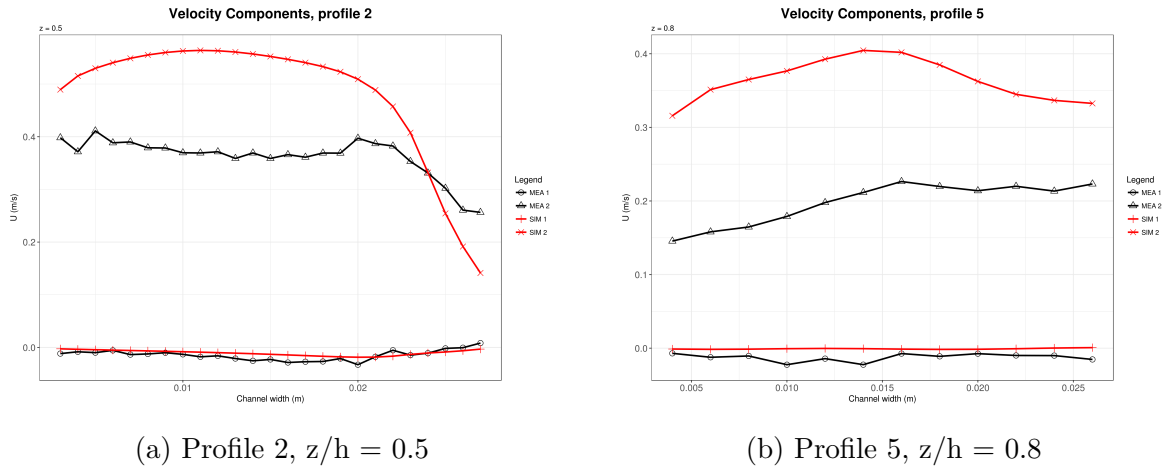


Figure 25: Velocity measurement and base case simulation comparison (Profile 2 and Profile 5)

Turbulent kinetic energy values are underpredicted at all investigated measurement points in the turbulent flow field. Interestingly, the predicted shape of the  $k$ -value graph in profile 3 (Figure 26b) matches the experimental one with great accuracy, whereas the second profile in the mixing section (Figure 26a) is not able to represent the measured shape.

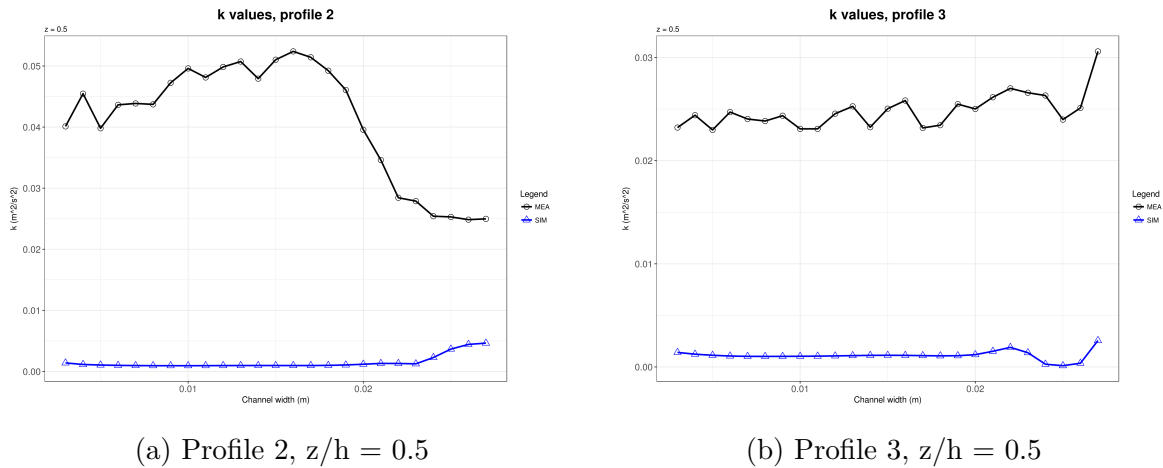


Figure 26: Turbulent kinetic energy measurement and base case simulation comparison (Profile 2 and Profile 3)

A main point of interest is the ability of the  $\gamma - Re_\theta$  transition model to correctly distinguish between turbulent and laminar flow. Results of the laminar section (Figure 27)

#### 4. NUMERICAL INVESTIGATION

clearly show the models ability to suppress the production of turbulent kinetic energy, since the predicted  $k$  values are essentially zero at all parts of this flow. Experimental values however exhibit non-zero  $k$  values, which originate from secondary velocity components. This exemplifies the difficulty to produce a fully laminar flow in experimental conditions. The velocity fluctuations present in this part of the channel are most likely due to imperfections in manufacturing process (i.e. thin glue layer in the channel corners, stratifiers), or pump instability (Section 3.3.1). The primary velocity component again matches the experimental value, indicating a correct measurement.

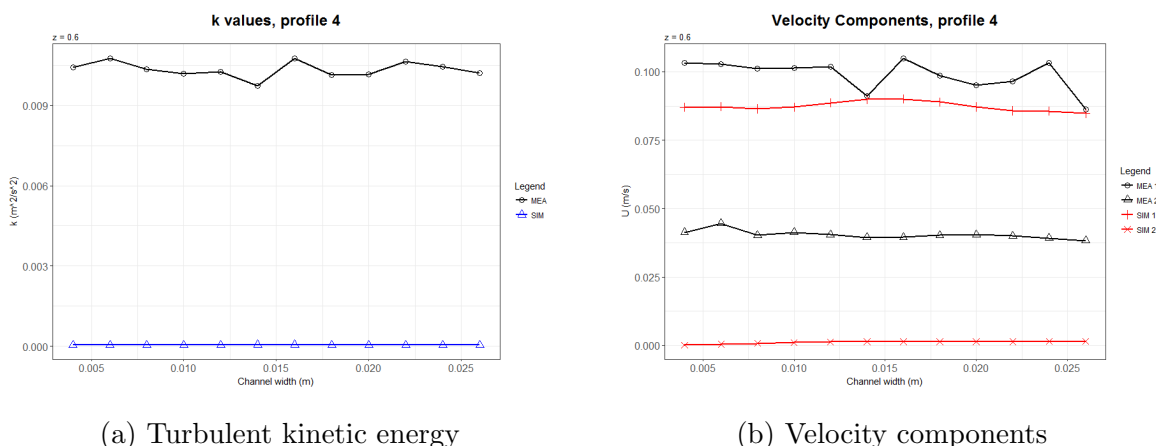


Figure 27: Turbulent kinetic energy and velocity measurement. Base case simulation comparison (Profile 4 at  $z/h = 0.6$ )

Based on these comparisons, it can be concluded that the turbulent kinetic energy is severely underpredicted in the turbulent part of the flow. An effort is therefore made to increase  $k$  by adjusting the standard values of the turbulence model closure coefficients. As discussed in Section 2.5, there are two sets of closure coefficients in the  $\gamma - Re_\theta$  model. The first are the coefficients associated with the transition part of the model, present in the  $\gamma$  and  $Re_\theta$  transport equations, second the closure coefficients relevant for the calculation of  $k$  and  $\omega$ . Since the turbulent kinetic energy is a property of turbulent flow, and the  $\gamma - Re_\theta$  model for  $\gamma = 1$  is essentially the  $k - \omega - SST$  turbulence model, it can be assumed that the coefficients for the transition part of the model have no significant influence on the calculation of  $k$ .

## 5 Screening Simulations

As defined in Section 2.7.3, the first step of a DoE should be the reduction of factors in order to reduce the effort in the following optimization step. In order to reduce the computational effort, a simplified mesh is created for this task.

### 5.1 Simplified Mesh

The high Base Case simulation time of approximately 144 hours is mainly due to the inclusion of the stratifiers. High velocities in the small pipes lead to small time steps as a result of the Courant number limit (Equation 4.5). Since the aim of Screening is to identify significant closure coefficients of the turbulence model, and not to match the experimental results, it is acceptable to simplify the geometry. By omitting the stratifiers, and reducing the number of cells to 2 021 160, a simulation time of  $\sim 16.6$  hours is achieved. The simplified mesh (Figure 28) results in an average  $y^+$  value of 1.12 which is in agreement with the mesh dependence study.

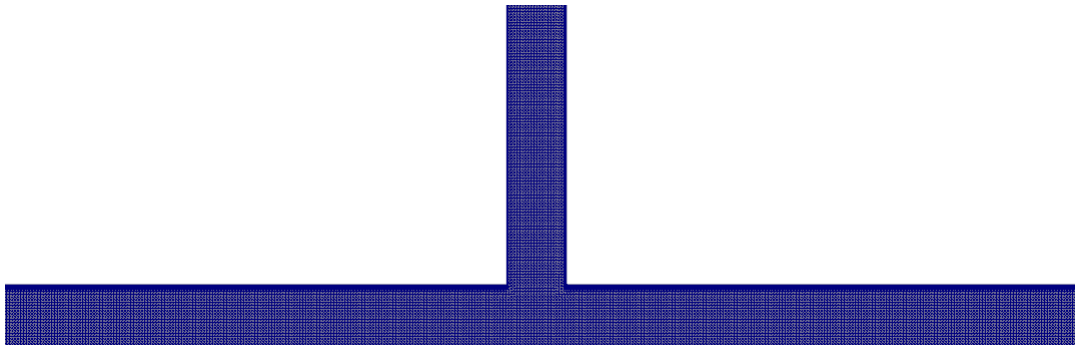


Figure 28: Segment of the simplified mesh for the Screening simulations

### 5.2 Boundary Conditions

In difference to the Base Case, a fully turbulent simulation is investigated for the Screening exercise. The reason for this change is to eliminate a possible influence of the transition prediction on the calculation of  $k$ . Inlet velocities are adjusted to the changed inlet geom-

etry.

Table 13: CFD boundary conditions for Screening

		Inlet 1	Inlet 2	Outlet	Wall
Velocity	$m/s$	0.33	0.33	zeroGradient	0
Pressure	$m^2s^{-2}$	zeroGradient	zeroGradient	1e5	zeroGradient
k	$m^2s^{-2}$	0.0005	0.0005	zeroGradient	0
$\omega$	$s^{-1}$	50	50	zeroGradient	1e-30
$\gamma$	-	1	1	zeroGradient	zeroGradient
$Re_\theta$	-	20	20	zeroGradient	zeroGradient
T	$K$	293	293	zeroGradient	zeroGradient

### 5.3 Design of Simulation Experiments

The investigated factors and levels are listed in Table 14. Levels are chosen according to (Schaefer et al. 2017).

Table 14: Investigated values of the Screening exercise

	Index	Standard Value (0)	Low Value (-1)	High Value (+1)
$\sigma_{K1}$	A	0.85	0.7	1
$\sigma_{K2}$	B	1	0.8	1.2
$\sigma_{\omega1}$	C	0.5	0.3	0.7
$\sigma_{\omega2}$	D	0.856	0.7	1.0
$\beta_1$	E	0.075	0.0598	0.0861
$\beta_2$	F	0.0828	0.0541	0.0975
$\beta^*$	G	0.09	0.0784	0.1024
$a_1$	H	0.31	0.31	0.4

## 5. SCREENING SIMULATIONS

---

A  $2^{8-4}$ , resolution IV, fractional factorial design is created for this task, resulting in 16 simulations. All factor combinations and corresponding response values ( $y$ ) are displayed in Table 15

Table 15: Fractional factorial screening design

	A	B	C	D	E	F	G	H	y
1	-1	-1	-1	-1	-1	-1	-1	-1	-6.731628
2	1	-1	-1	-1	1	1	1	-1	-7.751418
3	-1	1	-1	-1	1	1	-1	1	-7.113599
4	1	1	-1	-1	-1	-1	1	1	-6.325925
5	-1	-1	1	-1	1	-1	1	1	-5.745733
6	1	-1	1	-1	-1	1	-1	1	-5.144416
7	-1	1	1	-1	-1	1	1	-1	-5.398487
8	1	1	1	-1	1	-1	-1	-1	-6.135501
9	-1	-1	-1	1	-1	1	1	1	-6.306334
10	1	-1	-1	1	1	-1	-1	1	-7.145642
11	-1	1	-1	1	1	-1	1	-1	-7.733954
12	1	1	-1	1	-1	1	-1	-1	-6.718458
13	-1	-1	1	1	1	1	-1	-1	-6.151910
14	1	-1	1	1	-1	-1	1	-1	-5.395276
15	-1	1	1	1	-1	-1	-1	1	-5.160671
16	1	1	1	1	1	1	1	1	-5.739720

### 5.3.1 Response

A volume averaged  $k$  value, extracted from the mixing section of the channel, is chosen as the response (Equation 5.1).

$$y = k_{avg} = \frac{1}{V} \sum k_i * v_i \quad (5.1)$$

In order to achieve a normal distributed set of data, a logarithmic transformation was applied. The Boxplot of the transformed response is illustrated in Figure 29.

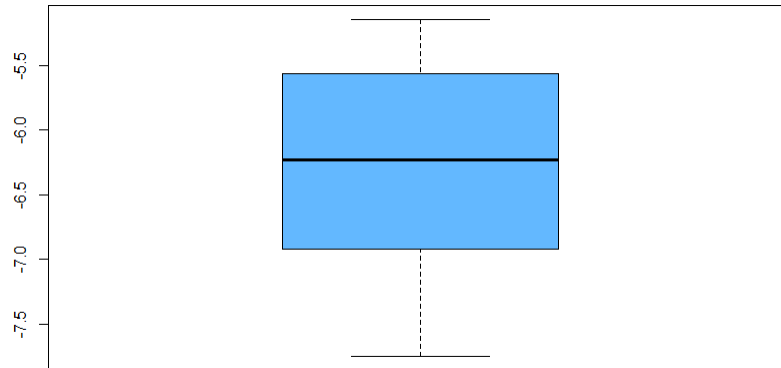


Figure 29: Boxplot of the transformed Response

### 5.4 Evaluation

Inspecting Figure 30 and Figure 31, it appears that Factors C, E and H (which correspond to  $\sigma_{k1}$ ,  $\beta_1$  and  $a_1$ ) have an significant effect on the calculation of  $k$ . As the main effect plot indicates, an increase in  $\sigma_{k1}$  or  $a_1$  results in an increased production of  $k$ , whereas the effect is reversed for  $\beta_1$ .

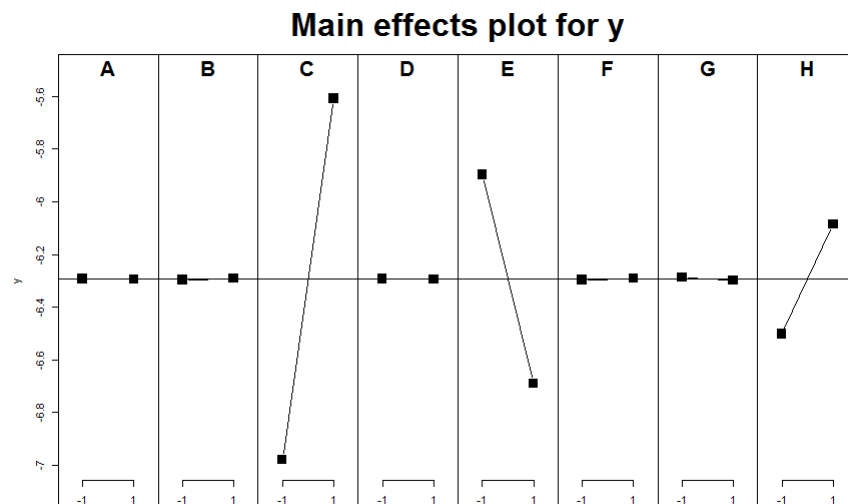


Figure 30: Screening results - Main effects plot

The half normal plot indicates additional significant two factor interactions for  $A : D$ ,  $A : F$  and  $A : B$ . However, considering the confounding pattern of these interactions

## 5. SCREENING SIMULATIONS

---

(Table 16), and the fact that they barely appear as outliers, it is concluded that they can be omitted.

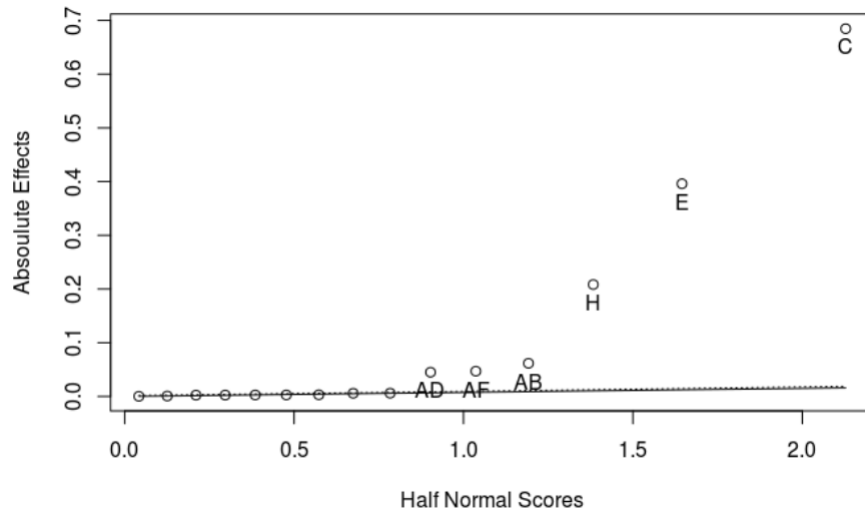


Figure 31: Screening results - Half normal plot

Table 16: Confounding pattern of two factor interactions

$$A:F = B:D = C:H = E:G$$

$$A:B = C:E = D:F = G:H$$

$$A:D = B:F = C:G = E:H$$

## 6 Optimization Simulations

Concluding from the previous screening, an optimization design investigating three factors  $(\sigma_{\omega 1}, \beta_1, a_1)$  is constructed. Aim of this step is to predict an ideal parameter combination that minimizes the simulation error compared to measurement data.

### 6.1 Boundary Conditions

In difference to screening, the optimization results would be unemployable if a simplified geometry was used. Boundary conditions, material properties and mesh therefore correspond to the base case (Section 4.2). All cases are again decomposed in 48 segments and submitted to VSC3.

### 6.2 Design

A CCC (Central Composite Circumscribed) design is applied in order to fit a quadratic model (Section 2.7.3). For three factors, this results in 17 runs, consisting of a full factorial design, center points and axial points. Each factor is therefore investigated on 5 Levels. A graphical representation of this design is illustrated in Figure 32.

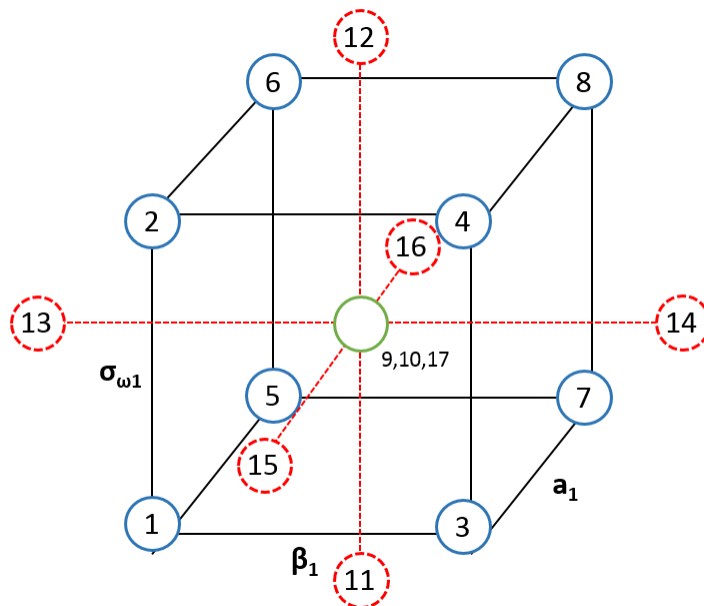


Figure 32: RSM Design

### 6.3 Response

For the comparison of measurements and simulation only the center points of the experimental profiles are evaluated, as to not distort the DoE outcome with invalid measurement points.

The variable in question for comparison is the measured (Section 2.6.4) and simulated turbulent kinetic energy ( $k_{MEA}$  and  $k_{SIM}$  respectively). A total of 213 measurement points, at five different profiles are evaluated. In order to define the response, a single value needs to be specified that incorporates the deviation of simulation and experiment. The calculation of this value is implemented as follows: The root mean square error ( $RMSE_p$ ) for each of the five profiles  $p$  is calculated, where  $n$  is the number of measurement points.

$$RMSE_p = \sqrt{\frac{1}{n} \sum (k_{MEA} - k_{SIM})^2} \quad (6.1)$$

Based on the measurements, a mean value for the turbulent kinetic energy of each profile

is determined

$$MEA_p = \frac{1}{n} \sum (k_{MEA}) \quad (6.2)$$

The relative error for each profile  $Error_p$  arises from

$$Error_p = \frac{RMSE}{MEA_i} \quad (6.3)$$

Finally the mean error, based on all five profiles can be established

$$Error = \frac{1}{5} \sum (Error_p) \quad (6.4)$$

Extraction of the simulation values  $k_{SIM}$  is done using a *ParaView* script. The error calculation and evaluation of the DoE in  $R$  is scripted as well, enabling a flexible and fast post processing.

## 6.4 1<sup>st</sup> Optimization

### 6.4.1 Setup

Proceeding from the standard values given in Section 2.4, the levels for each of the three factors are determined (Table 17). All factor combinations of the 17 run design are listed in Table 18. Note that the center point runs 9, 10 and 17 are identical in their factor settings.

Table 17: Investigated values of the first Optimization Design

	<b>Standard Value (0)</b>	<b>-1.68</b>	<b>-1</b>	<b>+1</b>	<b>+1.68</b>
$\sigma_{\omega 1}$	0.5	0.33	0.4	0.6	0.66
$\beta_1$	0.075	0.05	0.06	0.09	0.1
$a_1$	0.31	0.31	0.34	0.41	0.43

Table 18: First optimization design

	run.order	std.order	sigmaomegal	beta1	a1	y	Block
1	1	1	-1.000000	-1.000000	-1.000000	NA	1
2	2	2	1.000000	-1.000000	-1.000000	NA	1
3	3	3	-1.000000	1.000000	-1.000000	NA	1
4	4	4	1.000000	1.000000	-1.000000	NA	1
5	5	5	-1.000000	-1.000000	1.000000	NA	1
6	6	6	1.000000	-1.000000	1.000000	NA	1
7	7	7	-1.000000	1.000000	1.000000	NA	1
8	8	8	1.000000	1.000000	1.000000	NA	1
9	9	9	0.000000	0.000000	0.000000	NA	1
10	10	10	0.000000	0.000000	0.000000	NA	1
11	1	1	-1.681793	0.000000	0.000000	NA	2
12	2	2	1.681793	0.000000	0.000000	NA	2
13	3	3	0.000000	-1.681793	0.000000	NA	2
14	4	4	0.000000	1.681793	0.000000	NA	2
15	5	5	0.000000	0.000000	-1.681793	NA	2
16	6	6	0.000000	0.000000	1.681793	NA	2
17	7	7	0.000000	0.000000	0.000000	NA	2

#### 6.4.2 Evaluation

A graphical representation of the obtained quadratic model is the contour plot Figure 33. Two observations can be made: First, in order to reduce the error  $\sigma_{\omega_1}$  and  $a_1$  need to be increased, and  $\beta_1$  decreased. This observation is consistent with the results acquired in the previous Screening step (Figure 30). Second, the contour plot reveals that the desired stationary point (= Minimum of Error) is outside the examined region, as indicated by the steep decent of the contour plot.

## 6. OPTIMIZATION SIMULATIONS

---

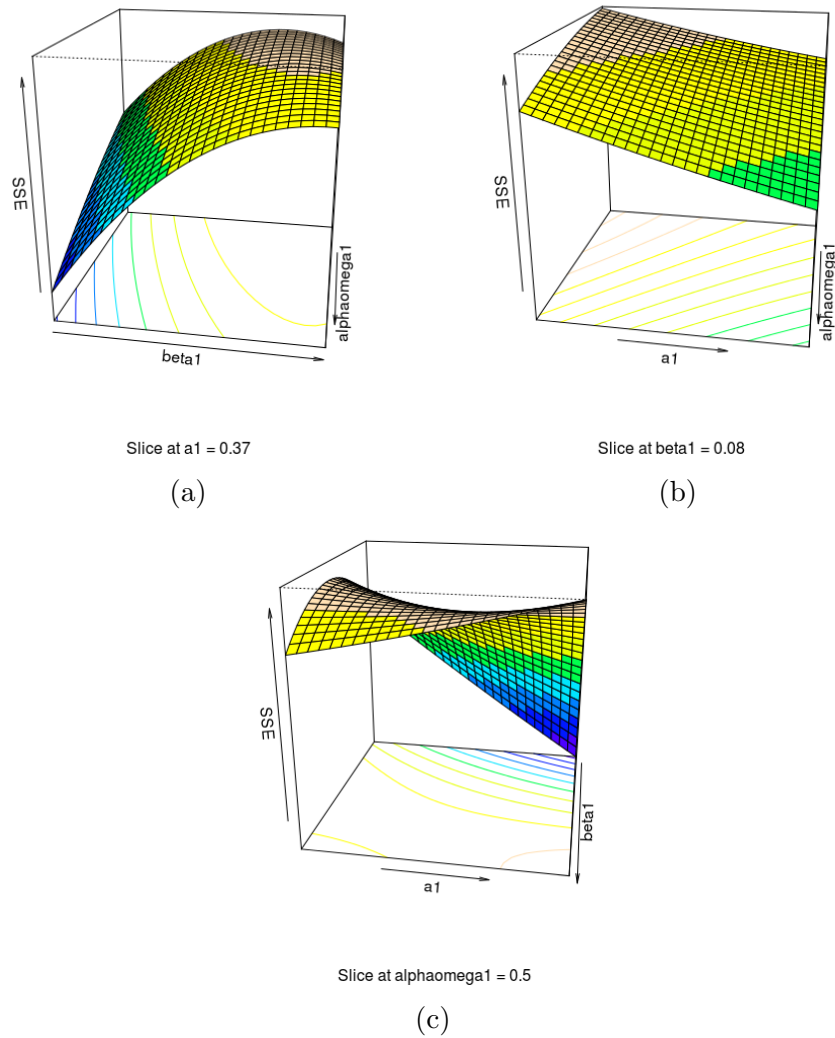


Figure 33: 3D contour plot of the first optimization design, Error on the z-Axis denoted as SSE

Aim of this DoE is to find the best Factor combination possible. Therefore the decision is made to repeat the optimization design with adjusted factor levels, as indicated in Figure 34. Moving the center point to the factor combination that resulted in the least amount of error is expected to yield one out of two possible outcomes: Ideally a minimum of error is detected, satisfying the aim of this DoE. Alternatively, a stability limit is observed i.e. the resulting factor combinations do not produce stable simulations.

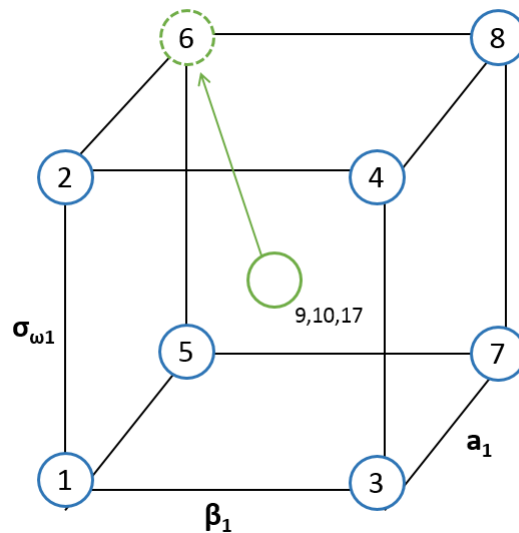


Figure 34: Movement of the center points

## 6.5 2<sup>nd</sup> Optimization

Case setup and boundary conditions are identical to the previous simulations. The moved center point corresponds to the parameter combination that predicted the least amount of error in the first Optimization. High and low levels for  $\sigma_{\omega 1}$  and  $\beta_1$  are determined by applying the same overall range to the new center point, however range for  $a_1$  is reduced compared to the previous DoE. The reason for this reduction are non stable simulations that occurred at  $a_1$  values above 0.58.

Table 19: Investigated values of the first optimization design

	Center Value (0)	-1.68	-1	+1	+1.68
$\sigma_{\omega 1}$	0.65	0.43	0.52	0.78	0.87
$\beta_1$	0.05	0.033	0.04	0.06	0.67
$a_1$	0.44	0.36	0.39	0.48	0.51

Investigated Factor combinations and corresponding Response values are listed in Table 20.

## 6. OPTIMIZATION SIMULATIONS

---

Table 20: 2<sup>nd</sup> Optimization Design

run.order	std.order	sigmaomega1	beta1	a1	y	Block	
1	1	1	0.5200000	0.04000000	0.3960000	0.7328486	1
2	2	2	0.7800000	0.04000000	0.3960000	0.7001272	1
3	3	3	0.5200000	0.06000000	0.3960000	0.8350569	1
4	4	4	0.7800000	0.06000000	0.3960000	0.7759955	1
5	5	5	0.5200000	0.04000000	0.4840000	0.5487783	1
6	6	6	0.7800000	0.04000000	0.4840000	0.7381197	1
7	7	7	0.5200000	0.06000000	0.4840000	0.6428209	1
8	8	8	0.7800000	0.06000000	0.4840000	0.5713454	1
9	9	9	0.6500000	0.05000000	0.4400000	0.6088113	1
10	10	10	0.6500000	0.05000000	0.4400000	0.6088113	1
11	1	1	0.4313669	0.05000000	0.4400000	0.7643486	2
12	2	2	0.8686331	0.05000000	0.4400000	0.6089903	2
13	3	3	0.6500000	0.03318207	0.4400000	0.7305587	2
14	4	4	0.6500000	0.06681793	0.4400000	0.7758746	2
15	5	5	0.6500000	0.05000000	0.3660011	0.8031949	2
16	6	6	0.6500000	0.05000000	0.5139989	0.6752117	2
17	7	7	0.6500000	0.05000000	0.4400000	0.6088113	2

### 6.5.1 Evaluation

In contrast to the Screening exercise, no transformation of the Response data is necessary, since the box plot Figure 35 reveals a satisfying distribution.

## 6. OPTIMIZATION SIMULATIONS

---

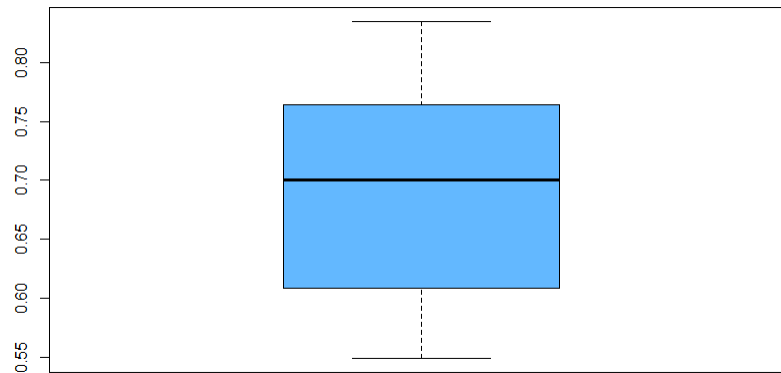


Figure 35: Boxplot of the 2<sup>nd</sup> optimization response

A quadratic regression model is fit to the available data resulting in  $R^2 = 0.82$ . Graphical representation of the residuals  $\varepsilon = y_i - \hat{y}_i$  yields important model fit information. The residual plot Figure 36 illustrates no observable pattern which indicates that the predictions made by the model are in equal quality regardless of the experimental region. This assumption is further backed by the observation that the five runs with the highest residuals (3,4,5,11,16) appear to have no common denominator in terms of their factor combination. Red lines indicate the residual standard error.

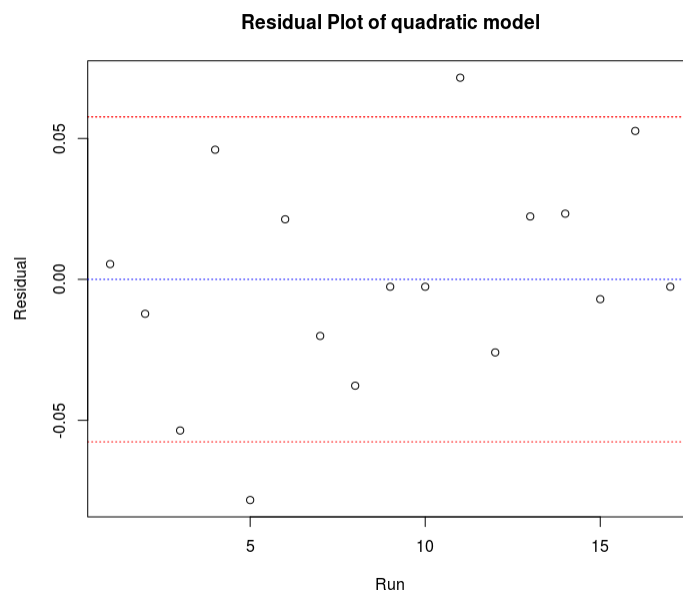


Figure 36: Residual plot of the 2<sup>nd</sup> quadratic model



## 7 Optimization Results

Using the parameter combination found in the previous DoE, a "*Stationary Point*" simulation is performed. Based on the model prediction a reduced error is expected in comparison to the "*Standard*" base case simulation. Boundary conditions and case setup are again analogous to Section 4.2. The following section provides a short qualitative, and more extensive quantitative comparison of the two simulations and the measurements.

### 7.1 Qualitative Comparison

A visual representation of the computed flow field is given in Figure 38. Starting with the velocity magnitude, the only noticeable difference is the decrease of the low velocity zone in the mixing section. Comparing the plots of turbulent kinetic energy, a clear difference is visible as the standard simulation predicts a high  $k$ -value zone which is not computed at the stationary point solution. Interestingly, the change in closure coefficients leads to a decreased  $k$  production in the mixing section. Whether this solution for  $k$  is physical or not is further discussed in Section 7.3.

## 7. OPTIMIZATION RESULTS

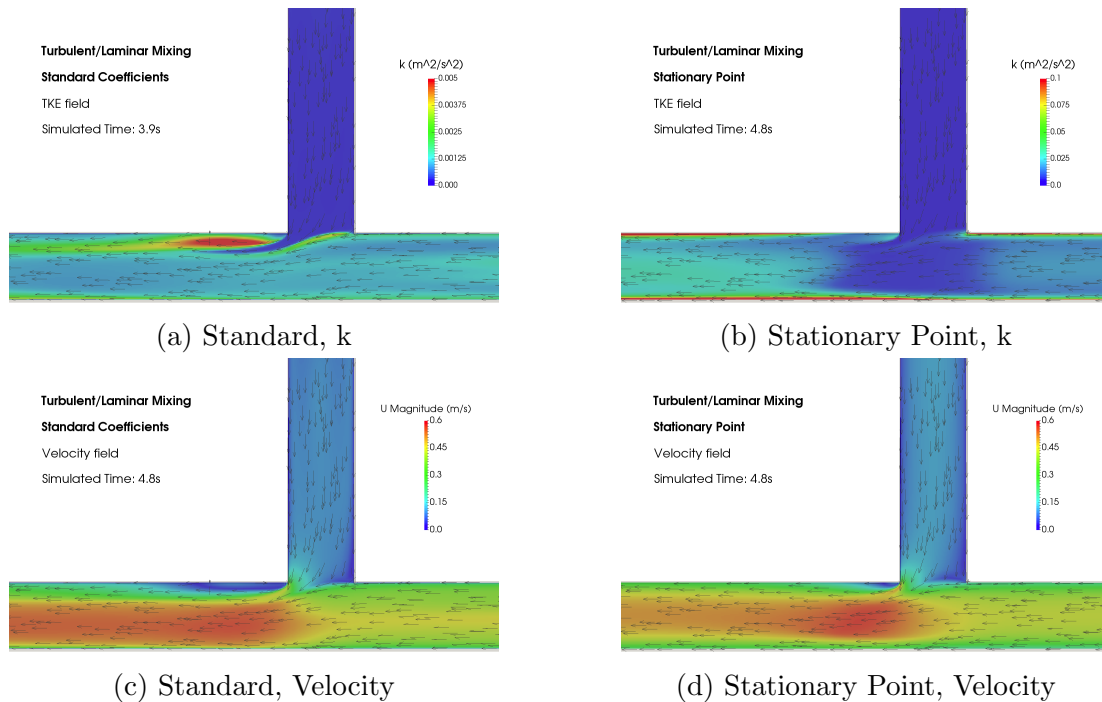


Figure 38: Qualitative comparison of the simulation with standard and adjusted coefficients at the symmetry plane

The solution for intermittency  $\gamma$  of the stationary point simulation is illustrated in Figure 39. Flow in the stratifiers is correctly predicted as laminar due to their small diameter. After the stratifiers the intermittency switches initially to a value of 1, and subsequently decays to  $\sim 0.5$  in the core of the flow field.

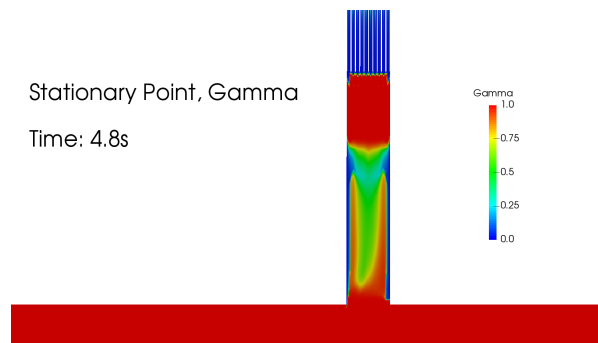


Figure 39: Intermittency values at  $z/h = 0.5$

The closure coefficients inherited from (Abraham, Sparrow, and J. Tong 2008) are

## 7. OPTIMIZATION RESULTS

---

adjusted to calibrate the transition model for internal flow. For the aim of this work the prediction of  $\gamma$  is satisfactory, since the main focus lies on the turbulent part of the flow. However if a precise prediction of transitional channel flow is desired, further optimization is necessary. This could be realized by constructing a DoE based on the transition model closure coefficients (Section 2.5.3), where  $\gamma$  values are selected as response.

### 7.2 Global Error Comparison

Based on the error calculation given in Section 6.3, the influence of closure coefficient adjustment is evaluated.

#### 7.2.1 Turbulent Kinetic Energy, all Profiles

As presented in Figure 40, the adjustment of closure coefficients leads to an error reduction of  $\sim 35\%$  compared to the initial simulation. The graph also displays the calculated error for each DoE simulation (grey).

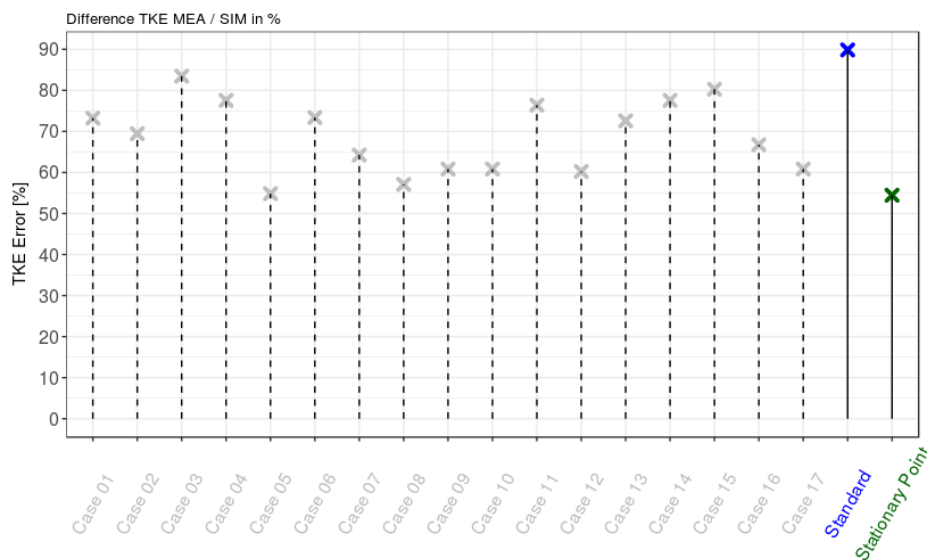


Figure 40: Error comparison of the turbulent kinetic energy error for all optimization simulations

In order to understand the composition of these errors, Figure 41 is inspected. The

## 7. OPTIMIZATION RESULTS

---

leftmost bar represents the mean error of the standard and stationary point simulation respectively. It is apparent that the error for each profile is reduced, except for profile four. This observation backs the assumption that the transitional turbulence model correctly distinguishes between laminar and turbulent flow, since only closure coefficients of the turbulence model part have been changed. As described in Section 4.3, the high error in profile four is due to small velocity fluctuations in the experiment, which lead to non-zero experimental k-values compared to the simulation. Therefore the laminar profile contributes significantly to the resulting mean error.

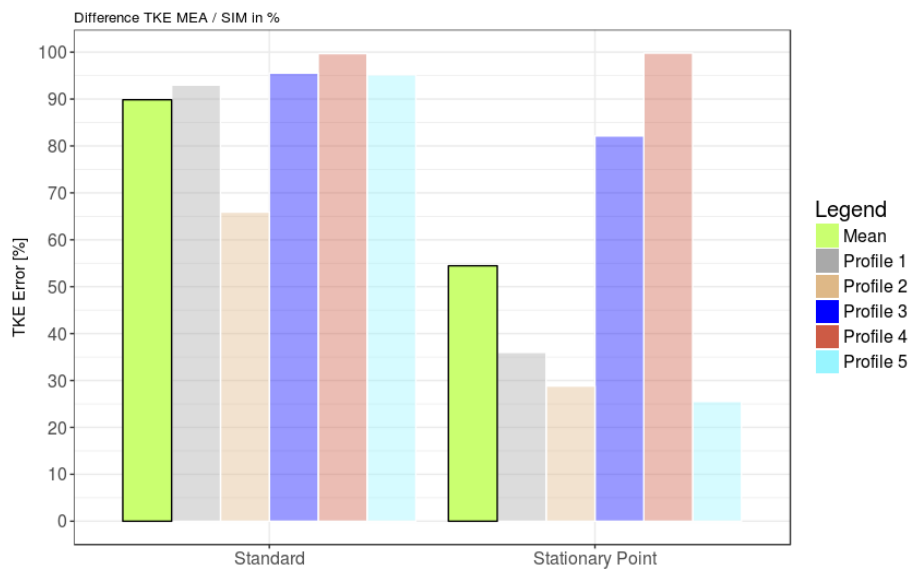


Figure 41: Error composition of the turbulent kinetic energy error with the standard (left) and adjusted (right) coefficients

### 7.2.2 Turbulent Kinetic Energy, only turbulent sections

Due to the laminar profile being unaffected by the parameter changes, the error comparison is repeated while omitting the laminar profile. The error reduction considering only turbulent parts of the flow is  $\sim 45\%$ . Composition of the error (Figure 43) now exhibits a reduction for all profiles, where the biggest improvement is noticeable in Profile 5.

## 7. OPTIMIZATION RESULTS

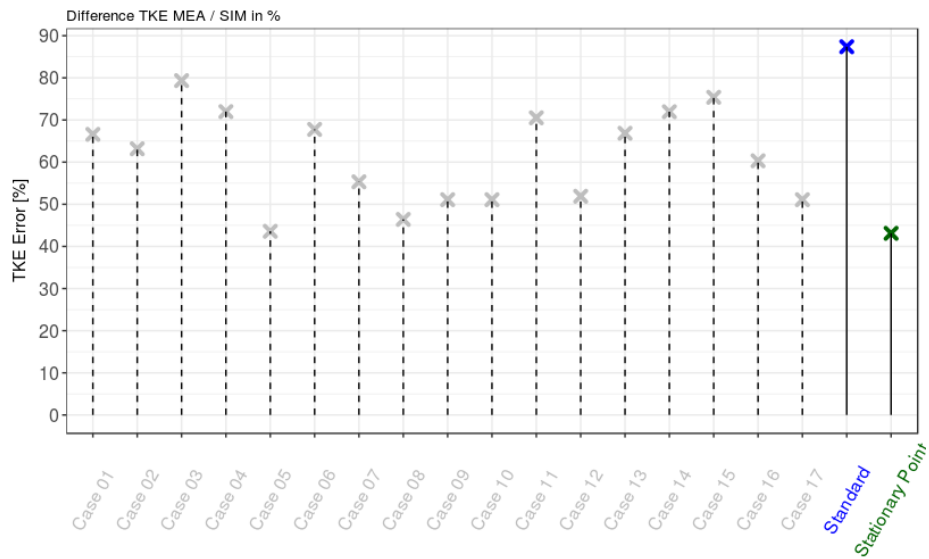


Figure 42: Error comparison of the turbulent kinetic energy error for all optimization simulations, without the laminar profile

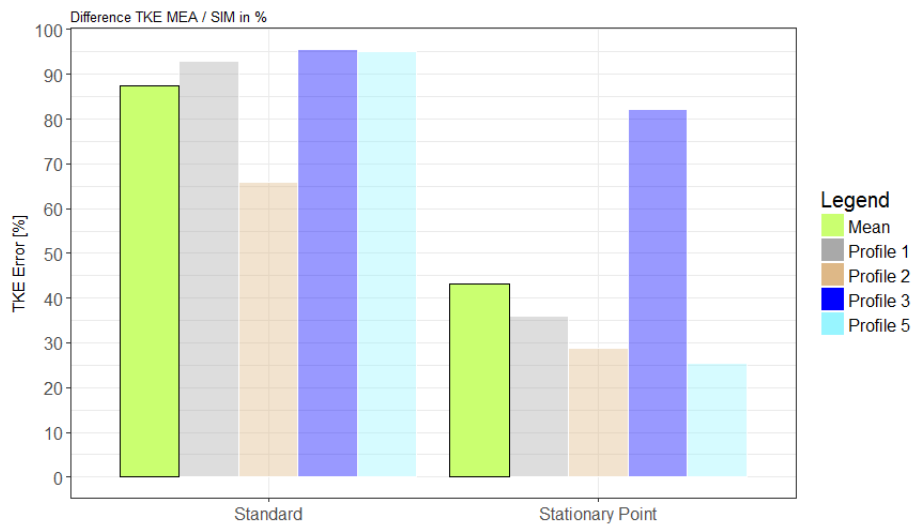


Figure 43: Error composition of the turbulent kinetic energy error with the standard (left) and adjusted (right) coefficients, without the laminar profile

### 7.2.3 Velocity

While the initial comparison of experimental and numerical results presented a discrepancy in turbulent kinetic energy values, a good agreement in velocity data was observed. Velocity

## 7. OPTIMIZATION RESULTS

prediction therefore should not be influenced by the DoE results. As Figure 44 indicates the mean error, based on the average velocity magnitude, of the base case simulation is 14%, with the stationary point simulation slightly below at 13%.

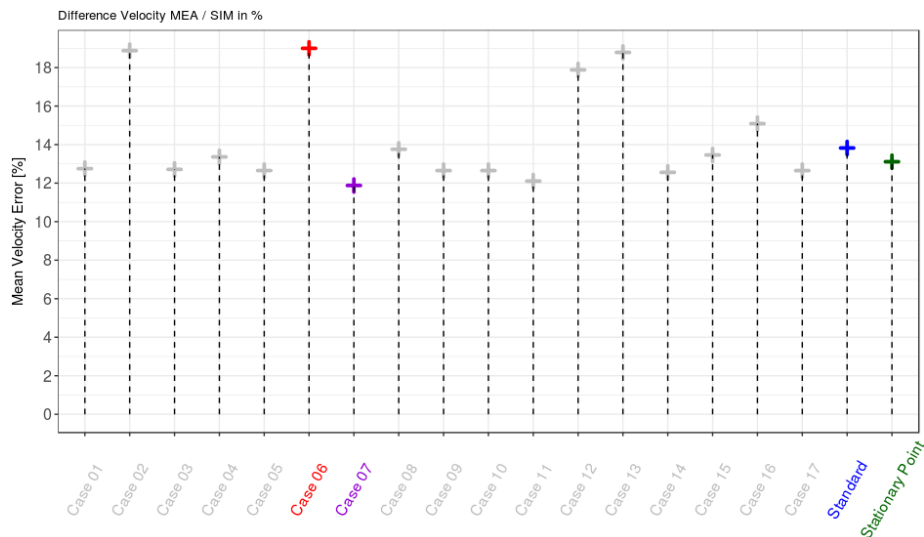


Figure 44: Error comparison of the velocity error for all optimization simulations.

Composition of the velocity error is presented in Figure 45, again the laminar profile exerts the largest amount of error.

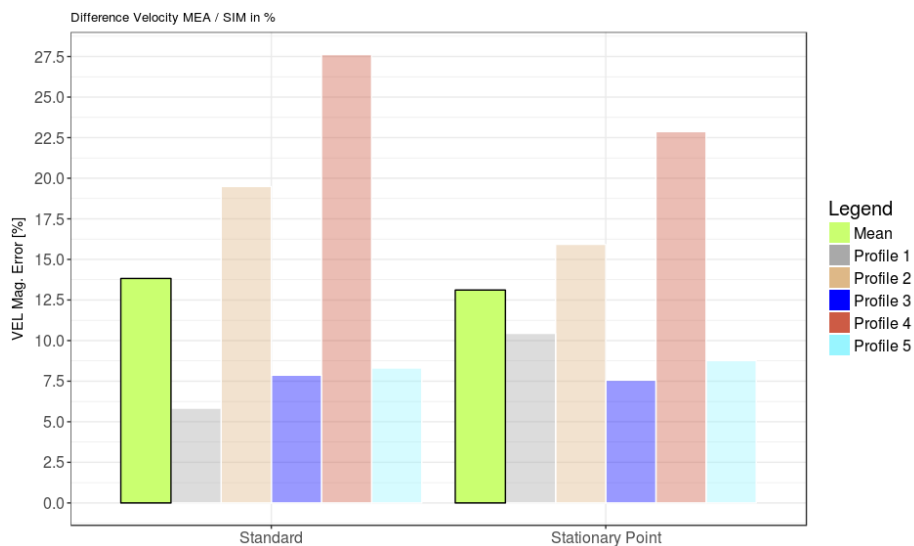


Figure 45: Error composition of the velocity error with the standard (left) and adjusted (right) coefficients

## 7.3 Profile Error Comparison

### 7.3.1 Turbulent kinetic energy

As the composition graphs in the previous section showed, the closure coefficient adjustment influenced the different profiles in various magnitudes. A complete comparison is given in Appendix E - I. All Profiles show a distinct increase in  $k$  near the channel walls for both simulations. The laminar section of the flow is unaffected by the parameter change, therefore both numerical profiles are identical.

Starting with the fully developed turbulent profiles 1 & 5 (Figure 46), a significant difference in magnitude can be observed between the two numerical solutions. Also noticeable is the slight convex curvature of the stationary point profile, which is not observed at the measurements.

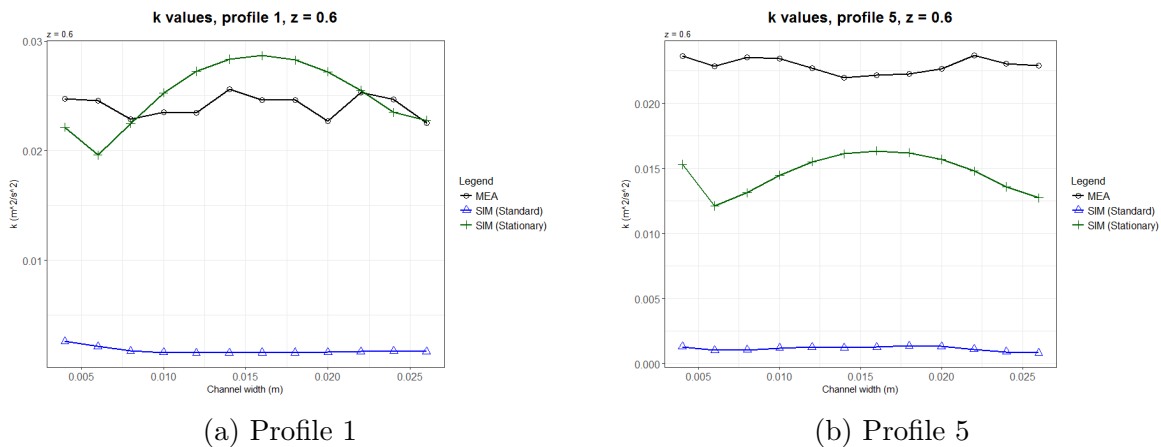


Figure 46: Effect of the parameter change on the turbulent kinetic energy, profiles 1 and 5 at  $z/h = 0.6$

At this point it should be acknowledged that the linear nature of the blue, standard simulation profile is misleading due to the scaling of the graph. Plotting the  $k$  values of Profile 5 without measurement or stationary point data (Figure 47) reveals the non-linearity.

7. OPTIMIZATION RESULTS

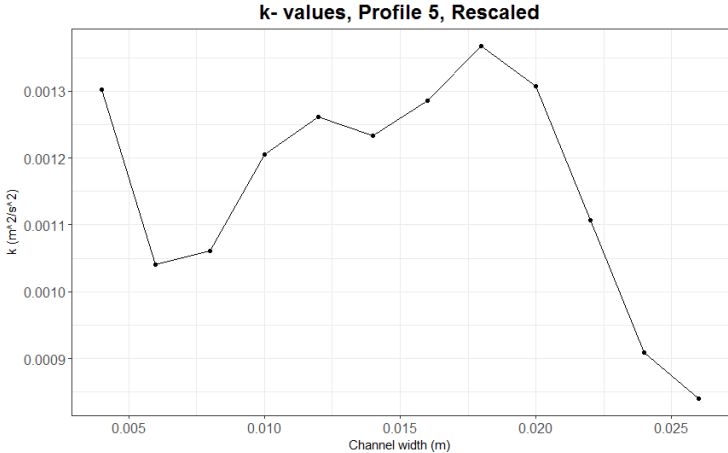


Figure 47: Simulation profile 5 with different scaling at  $z/h = 0.6$

In the mixing section, the simulation underestimates the  $k$  values in magnitude. However, the descent of the measured profile is approximately captured, in contrast to the simulation with standard coefficients where an increase is predicted (Corresponding to the high turbulence section in Figure 38). Although  $k$  is still under predicted, the change in closure coefficients yields an overall improved prediction at this part of the flow.

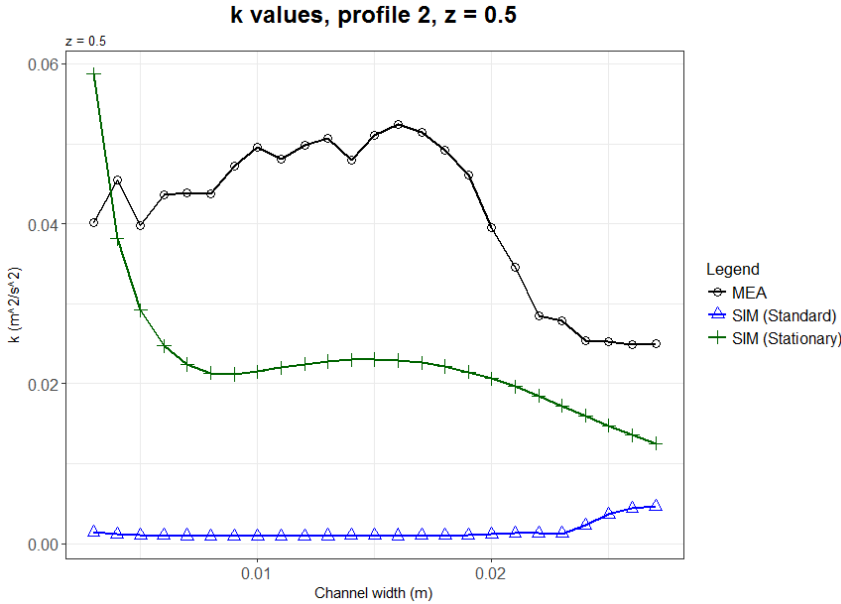


Figure 48: Effect of the parameter change on the turbulent kinetic energy, profile 2 at  $z/h = 0.5$

## 7. OPTIMIZATION RESULTS

Profile 3 exhibits the least amount of change in comparison with the other turbulent profiles. The characteristic increase in  $k$  near  $x = 0.025\text{ m}$  is predicted in both simulations.

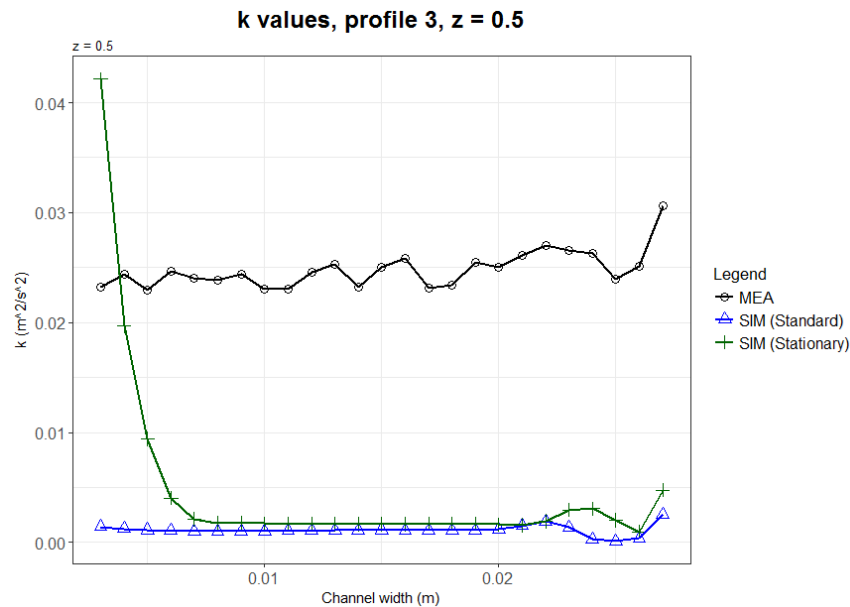


Figure 49: Effect of the parameter change on the turbulent kinetic energy, profile 3 at  $z/h = 0.6$

Based on the available measurement data it can be concluded that the low  $k$  zone predicted in Figure 38 is not physical. LDV data displays no decrease in turbulent kinetic energy in the mixing section, on the contrary  $k$  values at profile 2 exceed the values at profile 1 & 5 significantly. This behavior is not represented by either simulation since the  $k$  values in the standard simulation remain approximately the same throughout the turbulent flow. It is also evident that the adjustment of closure coefficients influences fully developed turbulent flows (Profile 1 & 5) significantly more than the mixing section (Profiles 2 & 3).

### 7.3.2 Velocity

In contrast to the turbulent kinetic energy profiles, the velocity components are predicted broadly similar in both simulations. The most notable difference in the velocity profiles of the base case and stationary point simulation is observed in profile 2 (Figure 50), where the step descent of the main velocity component near  $x = 0.02\text{ m}$  is not predicted in

## 7. OPTIMIZATION RESULTS

---

the stationary point simulation. Comparison with LDV data suggests that the new profile is closer to the experimental result in shape, though the velocity magnitude is still underpredicted.

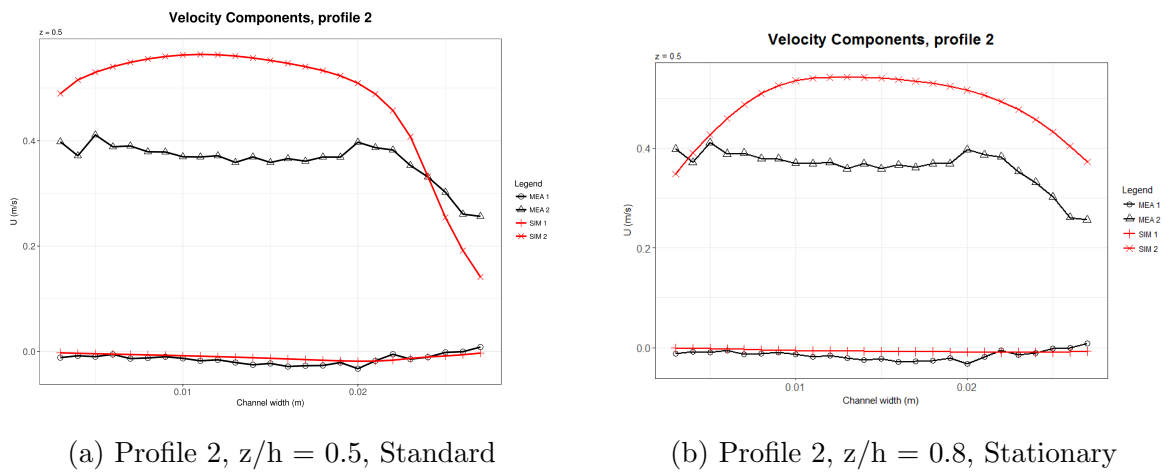


Figure 50: Effect of the parameter change on the velocity components, profiles 2 at  $z/h = 0.5$

## 8 Summary and Outlook

### 8.1 Summary

Primary motivation of this work was a discrepancy in experimental (LDV) and numerical (CFD) turbulent kinetic energy  $k$  values. Based on LDV measurements a statistical approach was applied to calibrate the closure coefficients of the turbulence model.

Evaluation of the measurements revealed that data acquisition near the channel walls is challenging. Near the side walls, the thin glue layer blocks the laser light from entering the channel. Measurements near top and bottom wall are difficult due to reflections and the shape of the measurement volume. Nonetheless, due to the high resolution of the profiles, enough quality data points were acquired in the bulk of the flow field. If the flow structures near the channel walls are of great interest, the experimental setup needs to be adapted.

In order to simulate laminar and turbulent flow in the same computational domain, a RANS based transitional turbulence model was used. Part of this work was to investigate the models ability to correctly predict laminar flow. A calibration for internal flow was inherited from Abraham, Sparrow, and J. Tong (2008), the results of the intermittency  $\gamma$  are adequate, therefore no further effort was made in the calibration of the transition prediction. However, the numerical results reveal that there is room for optimization if the exact transition onset is of interest.

The initial comparison of measurement and numerical data revealed a satisfying fit of the velocity components. The main contributor to the mean error of 14% is the laminar profile 4 where a secondary velocity component is present in the experiments compared to the simulation, therefore illustrating the difficulty of producing fully laminar channel flow. In contrast to velocity, the turbulent kinetic energy is significantly underpredicted in the numerical solution, where the mean error is  $\sim 90\%$ . In order to reduce this error, the turbulence model closure coefficients are adjusted using Design of Experiments.

In the first Screening step of the DoE, a fractional factorial design was applied on a simplified mesh to reduce computational effort and eliminate unnecessary closure coefficients

from future investigations. It was revealed that for the present geometry, three out of eight coefficients significantly influence the prediction of  $k$ . In a first optimization step, the three remaining closure coefficients were further investigated using a CCC design. Evaluation revealed that the desired minimum of error point was clearly outside the experimental region. A second optimization was performed with adjusted factor ranges that resulted in the prediction of a stationary point at  $\sigma_{\omega 1} = 0.66$ ,  $\beta_1 = 0.05$  and  $a_1 = 0.47$ . For one factor,  $a_1$ , a stability limit was found at values  $a_1 \geq 0.58$  where no stable solution could be achieved. The obtained quadratic regression model displayed an adequate fit for the present task. Model prediction could be enhanced e.g by performing a subsequent DoE with smaller factor ranges in the vicinity of the stationary point. It is however questionable if this improvement justifies the computational effort, since due to the shape of the contour plot no significant value changes are expected.

Comparison of the numerical solution with adjusted closure coefficients, standard coefficients and measurement data revealed an error reduction of  $\sim 45\%$  in the prediction of  $k$ . Evaluation revealed that the laminar flow was not affected by the parameter changes. In the fully turbulent flow, a significant improvement in magnitude of  $k$  was achieved. It is evident that the mixing section profiles are influenced differently, as  $k$  is still underpredicted in profiles 2 and 3.

### 8.2 Future Work

The main intention of this work was to reduce the underprediction of  $k$  in the simulation, which was accomplished. However the present results indicate that there is still room for further research, primarily the elimination of the remaining error. Evidently, this error does not solely consist of the model error  $\varepsilon_{model}$ , but also the numerical error  $\varepsilon_{num}$ , measurement error  $\varepsilon_{mea}$  and boundary condition error  $\varepsilon_{b.c.}$ . It is therefore not feasible that sole adjustment of the closure coefficients will lead to a perfect match of simulation and experiments. Since the mixing section profiles constitute the largest part of remaining error, they should be the key point of investigation if further closure coefficient adjustments are desired.

## 8. SUMMARY AND OUTLOOK

---

Results also indicated that the prediction of  $\gamma$  in the laminar part of the simulation could be improved. This may be achievable by constructing another DoE based on the transition model closure coefficients with the intermittency as response. Alternatively a new set of empirical correlations, specifically designed for internal flow, could be implemented in the framework of the  $\gamma - Re_\theta$  model.

A reasonable next step originating from this work is the validation of the obtained closure coefficients with multiphase or multispecie experiments, to determine whether the mixing prediction for internal laminar and turbulent flow is improved. If an enhancement can be observed, the subsequent steps should include validation for different internal flows and materials. Based on the outcome of validation experiments, a decision can be made whether further efforts to reduce the remaining error are reasonable.

## Appendix A Empirical Correlations

Three sets of empirical correlations are part of the  $\gamma - Re_\theta$  model (Robin B. Langtry and Florian R. Menter 2009):

$$F_{length} = \begin{cases} 398.189 * 10^{-1} + (-119.270 * 10^{-4})\tilde{Re}_{\theta t} + (-132.567 * 10^{-6})\tilde{Re}_{\theta t}^2 & \tilde{Re}_{\theta t} < 400 \\ 263.404 + (-123.939 * 10^{-2})\tilde{Re}_{\theta t} + (194.548 * 10^{-5})\tilde{Re}_{\theta t}^2 + \\ (-101.659 * 10^{-8})\tilde{Re}_{\theta t}^3 & 400 \leq \tilde{Re}_{\theta t} \leq 596 \\ 0.5 - (\tilde{Re}_{\theta t} - 596.0) * 3.0 * 10^{-4} & 596 \leq \tilde{Re}_{\theta t} \leq 1200 \\ 0.3188 & 1200 \leq \tilde{Re}_{\theta t} \end{cases} \quad (\text{A.1})$$

$$Re_{\theta c} = \begin{cases} \tilde{Re}_{\theta t} - (396.035 * 10^{-2} + (-120.656 * 10^{-4})\tilde{Re}_{\theta t} + (868.230 * 10^{-6})\tilde{Re}_{\theta t}^2) & \tilde{Re}_{\theta t} \leq 1870 \\ (-696.506 * 10^{-9})\tilde{Re}_{\theta t}^3 + (174.105 * 10^{-12})\tilde{Re}_{\theta t}^4 & \\ \tilde{Re}_{\theta t} - (593.11 + (\tilde{Re}_{\theta t} - 1870.0) * 0.482) & \tilde{Re}_{\theta t} > 1870 \end{cases} \quad (\text{A.2})$$

$$Re_{\theta t} = \begin{cases} \left[ 1173.51 - 589.428Tu + \frac{0.2196}{Tu^2} \right] F(\lambda_\theta), & Tu \leq 1.3 \\ 331.50[Tu - 0.5658]^{-0.671} F(\lambda_\theta), & Tu > 1.3 \end{cases} \quad (\text{A.3})$$

$$F(\lambda_\theta) = 1 - [-12.986\lambda_\theta - 123.66\lambda_\theta^2 - 405.689\lambda_\theta^3]e^{-[\frac{Tu}{1.5}]^{1.5}}, \quad \lambda_\theta \leq 0$$

$$F(\lambda_\theta) = 1 + 0.275[1 - e^{[-35.0\lambda_\theta]}]e^{[\frac{-Tu}{0.5}]}, \quad \lambda_\theta > 0$$

## Appendix B Measurement Results - Cross section

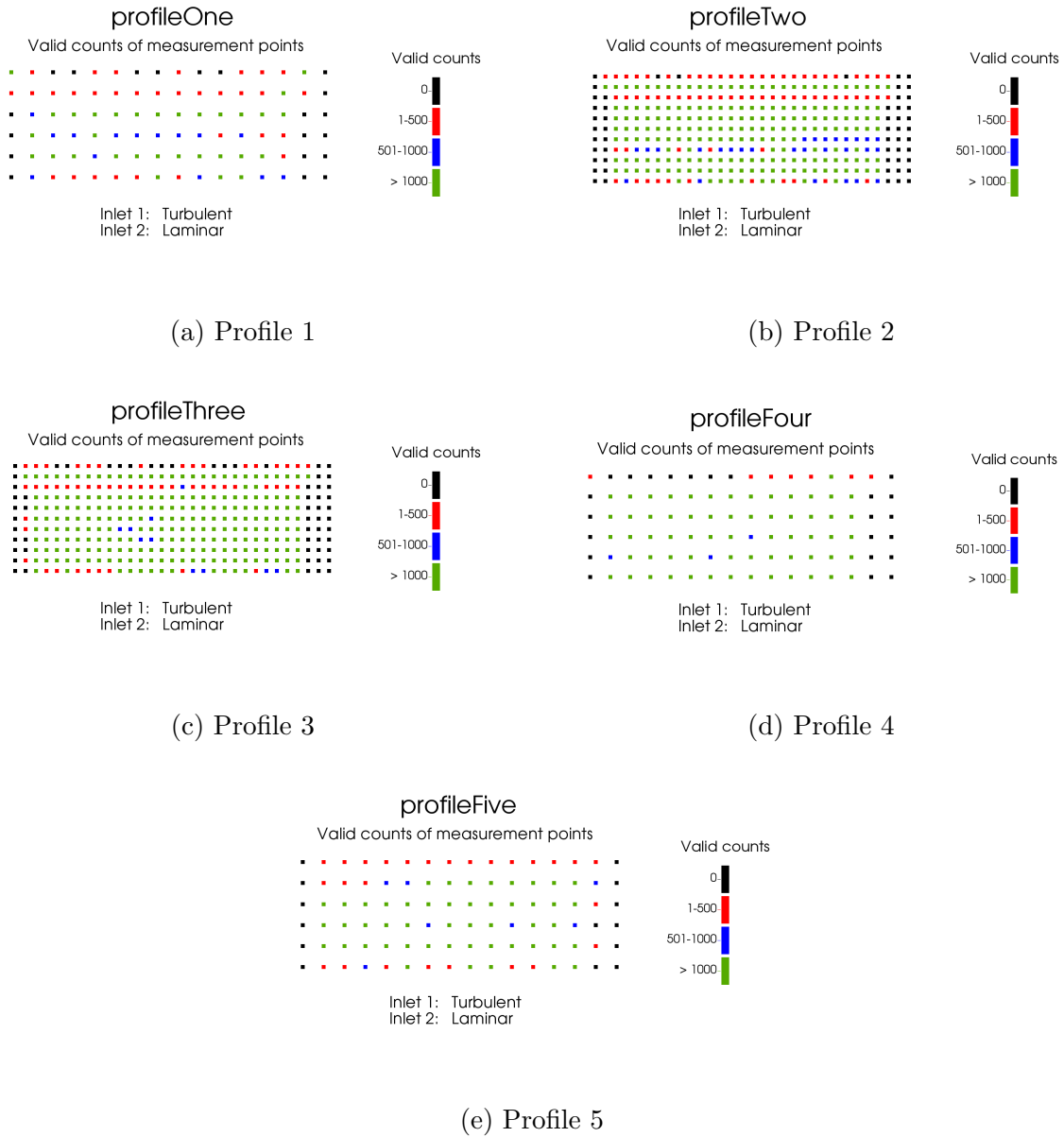
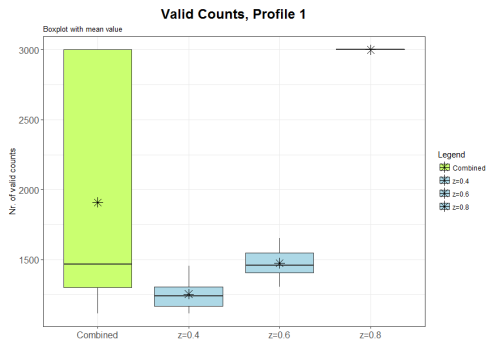
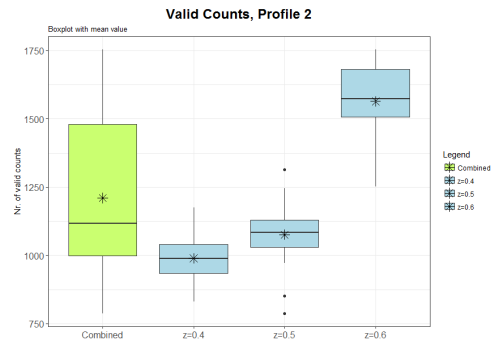


Figure 51: Valid counts for all measurement points

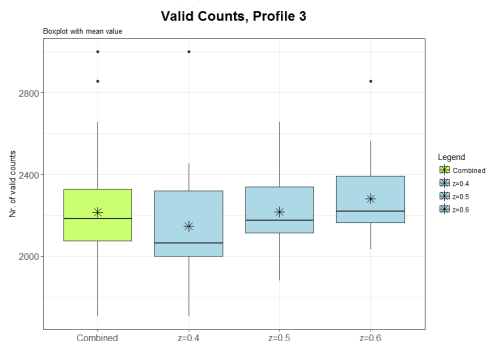
## Appendix C Measurement Results - Box plot



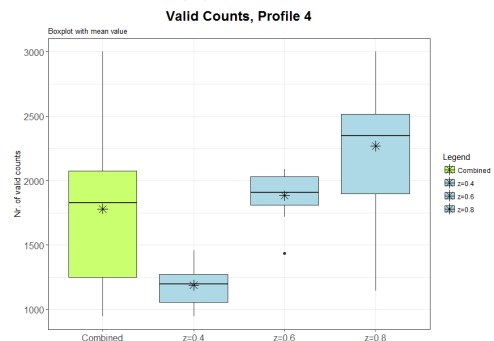
(a) Profile 1



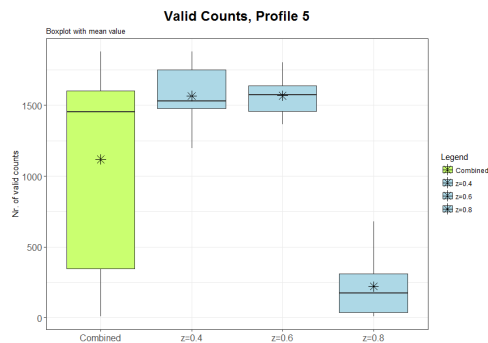
(b) Profile 2



(c) Profile 3



(d) Profile 4



(e) Profile 5

Figure 52: Valid counts for all measurement points

## Appendix D OpenFOAM solver settings

### D.1 turbulenceProperties

```
/*-----*- C++ -*-----*\
| ===== |
| \\ / F i e l d | OpenFOAM: The Open Source CFD Toolbox |
| \\ / O p e r a t i o n | Version: 4.0 |
| \\ / A n d | Web: www.OpenFOAM.org |
| \\ / M a n i p u l a t i o n |
\*-----*/
FoamFile
{
    version      2.0;
    format       ascii;
    class        dictionary;
    location     "constant";
    object       RASProperties;
}
// ***** //

simulationType RAS;

RAS
{
    RASModel      kOmegaSSTTransition;

    turbulence    on;

    printCoeffs  on;

kOmegaSSTTransitionCoeffs
{
// -kOmegaSST
alphaK1         0.85;
    alphaK2      1;
    alphaOmega1  0.5;
    alphaOmega2  0.856;
    Prt          1;
    gamma1       0.555556;
    gamma2       0.44;
}
```

## D. OPENFOAM SOLVER SETTINGS

---

```
beta1      0.075;
beta2      0.0828;
betaStar   0.09;
a1         0.31;
b1         1;
c1         10;
F3         false;

// -Transition
ca1        2;
ca2        0.06;
ce1        1;
ce2        70; //ABRAHAM2009
sigmaf     1;
cTheta    0.015; //ABRAHAM2009
sigmaTheta 2;
s1         2;
}
}
.
.
.
```

### D.2 fvSolution

```
solvers
{
    "rho.*"
    {
        solver      diagonal;
    }

    p
    {
        solver      GAMG;
        tolerance   1e-7;
        relTol      0.05;
        smoother    GaussSeidel;
        nPreSweeps  0;
        nPostSweeps 2;
        nFinestSweeps 2;
        cacheAgglomeration on;
    }
}
```

## D. OPENFOAM SOLVER SETTINGS

---

```
    nCellsInCoarsestLevel 10;
    agglomerator    faceAreaPair;
    mergeLevels    1;
}

pFinal
{
    $p;
    tolerance    1e-6;
    relTol    0.0;
}

p_rgh
{
    solver    GAMG;
    tolerance    1e-7;
    relTol    0.05;
    smoother    GaussSeidel;
    nPreSweeps    0;
    nPostSweeps    2;
    nFinestSweeps    2;
    cacheAgglomeration on;
    nCellsInCoarsestLevel 10;
    agglomerator    faceAreaPair;
    mergeLevels    1;
}

p_rghFinal
{
    $p_rgh;
    tolerance    1e-6;
    relTol    0.0;
}

"(U|h|k|omega|Ret|gamma)"
{
    solver    PBiCG;
    preconditioner    DILU;
    tolerance    1e-6;
    relTol    0.1;
    //nSweeps    1;
}
```

## D. OPENFOAM SOLVER SETTINGS

---

```
"(U|h|k|omega|Ret|gamma)Final"
{
    $U;
    relTol      0.1;
}

Yi
{
    $U;
    relTol      0.1;
}
}
relaxationFactors
{
    fields
    {
        h      0.9;
    }
}

PIMPLE
{
    momentumPredictor no;
    nOuterCorrectors 1;
    nCorrectors      1;
    nNonOrthogonalCorrectors 0;
}
```

### D.3 fvSchemes

```
ddtSchemes
{
    default      Euler;
}

gradSchemes
{
    default      Gauss linear;
}

divSchemes
{
```

## D. OPENFOAM SOLVER SETTINGS

---

```
    default          none;

    div(phi,U)       Gauss limitedLinearV 1;
    div(phi,Yi_h)    Gauss limitedLinear 1;
    div(phi,K)       Gauss limitedLinear 1;
    div(phi,k)       Gauss limitedLinear 1;
    div(phiid,p)     Gauss limitedLinear 1;
    div(phi,epsilon) Gauss limitedLinear 1;
    div(phi,omega)   Gauss limitedLinear 1;
    div(phi,Ret)     Gauss limitedLinear 1;
    div(phi,gamma)   Gauss limitedLinear 1;
    div((muEff*dev2(T(grad(U)))) Gauss linear;
    div(((rho*nuEff)*dev2(T(grad(U)))) Gauss linear;
}

laplacianSchemes
{
    default          Gauss linear orthogonal;
}

interpolationSchemes
{
    default          linear;
}

snGradSchemes
{
    default          orthogonal;
}

fluxRequired
{
    default          no;
    p_rgh;
}

wallDist
{
    method meshWave;
}
```

## Appendix E Profile 1

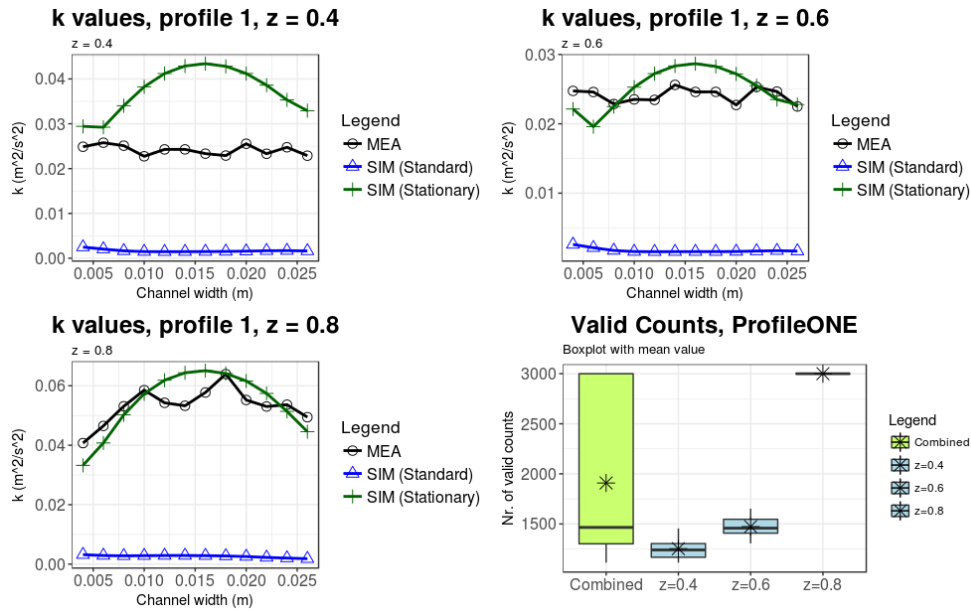


Figure 53: Turbulent kinetic energy comparison (Profile 1)

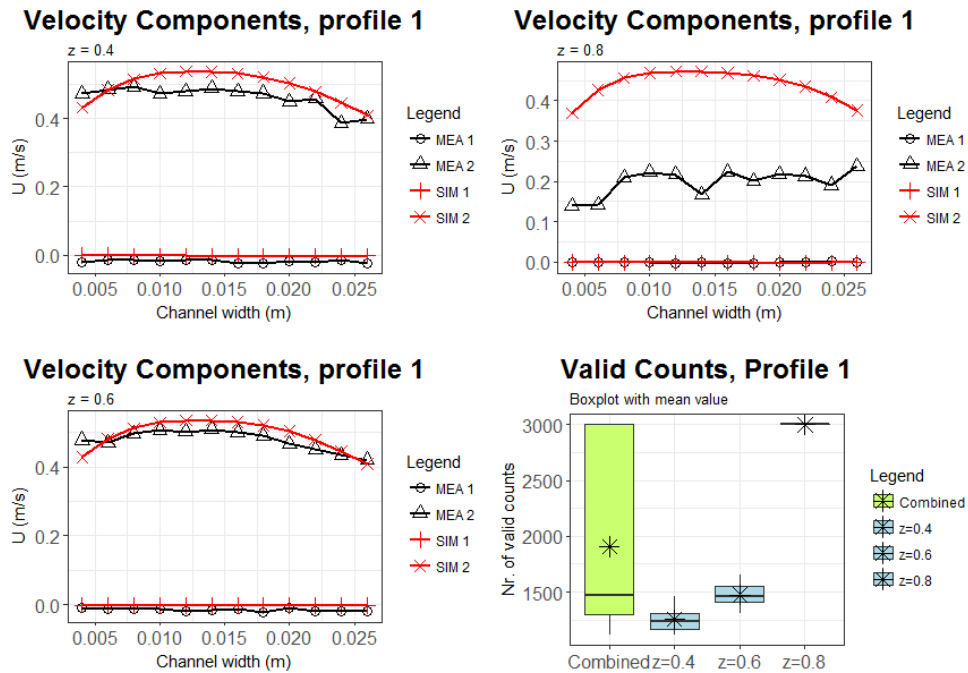


Figure 54: Standard coefficients velocity components comparison (Profile 1)

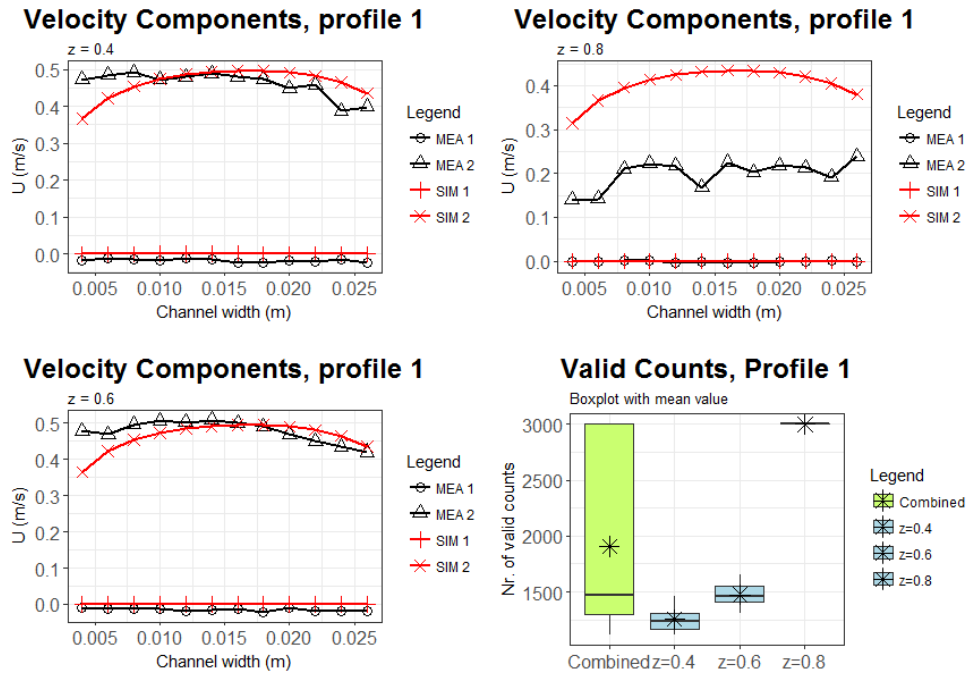


Figure 55: Adjusted coefficients velocity components comparison (Profile 1)

## Appendix F Profile 2

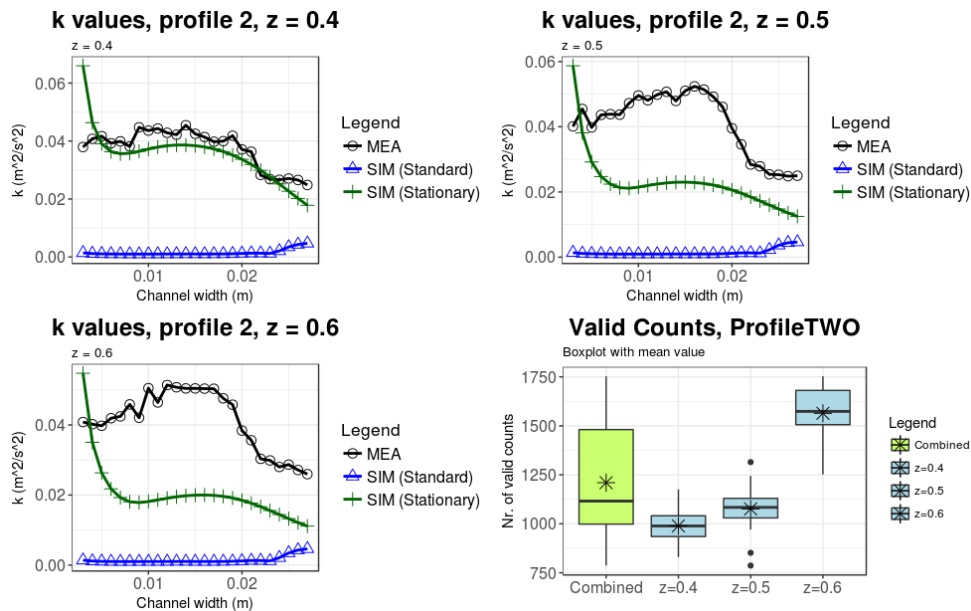


Figure 56: Turbulent kinetic energy comparison (Profile 2)

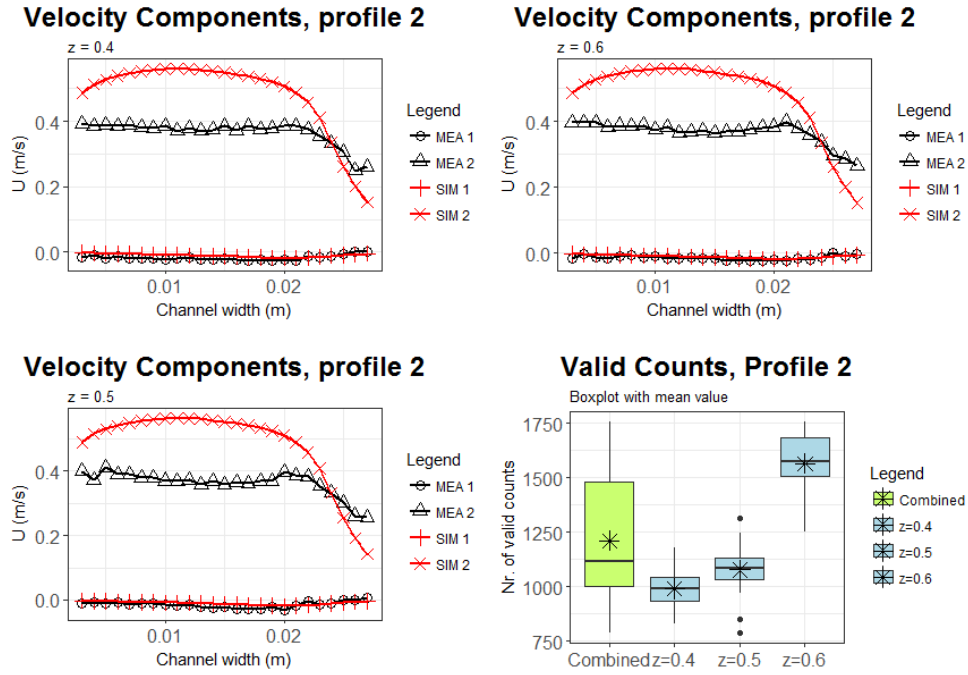


Figure 57: Standard coefficients velocity components comparison (Profile 2)

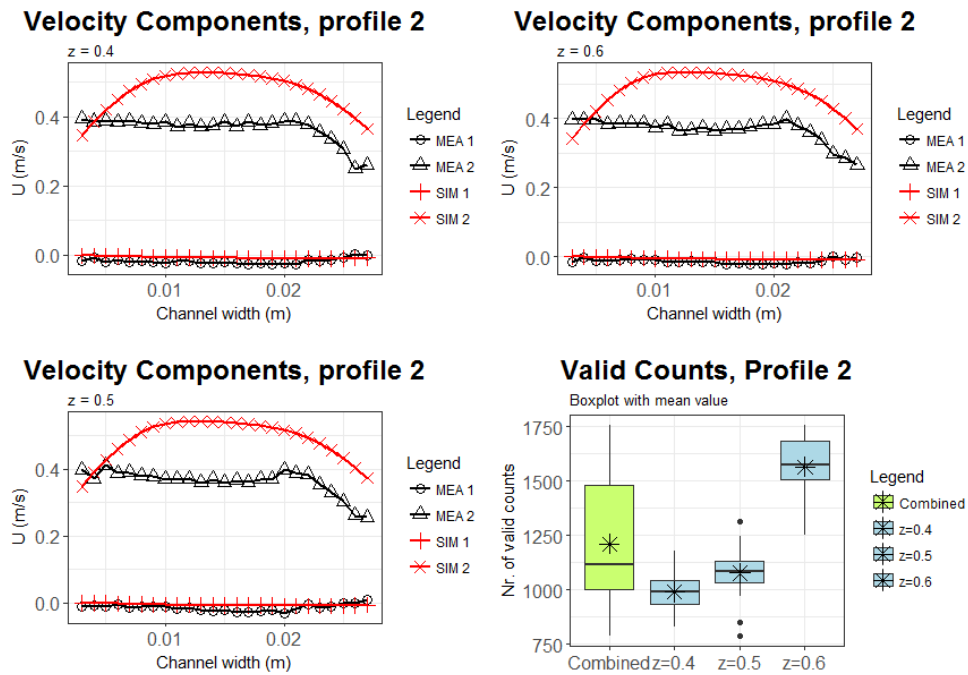


Figure 58: Adjusted coefficients velocity components comparison (Profile 2)

## Appendix G Profile 3

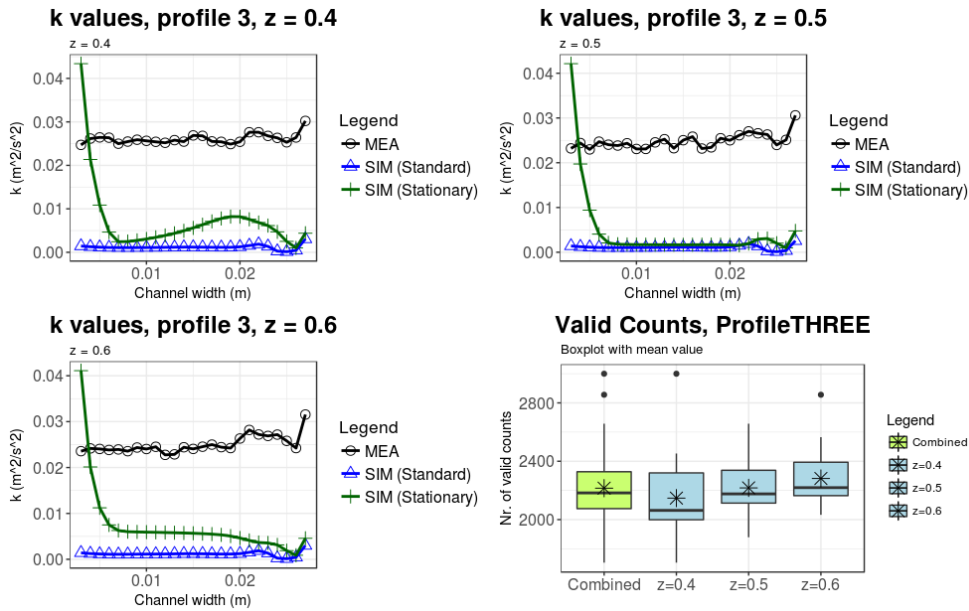


Figure 59: Turbulent kinetic energy comparison (Profile 3)

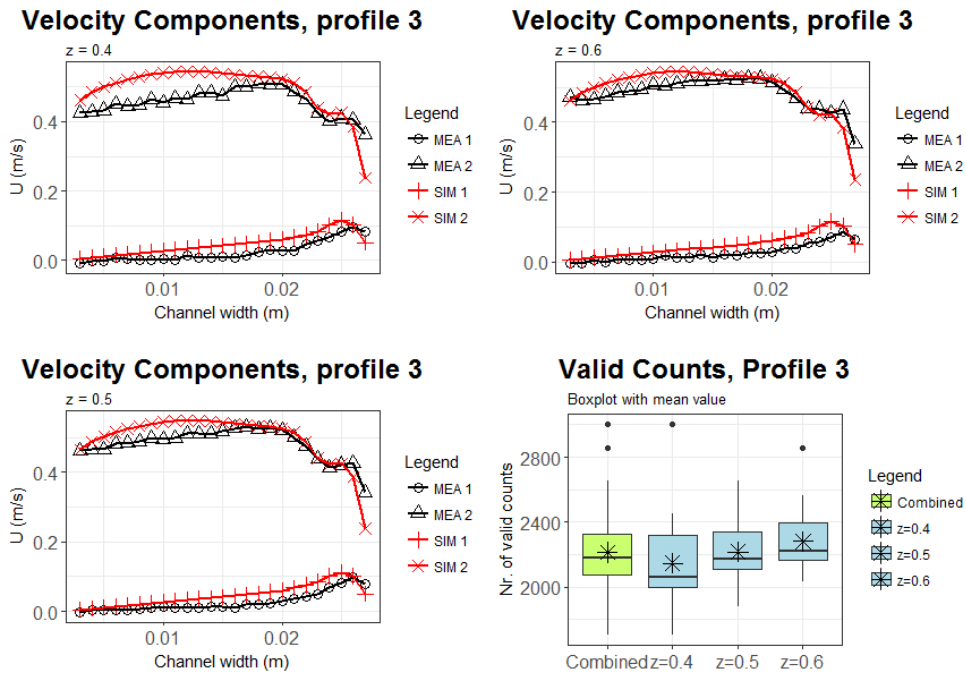


Figure 60: Standard coefficients velocity components comparison (Profile 3)

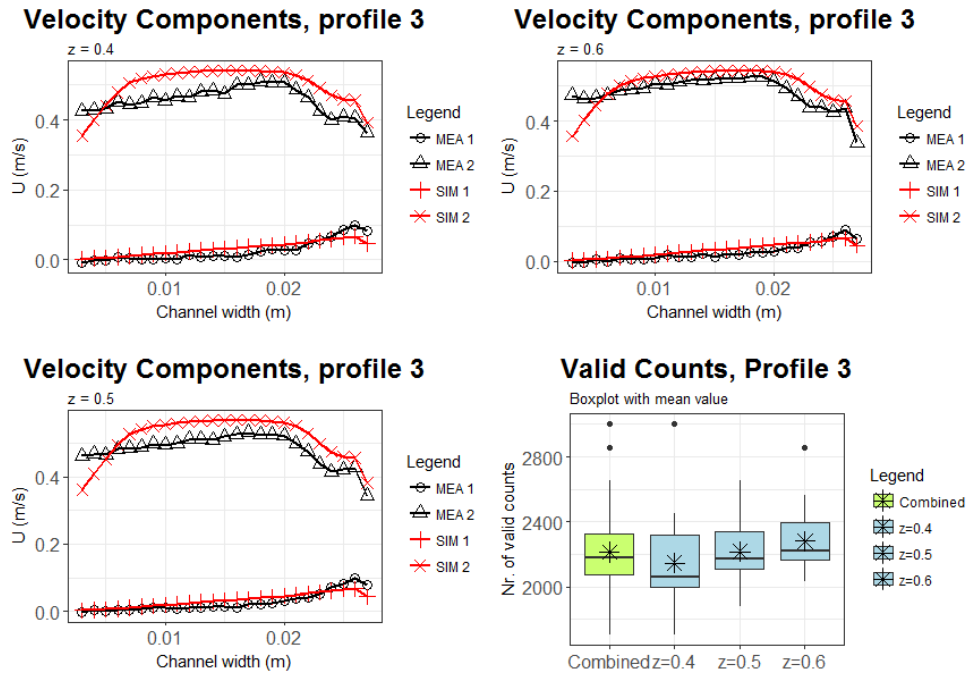


Figure 61: Adjusted coefficients velocity components comparison (Profile 3)

## Appendix H Profile 4

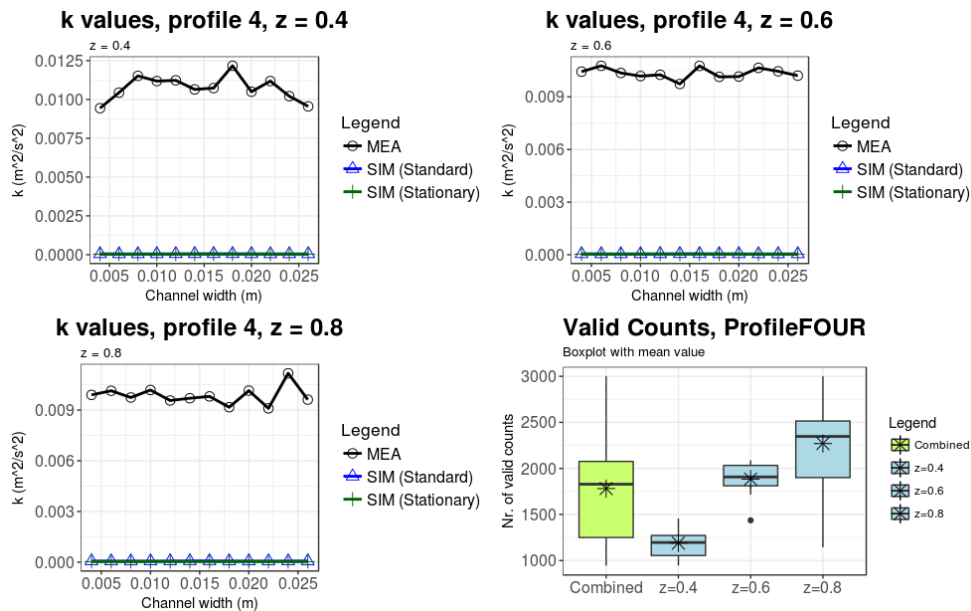


Figure 62: Turbulent kinetic energy comparison (Profile 4)

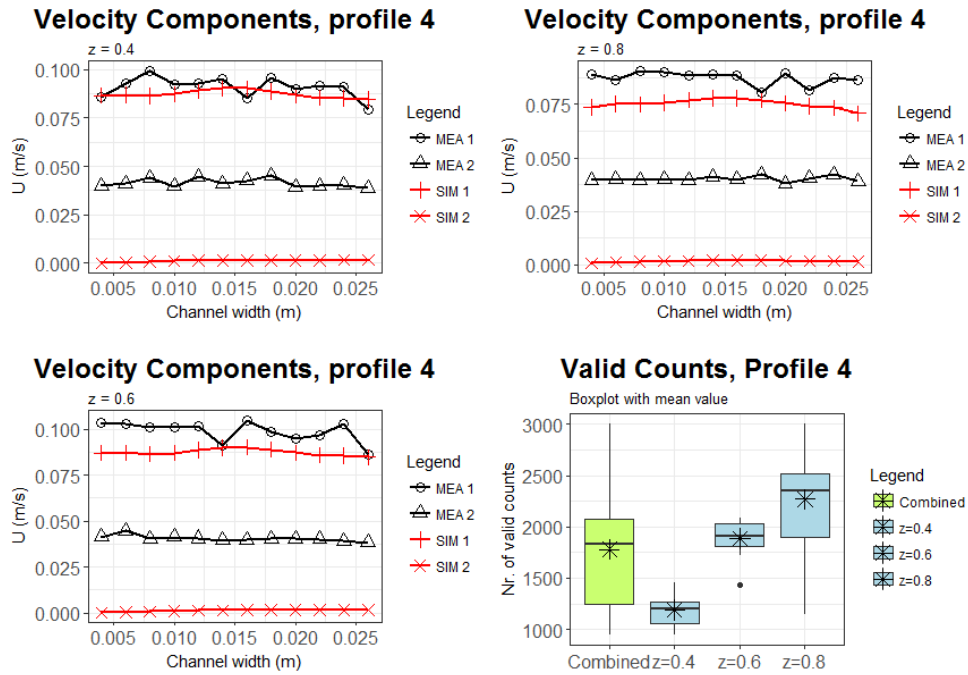


Figure 63: Standard coefficients velocity components comparison (Profile 4)

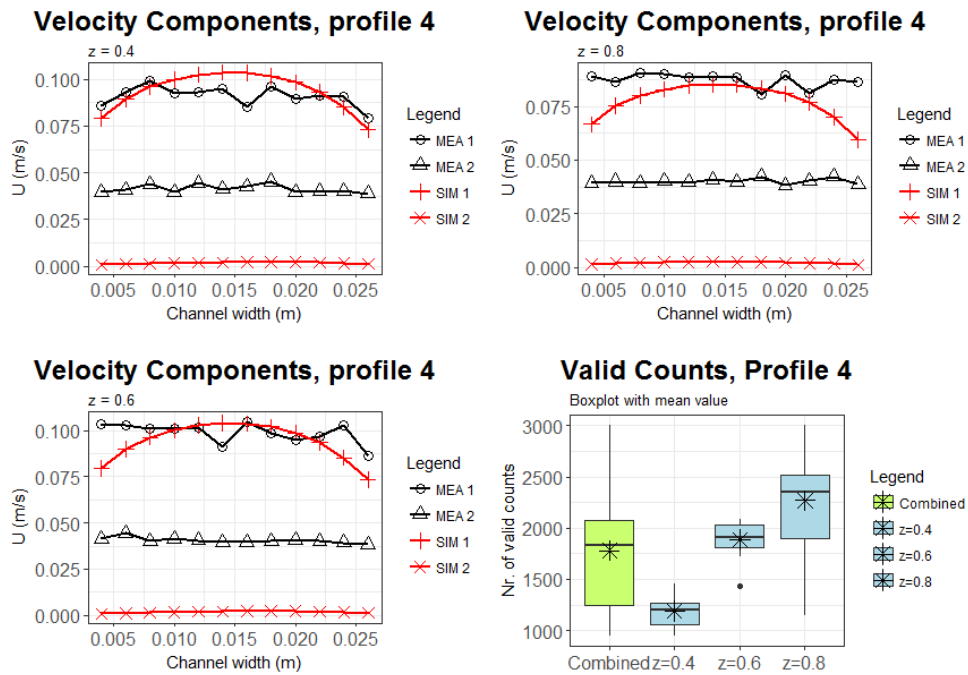


Figure 64: Adjusted coefficients velocity components comparison (Profile 4)

# Appendix I Profile 5

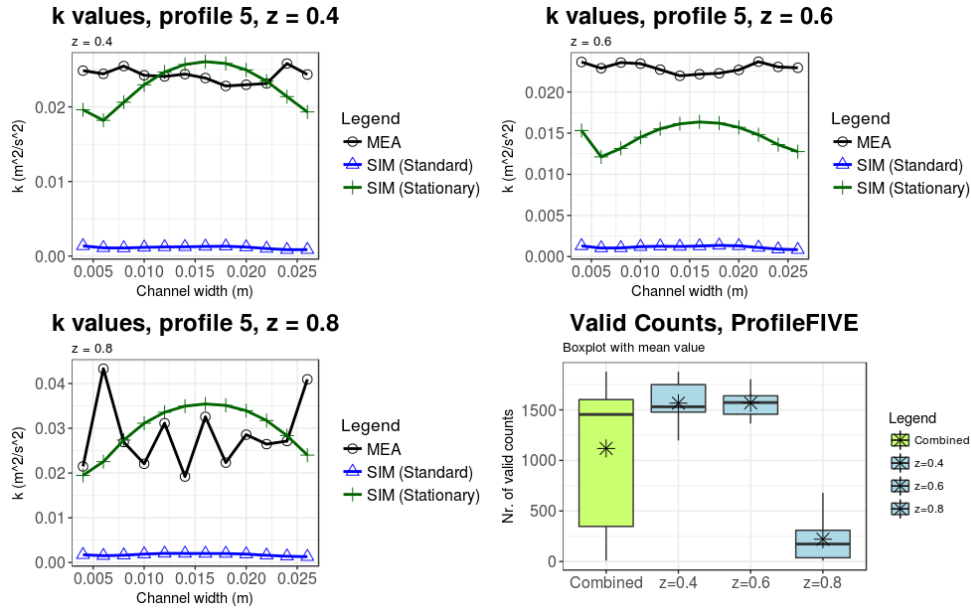


Figure 65: Turbulent kinetic energy comparison (Profile 5)

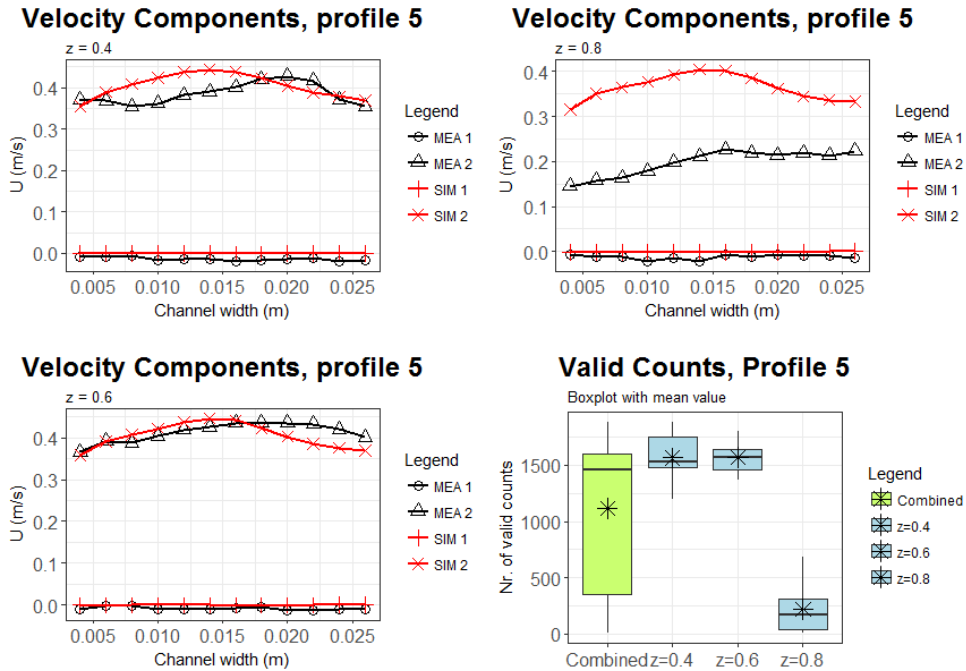


Figure 66: Standard coefficients velocity components comparison (Profile 5)

I. PROFILE 5

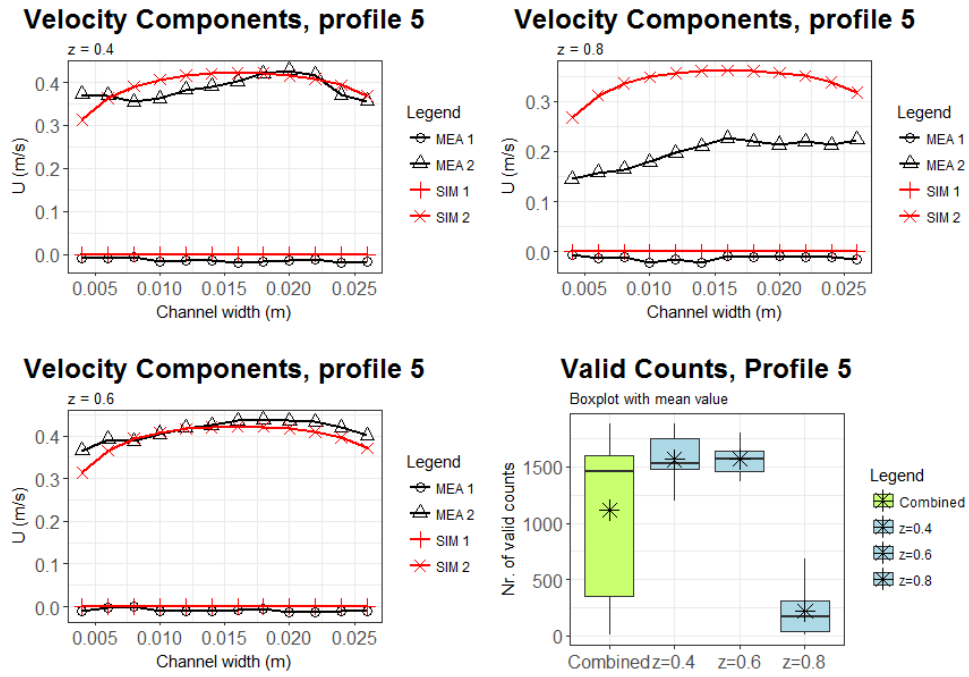


Figure 67: Adjusted coefficients velocity components comparison (Profile 5)

## References

- Abraham, J.P., E.M. Sparrow, and J.C.K. Tong (2008). “Breakdown of Laminar Pipe Flow into Transitional Intermittency and Subsequent Attainment of Fully Developed Intermittent or Turbulent Flow”. In: *Numerical Heat Transfer*. DOI: doi:10.1080/10407790802156178, .
- Abu-Ghannam, B. J. and R. Shaw (Oct. 1980). “Natural Transition of Boundary Layers—The Effects of Turbulence, Pressure Gradient, and Flow History”. In: *Journal of Mechanical Engineering Science* 22.5, pp. 213–228. ISSN: 0022-2542. DOI: 10.1243/jmes\_jour\_1980\_022\_043\_02. URL: [https://doi.org/10.1243/JMES\\_JOUR\\_1980\\_022\\_043\\_02](https://doi.org/10.1243/JMES_JOUR_1980_022_043_02).
- Beauvais, R. (1994). “Laser-Doppler Velocimetry (LDV)”. In: *Optical Measurements: Techniques and Applications*. Ed. by Mayinger, Franz. Berlin, Heidelberg: Springer Berlin Heidelberg, pp. 179–193. ISBN: 978-3-662-02967-1. DOI: 10.1007/978-3-662-02967-1\_10. URL: [https://doi.org/10.1007/978-3-662-02967-1\\_10](https://doi.org/10.1007/978-3-662-02967-1_10).
- Blumer, C. B. and E. R. VanDriest (June 1963). “Boundary layer transition- Freestream turbulence and pressure gradient effects”. In: *AIAA Journal* 1.6, pp. 1303–1306. ISSN: 0001-1452. DOI: 10.2514/3.1784. URL: <https://doi.org/10.2514/3.1784>.
- Boutier, A. and J.-M. Most (2012). *Laser Doppler Velocimetry, in Laser Velocimetry in Fluid Mechanics*. Ed. by Boutier, A. John Wiley & Sons. DOI: 10.1002/9781118569610.ch3.
- Eriksson, L. (2008). *Design of Experiments, Principles and Applications*. Ed. by Eriksson, L. Umetrics Academy. ISBN: 91-973730-4-4.
- Gondret, P., M. Lance, and L. Petit (2002). “Bouncing motion of spherical particles in fluids”. In: *Physics of Fluids* 14.2, pp. 643–652. DOI: 10.1063/1.1427920. eprint: <https://doi.org/10.1063/1.1427920>. URL: <https://doi.org/10.1063/1.1427920>.

- Groemping, Ulrike (2014). “R Package FrF2 for Creating and Analyzing Fractional Factorial 2-Level Designs”. In: *Journal of Statistical Software* 56.1, pp. 1–56. URL: <http://www.jstatsoft.org/v56/i01/>.
- Haddadi, Bahram et al. (2018). “Simultaneous Laser Doppler Velocimetry and stand-off Raman spectroscopy as a novel tool to assess flow characteristics of process streams”. In: *Chemical Engineering Journal* 334, pp. 123–133. ISSN: 1385-8947. DOI: <https://doi.org/10.1016/j.cej.2017.10.027>. URL: <http://www.sciencedirect.com/science/article/pii/S1385894717317345>.
- Hellsten, Antti (June 1998). “Some improvements in Menter’s k-omega SST turbulence model”. In: *29th AIAA, Fluid Dynamics Conference*. Fluid Dynamics and Co-located Conferences. DOI: 10.2514/6.1998-2554. URL: <https://doi.org/10.2514/6.1998-2554>.
- Langtry, Robin B. and Florian R. Menter (Dec. 2009). “Correlation-Based Transition Modeling for Unstructured Parallelized Computational Fluid Dynamics Codes”. In: *AIAA Journal* 47.12, pp. 2894–2906. ISSN: 0001-1452. DOI: 10.2514/1.42362. URL: <https://doi.org/10.2514/1.42362>.
- Langtry, Robin Blair (2006). “A correlation-based transition model using local variables for unstructured parallelized CFD codes”. PhD thesis. Universität Stuttgart. URL: <http://dx.doi.org/10.18419/opus-1705>.
- Launder, B.E. and B.I. Sharma (1974). “Application of the energy-dissipation model of turbulence to the calculation of flow near a spinning disc”. In: *Letters in Heat and Mass Transfer* 1.2, pp. 131–137. ISSN: 0094-4548. DOI: [https://doi.org/10.1016/0094-4548\(74\)90150-7](https://doi.org/10.1016/0094-4548(74)90150-7). URL: <http://www.sciencedirect.com/science/article/pii/S0094454874901507>.
- Lawson, John (2015). *Design and Analysis of Experiments with R*. Ed. by Lawson, John. CRC Press. ISBN: 9781439868133.
- (2016). *daewr: Design and Analysis of Experiments with R*. R package version 1.1-7. URL: <https://CRAN.R-project.org/package=daewr>.

- Lenth, Russell V. (2009). “Response-Surface Methods in R, Using rsm”. In: *Journal of Statistical Software* 32.7, pp. 1–17. URL: <http://www.jstatsoft.org/v32/i07/>.
- McKeon, Beverley et al. (2007). “Velocity, Vorticity, and Mach Number”. In: *Springer Handbook of Experimental Fluid Mechanics*. Ed. by Tropea, Cameron, Yarin, Alexander L., and Foss, John F. Berlin, Heidelberg: Springer Berlin Heidelberg, pp. 215–471. ISBN: 978-3-540-30299-5. DOI: 10.1007/978-3-540-30299-5\_5. URL: [https://doi.org/10.1007/978-3-540-30299-5\\_5](https://doi.org/10.1007/978-3-540-30299-5_5).
- Menter, F. R. (Aug. 1994). “Two-equation eddy-viscosity turbulence models for engineering applications”. In: *AIAA Journal* 32.8, pp. 1598–1605. ISSN: 0001-1452. DOI: 10.2514/3.12149. URL: <https://doi.org/10.2514/3.12149>.
- Menter, F. R., M. Kuntz, and R. Langtry (2003). “Ten Years of Industrial Experience with the SST Turbulence Model”. In: *Turbulence, Heat and Mass Transfer* 4, pp. 625–632.
- Menter, F. and T. Esch (2001). “Elements of industrial heat transfer predictions”. In: *16th Brazilian congress of mechanical engineering*. Vol. 20.
- Menter, F.R., T. Esch, and S. Kubacki (2002). “Transition modelling based on local variables”. In: *Engineering Turbulence Modelling and Experiments* 5, pp. 555–564. DOI: <https://doi.org/10.1016/B978-008044114-6/50053-3>.
- Nabavi, Majid and Kamran Siddiqui (2010). “A critical review on advanced velocity measurement techniques in pulsating flows”. In: *Measurement Science and Technology* 21.4, p. 042002. URL: <http://stacks.iop.org/0957-0233/21/i=4/a=042002>.
- Oertel, Herbert (2012). *Instabilitäten und turbulente Strömungen*. Ed. by Oertel jr., Herbert. Wiesbaden: Springer Fachmedien Wiesbaden, pp. 317–378. ISBN: 978-3-8348-2315-1. DOI: 10.1007/978-3-8348-2315-1\_6. URL: [https://doi.org/10.1007/978-3-8348-2315-1\\_6](https://doi.org/10.1007/978-3-8348-2315-1_6).
- Pope, S. (2000). *Turbulent Flows*. Ed. by Pope, Stephan B. Cambridge University Press. DOI: 10.1017/CB09780511840531.
- Schaefer, John et al. (Jan. 2017). “Uncertainty Quantification of Turbulence Model Closure Coefficients for Transonic Wall-Bounded Flows”. In: *AIAA Journal* 55.1, pp. 195–213.

ISSN: 0001-1452. DOI: 10.2514/1.j054902. URL: <https://doi.org/10.2514/1.J054902>.

Stephanopoulos, Kimon et al. (June 2016). “Uncertainty Quantification of Turbulence Model Coefficients in OpenFOAM and Fluent for Mildly Separated Flows”. In: *46th AIAA Fluid Dynamics Conference*. AIAA AVIATION Forum. American Institute of Aeronautics and Astronautics. DOI: 10.2514/6.2016-4401. URL: <https://doi.org/10.2514/6.2016-4401>.

Tong, Chenning and Z. Warhaft (1995). “Passive scalar dispersion and mixing in a turbulent jet”. In: *Journal of Fluid Mechanics* 292, pp. 1–38. DOI: 10.1017/S0022112095001418.

Wickham, Hadley (2009). *ggplot2: Elegant Graphics for Data Analysis*. Springer-Verlag New York. ISBN: 978-0-387-98140-6. URL: <http://ggplot2.org>.

Wilcox, David (Nov. 1988). “Reassessment of the scale-determining equation for advanced turbulence models”. In: *AIAA Journal* 26.11, pp. 1299–1310. ISSN: 0001-1452. DOI: 10.2514/3.10041. URL: <https://doi.org/10.2514/3.10041>.

Yeh, Y. and H.Z. Cummins (1964). “Localized fluid flow measurements with an He–Ne laser spectrometer”. In: *Applied Physics Letters* 4. DOI: 10.1063/1.1753925.

Zöchbauer, M., H. Smith, and T. Lauer (2015). “Advanced SCR Flow Modeling with a validated Large Eddy Simulation”. In: *SAE Technical Paper*. DOI: 10.4271/2015-01-1046..